

**Local-Field Effects and Nanostructuring  
for Controlling Optical Properties  
and Enabling Novel Optical Phenomena**

by

Ksenia Dolgaleva

Submitted in Partial Fulfillment

of the

Requirements for the Degree

Doctor of Philosophy

Supervised by

Professor Robert W. Boyd

The Institute of Optics

The College

School of Engineering and Applied Sciences

University of Rochester

Rochester, New York

2008

## Curriculum Vitae

Ksenia Dolgaleva was born in Astrakhan, Russia, on November 2, 1977. She graduated from a high school with a silver medal, and entered an undergraduate program at the Department of Physics of Moscow State University in 1994. She joined the research group of Prof. Oleg Nanii in 1998. Under supervision of Prof. Nanii, she theoretically investigated continuous-wave two-color generation in a laser with a dispersive cavity. While in Prof. Nanii's research group, Ksenia gave three presentations at two international conferences on Optics held in St. Petersburg, Russia, and wrote an article, published in *Quantum Electronics* journal. She graduated from Moscow State University with a M. S. degree in Physics in January 2000. She was awarded a prize for an outstanding Master thesis from the Russian Physical Society.

Ksenia entered the Ph. D. program at Moscow State University in April 2000. At the same time, she worked for the Optictelecom company, which was collaborating with the research group of her advisor, Prof. Nanii. Her job at Optictelecom involved preparation of scientific seminars and a lecture course, and co-authoring a manual on Fiber Optics for Optictelecom employees and undergraduate students of Moscow State University.

Ksenia moved to Rochester, NY and entered the Ph. D. program at the Institute of Optics, University of Rochester, in September 2001. She started her research under the supervision of Dr. Andrey Okishev at the Laboratory for Laser Energetics. Her first project was related to the characterization of laser performance of

a new crystal, Yb:GdCOB, a potential candidate for broadband amplifiers for the 60-beam OMEGA laser facility. After two years at the Laboratory for Laser Energetics, she joined Prof. Robert Boyd's research group in June 2003. Under supervision of Prof. Boyd, Ksenia worked on various projects, including composite laser materials, local-field-induced microscopic cascading in nonlinear optics, optical activity from artificial chiral structures, cholesteric liquid crystal lasers, and single-step phase-matched third-harmonic generation in a 1D photonic crystal. While in Prof. Boyd's group, Ksenia co-authored 11 papers, published and in preparation for publication in refereed journals, and one encyclopedia article. She gave presentations at 8 international conferences in Optics, and co-authored 4 more conference presentations given by other researchers. Ksenia was awarded a prize for outstanding student presentation at the *Frontiers in Optics* OSA Annual Meeting in Rochester in October 2008.

## Acknowledgements

I am endlessly grateful to my advisor, Prof. Robert Boyd, for his great help, guidance, and wise supervision. He contributed a lot towards my growth as a young scientist, and I cannot think of a better experience than that I gained being a part of his research group.

I would like to acknowledge Prof. Peter Milonni for his mentoring, support, and belief in success of some of my projects that I had been struggling through and that eventually worked.

I am also thankful to Prof. John Sipe for his mentoring, valuable discussions, and healthy criticism that ensured success and clarity of some crucial parts of my work.

I am grateful to Dr. Svetlana Lukishova for her support, help and encouragement of my efforts and struggling. Her good advice helped me to make some crucial decisions that cardinally changed my future towards the best.

I would like to thank Prof. Shaw Horng Chen and his student Ku-Hsien (Simon) Wei for a great opportunity to collaborate with them on a wonderful project, and to realize how useful my skills and knowledge could be for someone working in a different field.

I am also grateful to Dr. Sergei Volkov, Prof. Martti Kauranen and Prof. Yuri Svirko for a great collaboration and valuable discussions in the process of which I have learned a lot about a field that is new to me.

I would like to acknowledge Prof. Paras Prasad, Prof. Ion Tiginyanu, Dr. Paul

Markowicz, and Dr. Lilian Syrbu for fruitful collaborations.

I would like to thank Prof. Carlos Stroud, Prof. Mikhail Noginov, Prof. John Dowling, Prof. Lukas Novotny, Prof. Nick Lepeshkin, Prof. Stephen Rand, and Prof. Anthony Siegman for valuable discussions.

I am thankful to Prof. Lewis Rothberg and Prof. Miguel Alonso for agreeing to serve on my Ph. D. committee and for their advice on how to improve my Ph. D. thesis.

Many thanks to Dr. Andrey Okishev and Dr. John Zuegel for valuable laboratory skills that I have gained while working with them.

I am grateful to Dr. Frank Duarte, Dr. Robert James, and Prof. Steve Jacobs for assisting in my attempt to prepare a new optical material that is interesting to investigate from the perspective of my research.

I would like to thank fellow graduate students and postdocs from Prof. Boyd's research group. I am especially grateful to Heedeuk Shin and Andreas Liapis who collaborated with me directly. Many thanks to Giovanni Piredda, Aaron Schweinsberg, Colin O'Sullivan-Hale, Petros Zerom, George Gehring, Anand Jha, Zhimin Shi, Joseph Wornehm, Mehul Malik, Cliff Chen, Hye Jeong Chang, and Sandrine Hocde.

I am grateful to Per Adamson and Brian McIntyre for their technical assistance and help with equipment. I am thankful to the Institute of Optics administrative assistants: Maria Schnitzler, Joan Christian, Lissa Cotter, Gina Kern, Noelene Votens, Betsy Benedict, and Maria Banach. Without their help I would not succeed to com-

plete my program.

I would especially like to acknowledge the Director of the Institute of Optics, Prof. Wayne Knox, for his support during my first years at the Institute and for being such a dedicated Director whose contribution towards the development of the Institute is hard to overestimate.

I am endlessly grateful to my supportive family: my husband Sergei, my mother Natalia Feketa, my daughter Natalia, my step-father Iosif Feketa, my father Pavel Dolgalev, my sister Anna Feketa, my aunts Irina Dolgaleva, Valentina Fomina, and Lubov Anpilova, my cousins and my grandmother Ekaterina Sorokina. I would like to devote this thesis to them all, as without their support I would not be able to get through this challenge.

Many thanks to my supportive friends.

## Publications

1. K. Dolgaleva, H. Shin, R. W. Boyd, and J. E. Sipe, "Observation of microscopic cascaded contribution to the fifth-order nonlinear susceptibility," to be submitted to *Phys. Rev. Lett.*
2. K. Dolgaleva, R. W. Boyd, and P. W. Milonni, "Effects of Local Fields on Laser Gain for Layered and Maxwell Garnett Composite Materials," accepted for publication in *J. Phys. A*.
3. S. N. Volkov, K. Dolgaleva, R. W. Boyd, K. Jefimovs, J. Turunen, Y. Svirko, B. K. Canfield, and M. Kauranen, "Optical activity in diffraction from a planar array of achiral nanoparticles," submitted to *Phys. Rev. Lett.*
4. S. K. H. Wei, S. H. Chen, K. Dolgaleva, S. G. Lukishova, and R. W. Boyd, "Robust organic lasers comprising glassy-cholesteric pentafluorene doped with a red-emitting oligofluorene," submitted to *Appl. Phys. Lett.*
5. K. Dolgaleva, S. K. H. Wei, S. G. Lukishova, S. H. Chen, K. Schwertz, and R. W. Boyd, "Enhanced laser performance of cholesteric liquid crystals doped with oligofluorene dye," *J. Opt. Soc. Am. B* **25**, 1496–1504 (2008).
6. K. Dolgaleva, R. W. Boyd, and J. E. Sipe, "Cascaded nonlinearity caused by local-field effects in the two-level atom," *Phys. Rev. A* **76**, 063806 (2007).
7. K. Dolgaleva and R. W. Boyd, "Laser gain media based on nanocomposite materials," *J. Opt. Soc. Am. B* **24**, A19–A25 (2007).
8. K. Dolgaleva, R. W. Boyd, and P. W. Milonni, "Influence of local-field effects on the radiative lifetime of liquid suspensions of Nd:YAG nanoparticles," *J. Opt. Soc. Am. B* **24**, 516–521 (2007).
9. L. Syrbu, V. V. Ursaki, I. M. Tiginyanu, K. Dolgaleva, and R. W. Boyd, "Red and green nanocomposite phosphors prepared from porous GaAs templates," *J. Opt. A: Pure Appl. Opt.* **9**, 401–404 (2007).
10. L. Syrbu, V. V. Ursaki, I. M. Tiginyanu, K. Dolgaleva, and R. W. Boyd, "Er- and Eu-doped CaP-oxide porous composites for optoelectronic applications," *Phys. Stat. Sol. (RRL)* **1**, R13–R15 (2007).
11. P. P. Markowicz, V. K. S. Hsiao, H. Tiryaki, A. N. Cartwright, P. N. Prasad, K. Dolgaleva, N. N. Lepeshkin, and R. W. Boyd, "Enhancement of third-harmonic generation in a polymer-dispersed liquid-crystal grating," *Appl. Phys. Lett.* **87**, 051102 (2005).
12. V. G. Voronin, K. P. Dolgaleva, and O. E. Nanii, "Two-color generation in a solid-state laser with a dispersive cavity," *Quantum Electron.* **30**, 778–782 (2000).

## Other Publications

1. A. V. Okishev, K. P. Dolgaleva, and J. D. Zuegel, “Experimental optimization of diode-pumped Yb:GdCOB laser performance for broadband amplification at 1053 nm,” ICONO/LAT conference proceedings (St.-Petersburg, Russia, 2005).
2. K. Dolgaleva, N. Lepeshkin, and R. W. Boyd, “Frequency doubling,” *Encyclopedia of Nonlinear Science*, (London, Routledge, 2004).
3. S. K. Isaev, V. G. Voronin, O. E. Nanii, A. N. Turkin, K. P. Dolgaleva, D. D. Scherbatkin, “Fundamentals of Fiber Optics and Integral Optics” (an undergraduate-level manual, in Russian) Moscow State University, 2002.

## Conference Papers

1. K. Dolgaleva, H. Shin, R. W. Boyd, and J. E. Sipe, “Experimental separation of microscopic cascading induced by local-field effects,” *Frontiers in Optics and Laser Science (FiO/LS) 2008*, Rochester, NY (USA).
2. R. W. Boyd, K. Dolgaleva, G. Piredda, and A. Schweinsberg, “Nonlinear optics of structured photonic materials,” *Frontiers in Optics and Laser Science (FiO/LS) 2008*, Rochester, NY (USA).
3. K. Dolgaleva, R. W. Boyd, S. N. Volkov, K. Jefimovs, J. Turunen, Y. Svirko, B. K. Canfield, and M. Kauranen, “Polarization changes in diffraction from planar periodic patterns with pure structural and molecular chirality,” *Quantum Electronics and Laser Science (QELS) 2008*, San Jose, CA (USA).
4. K. Dolgaleva, R. W. Boyd, and J. E. Sipe, “Microscopic cascading in fifth-order nonlinearity induced by local-field effects,” *Nonlinear Photonics 2007*, Quebec, QC (Canada).
5. K. Dolgaleva, R. W. Boyd, and J. E. Sipe, “Cascade-like nonlinearity caused by local-field effects: Extending Bloembergen’s result,” *Quantum Electronics and Laser Science (QELS) 2007*, Baltimore, MD (USA).
6. K. Dolgaleva, K. H. S. Wei, A. Trajkovska, S. Lukishova, R. W. Boyd, and S. H. Chen, “Oligofluorene as a new high-performance dye for cholesteric liquid crystal lasers,” *Frontiers in Optics and Laser Science (FiO/LS) 2006*, Rochester, NY (USA).
7. S. K. H. Wei, K. Dolgaleva, A. Trajkovska, S. Lukishova, R. W. Boyd, and S. H. Chen, “High performance and color purity in oligofluorene-doped cholesteric liquid crystal laser,” *Frontiers in Optics and Laser Science (FiO/LS) 2006*, Rochester, NY (USA).



8. K. Dolgaleva and R. W. Boyd, "A bi-exponential fluorescence decay in composite materials based on Nd:YAG nanoparticles," Conference on Lasers and Electro-Optics (CLEO) 2006, Long Beach, CA (USA).
9. K. Dolgaleva and R. W. Boyd, "Influence of local-field effects on the radiative properties of Nd:YAG nanoparticles in a liquid suspension," American Physical Society (APS) March Meeting 2006, Baltimore, MD (USA).
10. A. V. Okishev, K. P. Dolgaleva, and J. D. Zuegel, "Experimental optimization of diode-pumped Yb:GdCOB laser performance for broadband amplification at 1053 nm," International Conference on Coherent and Nonlinear Optics collocated with International Conference on Lasers, Applications, and Technologies (ICONO/LAT), St.-Petersburg, Russia, 2005.
11. P. P. Markowicz, V. Hsiao, H. Tiryaki, P. N. Prasad, N. N. Lepeshkin, K. Dolgaleva, and R. W. Boyd, "Enhancement of third-harmonic generation in Photonics crystals," Conference on Lasers and Electro-Optics (CLEO) 2005, Baltimore, MD (USA).
12. K. Dolgaleva, N. Lepeshkin, R. W. Boyd, P. P. Markowicz, V. K. S. Hsiao, H. Tiryaki, A. N. Cartwright, and P. N. Prasad, "Phase-matched third-harmonic generation in a 1-D Photonics crystal," Frontiers in Optics and Laser Science (FiO/LS) 2004, Rochester, NY (USA).
13. O. E. Nanii, K. P. Dolgaleva, "A novel construction of a two-color laser with a dispersive cavity using two pump sources," International Optical Congress "Optics-XXI century," St.-Petersburg, Russia, 2000.
14. K. P. Dolgaleva, K. N. Belov, O. E. Nanii, "Two-color generation in a laser with a dispersive cavity and two pump sources," International Conference of Young Scientists and Specialists "Optics-2000," St.-Petersburg, Russia.
15. K. P. Dolgaleva, "Wavelength competition in a two-color laser with a dispersive cavity," International Conference of Young Scientists and Specialists "Optics-99," St.-Petersburg, Russia, 1999.

## Abstract

My Ph. D. thesis is devoted to the investigation of the methods for controlling and improving the linear and nonlinear optical properties of materials. Within my studies, two approaches are considered: nanostructuring and invoking local-field effects. These broad topics involve various projects that I have undertaken during my Ph. D. research.

The first project is on composite laser gain media. It involves both nanostructuring and using local-field effects to control the basic laser parameters, such as the radiative lifetime, small-signal gain and absorption, and the saturation intensity. While being involved in this project, I have performed both theoretical and experimental studies of laser characteristics of composite materials. In particular, I have developed simple theoretical models for calculating the effective linear susceptibilities of layered and Maxwell Garnett composite materials with a gain resonance in one of their components. The analysis of the results given by the models suggests that local-field effects provide considerable freedom in controlling the optical properties of composite laser gain media. I have also experimentally measured the radiative lifetime of Nd:YAG nanopowder suspended in different liquids to extract information regarding local-field effects.

The second project is devoted to the investigation of a not-well-known phenomenon that local-field effects can induce, which is microscopic cascading in nonlinear optics. This project involves the theoretical prediction of local-field-induced microscopic cas-

cading effect in the fifth-order nonlinear response and its first experimental observation. This effect has been mostly overlooked or underestimated, but could prove useful in quantum optics. I have shown that, under certain conditions, the microscopic cascaded contribution can be a dominant effect in high-order nonlinearities.

The third project is about characterization of laser performance of a new dye, oligofluorene, embedded into cholesteric liquid crystal (CLC) structures. These structures constitute self-assembling mirrorless distributed-feedback low-threshold laser systems. I have performed a detailed comparative experimental study of the laser characteristics of cholesteric liquid crystals doped with oligofluorene and a well studied dye, DCM, commonly used for lasing in CLCs. I have experimentally demonstrated that oligofluorene-doped CLCs yield a total output energy in the transverse single-mode regime five times that of DCM-doped CLCs with superior temporal and spatial stability.

In the fourth project I investigated the polarization changes of light diffracted from artificial planar chiral structures. I have performed the measurements of the polarization state of light diffracted from planar arrays of nanoparticles with molecular and pure structural chirality. Both sorts of samples are shown to lead to comparable polarization changes in the diffracted light. The results can be explained by a simple model in which the polarization effects resulted from an independent scattering by individual particles, with no interparticle coupling, where the array structure simply determines the direction of the diffraction maximum. It invites a conclusion that

structural and molecular chirality are indistinguishable in diffraction experiments, in contrast to some earlier published statements.

# Contents

<b>1</b>	<b>Background</b>	<b>1</b>
1.1	Introduction . . . . .	1
1.2	Composite Optical Materials . . . . .	3
1.2.1	Composite Geometries . . . . .	5
1.3	Local Field . . . . .	7
1.3.1	Local-Field Models for Homogeneous Media . . . . .	8
1.3.2	Local Field and Cascading in Nonlinear Optics . . . . .	14
1.4	Lorentz–Maxwell–Bloch Equations . . . . .	17
1.5	Dye-Doped Cholesteric Liquid Crystal Lasers . . . . .	20
1.6	Planar Chiral Structures . . . . .	24
<b>2</b>	<b>Composite Laser Materials</b>	<b>27</b>
2.1	Introduction . . . . .	27
2.2	The Idea of Composite Lasers . . . . .	28

2.2.1	Influence of Local-Field Effects on Laser Properties of Dielectric Materials . . . . .	29
2.2.2	Analysis . . . . .	37
2.3	Influence of Local-Field Effects on the Radiative Lifetime of Liquid Suspensions of Nd:YAG Nanoparticles . . . . .	40
2.3.1	Sample Preparation and Experiment . . . . .	44
2.3.2	Data Analysis . . . . .	49
2.4	Optimization of Laser Gain Properties for Layered and Maxwell Garnett Composite Geometries . . . . .	54
2.4.1	Lorentz local field in a resonant medium . . . . .	55
2.4.2	Linear Susceptibility of Layered Composite Materials . . . . .	60
2.4.3	Linear Susceptibility of Maxwell Garnett Composite Materials . . . . .	65
2.4.4	Analysis . . . . .	70
2.5	Conclusions . . . . .	80
<b>3</b>	<b>Microscopic Cascading</b>	<b>84</b>
3.1	Introduction . . . . .	84
3.2	Theoretical Prediction of Microscopic Cascading . . . . .	87
3.2.1	Maxwell–Bloch equations approach . . . . .	87
3.2.2	The Naïve Local-Field Correction . . . . .	90
3.2.3	Bloembergen’s approach . . . . .	93
3.3	Numerical Analysis . . . . .	98

3.4	Experimental Observation of Microscopic Cascading . . . . .	106
3.5	Conclusions . . . . .	120
<b>4</b>	<b>Dye-Doped CLC Lasers</b>	<b>122</b>
4.1	Introduction . . . . .	122
4.2	Sample Preparation . . . . .	126
4.3	Experimental Setup . . . . .	129
4.4	Stability and Frequency Mode Competition . . . . .	131
4.5	Lasing Output . . . . .	133
4.5.1	Transverse single-mode regime . . . . .	134
4.5.2	Transverse multi-mode regime . . . . .	137
4.5.3	Laser Output Degradation Issues in CLCs . . . . .	140
4.6	Conclusions . . . . .	141
<b>5</b>	<b>Artificial Chiral Structures</b>	<b>144</b>
5.1	Introduction . . . . .	144
5.2	Experiment . . . . .	148
5.3	Experimental Data . . . . .	150
5.4	Wire Model . . . . .	151
5.5	Conclusions . . . . .	156
<b>6</b>	<b>Summary</b>	<b>158</b>
	<b>Bibliography</b>	<b>163</b>

<i>CONTENTS</i>	xvi
<b>A Maxwell Garnett Mesoscopic Electric Field</b>	<b>178</b>
<b>B Optical Bistability</b>	<b>181</b>



# List of Figures

1.1	Composite material geometries . . . . .	5
2.1	Basic laser parameters . . . . .	39
2.2	SEM picture of Nd:YAG nanopowder . . . . .	44
2.3	Liquids used for suspending Nd:YAG nanopowder . . . . .	45
2.4	Experimental setup for measuring the radiative lifetime of Nd:YAG nanopowder . . . . .	46
2.5	Typical fluorescence decay in the Nd:YAG nanopowder . . . . .	47
2.6	Experimentally measured radiative lifetimes of the Nd:YAG-nanopowder suspensions . . . . .	53
2.7	Small-signal gain of a layered composite material as a function of the refractive index . . . . .	73
2.8	Small-signal gain of a layered composite material as a function of the volume fraction of the resonant component . . . . .	74

2.9	Small-signal gain of a layered composite material as a function of the detuning of the optical field . . . . .	76
2.10	Small-signal gain of a Maxwell Garnett composite material as a function of the refractive index of the non-resonant host . . . . .	78
2.11	Small-signal gain of a Maxwell Garnett composite material as a function of the inclusion volume fraction . . . . .	79
2.12	Small-signal gain of a Maxwell Garnett composite material as a function of the detuning of the optical field . . . . .	80
3.1	The ranges of validity of various susceptibility models . . . . .	101
3.2	Real and imaginary parts of the total susceptibility . . . . .	103
3.3	The ratio of the absolute values of cascaded and direct contributions to $\chi^{(5)}$ . . . . .	103
3.4	Real and imaginary parts of the direct and cascaded contributions to $\chi^{(5)}$ . . . . .	105
3.5	Experimental setup for degenerate four-wave mixing . . . . .	108
3.6	Intensities of first and second diffracted orders on the logarithmic scale	110
3.7	Typical experimental data for $\chi^{(3)}$ and $\chi^{(5)}$ . . . . .	111
3.8	Phase matching diagram . . . . .	113
3.9	Normalized efficiencies of contributions to $\chi^{(5)}$ . . . . .	116
3.10	Measured fifth-order nonlinear susceptibility and its macroscopic cascaded contribution . . . . .	118

4.1	Reflectance and lasing spectra of dye-doped CLC structures . . . . .	128
4.2	Experimental setup for lasing in CLC . . . . .	129
4.3	Intensity distribution of the laser output of dye-doped CLC lasers . . .	131
4.4	A photograph of the lasing output of dye-doped CLC structures . . .	134
4.5	Laser output from dye-doped CLC structures in single-mode regime . .	135
4.6	Slope efficiency of dye-doped CLC lasers in single-mode regime . . . .	136
4.7	Laser output from dye-doped CLC structures in multi-mode regime . .	137
4.8	Slope efficiency of dye-doped CLC lasers in multi-mode regime . . . .	138
5.1	Experimental setup and sample layout . . . . .	148
5.2	Polarization azimuth rotation and ellipticity of light in diffraction from planar structures . . . . .	150
5.3	Scattering from a tilted cross . . . . .	153
5.4	Polarization azimuth rotation predicted by wire model . . . . .	154
B.1	Parameter space for bistability in population inversion . . . . .	184

# Chapter 1

## Background

### 1.1 Introduction

Optical materials have a broad range of applications in a variety of aspects of human life. Among those are medicine, military, communications, computing, manufacturing, and various industrial applications. Rapid progress of nanotechnology opens new opportunities in designing optical materials with improved optical properties.

The primary goal of my Ph.D. dissertation is to investigate novel methods of controlling linear and nonlinear optical properties of materials, and to come up with new efficient solutions of how one can achieve the desired control. There are many approaches one can use to significantly modify the optical properties of materials. Among the methods I have been studying are nanostructuring and exploiting local-field effects. The former method is a popular way to approach the problem of control-

ling the optical properties of materials. With rapid development of nanotechnology, this method becomes more and more important and accessible. The latter method, relying on local-field effects, requires a deep understanding of fundamental nature of the local-field phenomenon in both linear and nonlinear optics. If one gains the necessary understanding, local-field effects will open many unknown opportunities and serve as a source for novel unusual effects.

The two approaches to controlling the optical properties of nonlinear and laser materials led to several projects which I have undertaken as a part of my Ph. D. research. Among these projects are

- Optimization of laser properties of composite laser gain media through use of local-field effects;
- Microscopic cascaded phenomena in nonlinear optics induced by local-field effects;
- Characterization and optimization of laser performance of dye-doped cholesteric liquid crystal lasers;
- Polarization changes in diffraction off artificial planar chiral structures.

In the current chapter, I give an overview of various concepts that form the basis of my research. I describe the individual research projects in the latter chapters of my dissertation. In Chapter 2, I present my theoretical and experimental work on controlling the basic laser parameters of nanocomposite optical materials. This

study involves local-field effects in combination with nanostructuring. Chapter 3 is devoted to a microscopic cascading phenomenon in nonlinear optics that I accidentally uncovered theoretically, and later observed experimentally. This phenomenon is a consequence of local-field effects. It has potential in applications for quantum and conventional lithography. I present my work on characterization and optimization of laser performance of dye-doped cholesteric liquid crystal lasers in Chapter 4. Chapter 5 describes my experiment on polarization control of light diffracted from artificial planar chiral structures. Finally, I summarize my Ph.D. research in Chapter 6

## 1.2 Composite Optical Materials

Nanocomposite optical materials are nanoscale mixtures of two or more homogeneous constituents in which the individual particles are much smaller than the optical wavelength, but still large enough to have their own dielectric identities. The optical properties of composite materials can be adjusted by controlling the constituents and morphology of the composite structure. Properly tailored composites can display the best qualities of each of their constituents, or, in certain cases, can display properties that even exceed those of their constituents. These features render composite materials valuable for applications in photonics and laser engineering.

Nanocomposite optical materials are becoming more and more important in laser applications as nanofabrication technology has been rapidly developing. In particular, nanoscale ceramic composite laser gain media with improved optical properties have

been reported [1, 2]. It has also been shown that one can improve the performance of a laser material by mixing it with some other material on a nanoscale in such a way that the thermal refractive index changes of the resulting composite material are smaller than those of either of the constituents [3, 4]. In the current work we are concerned with a somewhat different approach to controlling the laser properties of nanocomposite materials: by implementing local-field effects [5, 6].

The optical properties of composite materials have been the subject of many studies (see, for example, [7–10]). In particular, the modification of the radiative lifetime of composite materials caused by local-field effects was addressed in many publications both theoretically [11–15] and experimentally [16–24]. The influence of the local-field effects on the nonlinear optical properties of composite materials is even more significant, as the material response scales as several powers of the local-field correction factor (*i. e.*, the quantity equal to the ratio of the local field acting on a typical emitter to the average field in the medium). Theoretical modeling of the nonlinear optical response has been reported for many different geometries of composite materials [25–28]. In particular, rigorous theories for Maxwell Garnett-type composite materials [25] and layered composite materials [27] have been developed. It was shown that a significant enhancement of the nonlinear optical response is possible under certain conditions. A number of experiments in the field yielded promising results [29–32]. Thus, a composite-material approach has proven to be a valuable tool in designing optical materials with enhanced nonlinear response.

While there have been numerous studies of the nonlinear optical properties of composite materials, there has not been a systematic study yet of their laser properties. In Chapter 2 we present a study of the influence of the local-field effects on the laser properties of composite materials. We believe that the analysis done in this work will help in further development of new materials for laser applications.

### 1.2.1 Composite Geometries

There are three types of composite geometries mainly discussed in the literature: Maxwell Garnett composites [7, 8, 28], Bruggeman composites [32–34], and layered composites [27, 28, 31] (see Fig. 1.1).

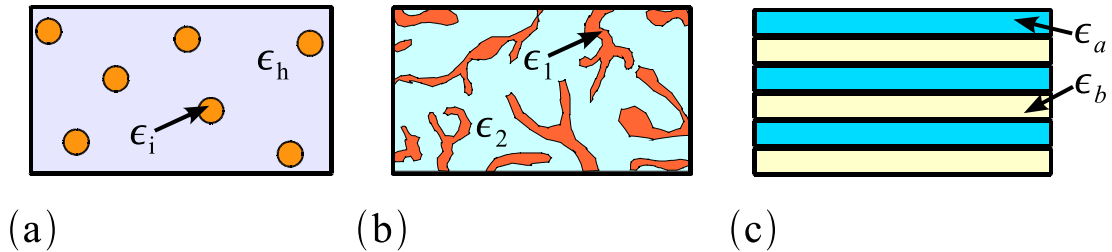


Figure 1.1: Composite material structures: (a) Maxwell Garnett geometry; (b) Bruggeman geometry; (c) layered geometry.

The Maxwell Garnett type of composite geometry is a collection of small particles (the inclusions) distributed in a host medium. The inclusions are assumed to be spheres or ellipsoids of a size much smaller than the optical wavelength; the distance between them must be much larger than their characteristic size and much smaller than the optical wavelength. Under these conditions, one can treat the composite



material as an effective medium, characterized by an effective (average) dielectric constant,  $\epsilon_{\text{eff}}$ , which satisfies the relation [7, 8]

$$\frac{\epsilon_{\text{eff}} - \epsilon_{\text{h}}}{\epsilon_{\text{eff}} + 2\epsilon_{\text{h}}} = f_{\text{i}} \frac{\epsilon_{\text{i}} - \epsilon_{\text{h}}}{\epsilon_{\text{i}} + 2\epsilon_{\text{h}}}. \quad (1.1)$$

Here  $\epsilon_{\text{h}}$  and  $\epsilon_{\text{i}}$  are the dielectric constants of the host and inclusion materials, respectively, and  $f_{\text{i}}$  is the volume fraction of the inclusion material in the composite.

In the Maxwell Garnett model the composite medium is treated asymmetrically. It is assumed that the host material completely surrounds the inclusion particles, and the result for the effective dielectric constant of the composite will be different if we interchange the host and inclusion dielectric constants in the expression (1.1). This problem is eliminated in the Bruggeman composite model [35], in which each particle of each constituent component is considered to be embedded in an effective medium characterized by  $\epsilon_{\text{eff}}$ . The corresponding equation defining the effective dielectric constant thus has the form [32]

$$0 = f_a \frac{\epsilon_a - \epsilon_{\text{eff}}}{\epsilon_a + 2\epsilon_{\text{eff}}} + f_b \frac{\epsilon_b - \epsilon_{\text{eff}}}{\epsilon_b + 2\epsilon_{\text{eff}}}. \quad (1.2)$$

Here  $\epsilon_a$  and  $\epsilon_b$  are the dielectric constants of the constituent components  $a$  and  $b$  and  $f_a$  and  $f_b$  are the volume fractions of the components.

The third composite model shown in Fig. 1.1 is a layered structure consisting of alternating layers of two materials ( $a$  and  $b$ ) with different optical properties.

The thicknesses of the layers should be much smaller than the optical wavelength. Materials of this sort are anisotropic. For light polarized parallel to the layers of such a composite material the effective dielectric constant is given by a simple volume average of the dielectric constants of the constituents:

$$\epsilon_{\text{eff}} = f_a \epsilon_a + f_b \epsilon_b. \quad (1.3)$$

The electric field in this case is spatially uniform, as the boundary conditions require continuity of its tangential part on the border between two constituents. However, for the light polarized perpendicular to the layers, the effective dielectric constant is given by

$$\frac{1}{\epsilon_{\text{eff}}} = \frac{f_a}{\epsilon_a} + \frac{f_b}{\epsilon_b}. \quad (1.4)$$

In the latter case the electric field is non-uniformly distributed between the two constituents in the composite, and local-field effects are of particular interest.

The composite geometries that we described above are those used most often in the design of composite optical materials.

### 1.3 Local Field

It is well-known that the field driving an atomic transition in a material medium, the local field, is different in general from both the external field and the average field inside the medium. The difference from the average field does not play a significant

role when one considers a low-density medium. To describe the optical properties of such a system, one can use the macroscopic (ensemble average) field. However, if the atomic density of a system exceeds  $\approx 10^{15} \text{ cm}^{-3}$  [36], the influence of local-field effects becomes significant and cannot be neglected.

In order to account for local-field effects on the optical properties of a material, one needs to apply a proper model relating the local field to its macroscopic counterparts, namely the average field and polarization. The choice of the model strongly depends on the medium of interest. For example, local field in a homogeneous medium can be related to the macroscopic average field according to

$$\tilde{\mathbf{E}}_{\text{loc}} = L\tilde{\mathbf{E}}, \quad (1.5)$$

where  $L$  is the local-field correction factor. The tilde denotes quantities oscillating at an optical frequency. The relationship between the local and average fields can be rather complicated in composite materials. In this Section we describe several models of local field for homogeneous materials. Local field of composite geometries is a more specific subject, and we cover it in Chapter 2.

### 1.3.1 Local-Field Models for Homogeneous Media

Existing theoretical models predict different expressions for the local-field correction factor  $L$ , relating the local field to the average field in the medium (see Eq. (1.5)).

Two models, most commonly used to describe the experimental outcomes, are the

virtual-cavity model, or Lorentz model [37], and the real-cavity model [11]. A more precise version of the real-cavity model is the Onsager model of local field [38]. Below we give a brief description to these models of local field, and mention some other, more sophisticated models for homogeneous media, which reconcile the simpler models.

### Lorentz Local Field

It is conventional to describe local-field effects in a homogeneous material medium using the well-known Lorentz model. In the simplest version of this model, one treats the medium as a cubic lattice of point dipoles of the same sort. In order to find the local field acting on a typical dipole of the medium, one surrounds the dipole of interest with an imaginary spherical cavity of radius much larger than the distance between the dipoles, and much smaller than the optical wavelength. The contributions to the local field from the dipoles situated within the spherical cavity are accounted for exactly, while the dipoles outside the cavity are treated as uniformly distributed, characterized by some average macroscopic polarization. This approach yields the well-known expression

$$\tilde{\mathbf{E}}_{\text{loc}} = \tilde{\mathbf{E}} + \frac{4\pi}{3}\tilde{\mathbf{P}} \quad (1.6)$$

for the local field  $\tilde{\mathbf{E}}_{\text{loc}}$  in terms of the average macroscopic field  $\tilde{\mathbf{E}}$  and the macroscopic polarization  $\tilde{\mathbf{P}}$ . Local field given by Eq. (1.6) is called “Lorentz local field.” It is derived in many textbooks (see, for example, [5, 6]). The textbook model used for deriving Eq. (1.6) is known as virtual-cavity model, because a fictitious sphere is

introduced as a trick for calculating the local field acting on a typical dipole in the medium. An alternative, more elegant, derivation of the relationship (1.6) which does not require introducing an imaginary sphere was described by Aspnes [37].

We further derive the Lorentz–Lorenz (or Clausius–Mossotti) relation for the dielectric permittivity  $\epsilon^{(1)}$  and microscopic polarizability  $\alpha$ . Let us assume for now that the medium is lossless and dispersionless. We represent the dipole moment induced in a typical molecule (or atom) of the medium as

$$\tilde{\mathbf{p}} = \alpha \tilde{\mathbf{E}}_{\text{loc}}. \quad (1.7)$$

The macroscopic polarization of the material is given by the equation

$$\tilde{\mathbf{P}} = N \tilde{\mathbf{p}}, \quad (1.8)$$

where  $N$  denotes molecular (or atomic) number density. Using Eqs. (1.6) through (1.8), we find that the polarization and macroscopic field are related by

$$\tilde{\mathbf{P}} = N\alpha \left( \tilde{\mathbf{E}} + \frac{4\pi}{3} \tilde{\mathbf{P}} \right). \quad (1.9)$$

We assume the polarization  $\tilde{\mathbf{P}}$  to be linear in the average field:

$$\tilde{\mathbf{P}} = \chi^{(1)} \tilde{\mathbf{E}}, \quad (1.10)$$

where  $\chi^{(1)}$  is the linear optical susceptibility of the medium. Substituting the expression (1.9) into (1.10), solving for  $\chi^{(1)}$ , and eliminating the field  $\tilde{\mathbf{E}}$ , we find that

$$\chi^{(1)} = \frac{N\alpha}{1 - \frac{4\pi}{3}N\alpha}. \quad (1.11)$$

Expressing the left-hand side of (1.11) as  $\chi^{(1)} = (\epsilon^{(1)} - 1)/4\pi$  ( $\epsilon^{(1)}$  is the dielectric permittivity of the medium), we obtain the well-known Lorentz–Lorenz (or Clausius–Mossotti) relation

$$\frac{\epsilon^{(1)} - 1}{\epsilon^{(1)} + 2} = \frac{4\pi}{3}N\alpha. \quad (1.12)$$

Through rearrangement of Eq. (1.12), we can express the linear susceptibility as

$$\chi^{(1)} = \frac{\epsilon^{(1)} + 2}{3}N\alpha. \quad (1.13)$$

Substituting the expression (1.13) into (1.10), then (1.10) into (1.8), and using the relationship (1.7) between the local field and the dipole moment, we obtain the equation relating the local field to the average field:

$$\tilde{\mathbf{E}}_{\text{loc}} = \frac{\epsilon^{(1)} + 2}{3}\tilde{\mathbf{E}}. \quad (1.14)$$

The factor

$$L = \frac{\epsilon^{(1)} + 2}{3} \quad (1.15)$$

is known in the literature as the Lorentz local-field correction factor. The expression (1.15) for the local-field correction factor is valid in the case of homogeneous media, where all the particles (molecules or atoms) are of the same sort. It is also valid in materials where the emitters enter as inclusions that do not influence the correlation between the host molecules or atoms [12, 20].

### Onsager Model

A different macroscopic model for describing the local field in homogeneous media had been developed by Onsager [38]. In his study, Onsager treats a molecule or atom as being enclosed in a tiny real cavity in the medium. Then the field acting on the molecule is divided into the cavity field, which would exist at the center of the real cavity surrounding the molecule in the absence of the molecule, and the reaction field, which corrects the cavity field for the polarization of the surrounding medium by the dipole field of the molecule in the cavity. The resulting local field is given by

$$\tilde{\mathbf{E}}_{\text{loc}} = \frac{3\epsilon}{2\epsilon + 1} \tilde{\mathbf{E}} + \frac{2(\epsilon^{(1)} - 1)}{(2\epsilon^{(1)} + 1)a^3} \tilde{\mathbf{p}} \quad (1.16)$$

with the first and second terms expressing the cavity and reaction fields, respectively. Here  $a$  is the cavity radius. Even though the Lorentz and Onsager models yield different expressions for the local field, microscopic theories, developed in [12] and [39], reconcile those two models, which appear to be two special cases of the more general theories.

In reality, there is no need to apply a full microscopic treatment of local-field effects in order to describe an experimental outcome. In most of the cases, one of the two macroscopic theories works reasonably well. Onsager model is applicable to polar liquids, while the Lorentz model is applicable to solids and non-polar liquids. Both models can describe a guest-host system. The Lorentz model describes such a system in cases when the guest's molecule or atom replaces a molecule or atom of the host with similar polarizability [12]. An example is neodymium-doped YAG where neodymium guest ions replace yttrium ions in the crystalline structure. Both neodymium and yttrium belong to the class of rare-earth metals, which implies that they have similar properties. Onsager model is more suitable when the polarizability of a guest is significantly different from that of the host molecules or atoms. Then the guest not only forms a cavity in the host medium, but affects the local field outside the cavity [38, 40]. A good example of such a guest-host system is provided by liquid solutions of fullerene  $C_{60}$  [40].

### **Real-Cavity Model**

Real-cavity model is a simplified version of the Onsager model of local field. Like in the Onsager model, within the real-cavity model one considers an emitter as being inserted into a tiny cavity inside a dielectric medium [11]. The cavity is assumed to have no material in it except for the emitting dipole under consideration. This situation can be realized in the case when the polarizability of the emitter is low,



so that it does not impose strong changes on the local field outside the cavity. The expression for the local field, given by the real-cavity model, has the form

$$\tilde{\mathbf{E}}_{\text{loc}} = \frac{3\epsilon^{(1)}}{2\epsilon^{(1)} + 1} \tilde{\mathbf{E}}, \quad (1.17)$$

and the corresponding local-field correction factor is given by [11]

$$L = \frac{3\epsilon^{(1)}}{2\epsilon^{(1)} + 1}. \quad (1.18)$$

Comparing Eqs. (1.16) and (1.17), it is easy to see that within the real-cavity model one neglects the reaction field. Despite this approximation, real-cavity model describes many experimental outcomes reasonably well, which we show in Chapter 2.

### 1.3.2 Local Field and Cascading in Nonlinear Optics

Local-field effects lead to a modification of the optical properties of dense media, and, consequently, serve as a source of interesting new nonlinear optical phenomena. For instance, steady-state solutions to the local-field-corrected Maxwell–Bloch equations indicate that it is possible to realize mirrorless optical bistability [41–44]. Also, an additional inversion-dependent frequency shift appears. This frequency shift, called the Lorentz red shift, was experimentally measured in the reflection spectrum of a dense alkali vapor [45, 46]. The Lorentz red shift can cause a pulse to acquire a dynamic chirp, which enables soliton formation at a very low level of atomic excitation [47, 48].

In a collection of three-level atoms, local-field effects can lead to inversionless gain and the enhancement of the absorptionless refractive index by more than two orders of magnitude [49–52]. Successful experimental attempts to realize this enhancement of the refractive index have been reported [53, 54].

A phenomenological approach to treating local-field effects in nonlinear optics was proposed by Bloembergen [55]. He found that the local-field-corrected second-order nonlinear susceptibility scales as three powers of the local-field correction factor  $L$ . It has been understood that Bloembergen’s result can be generalized to a higher-order nonlinearity, and that the corresponding  $i$ th-order nonlinear susceptibility should scale as  $L^{i+1}$  (see, for example, [56, 57]). In Chapter 3 we show theoretically that Bloembergen’s approach, when consistently applied, actually leads to a much more complicated form for the nonlinear susceptibility. This is due to the presence of a cascaded nonlinear effect.

Cascading is a process in which a lower-order nonlinear susceptibility contributes to higher-order nonlinear effects in a multi-step fashion; it has been a field of interest in nonlinear optics for some time. Macroscopic cascading has a non-local nature, in that the intermediate field generated by a lower-order nonlinearity propagates to contribute to a higher-order nonlinear process by nonlinearly interacting with the fundamental field [58–67]. Thus, it has been acknowledged that the experimentally-measured third-order susceptibility can include contributions proportional to the square of the second-order susceptibility [58–60]. On the other hand, it has also been shown that nonlinear

cascading is possible due to the local nature of the field acting on individual molecules in the medium [60, 68–73]. This local-field-induced “microscopic” cascading does not require propagation, and has a purely local character.

The fact that local-field effects create cascaded contributions of the lowest order hyperpolarizability  $\gamma_{\text{at}}^{(2)}$  to the third-order susceptibility was first demonstrated by Bedeaux and Bloembergen [68]. They presented a general relationship between macroscopic and microscopic nonlinear dielectric response, obtained neglecting the pair correlation effect, which was later taken into account by Andrews *et al.* [72]. All the studies conducted thus far have concentrated on treating the local cascading contribution of  $\gamma_{\text{at}}^{(2)}$  to third-order nonlinear effects, which only arises if the constituent molecules lack center of inversion symmetry. We show in Chapter 3 both theoretically and experimentally that the microscopic cascading effects can be significant in higher-order nonlinearities, and are present in any system with the nonlinear response higher than the lowest-level.

Together with the fundamental interest to the microscopic cascading effect, there is a practical significance for its detailed investigation. Many studies in quantum information science require materials that can respond to the simultaneous presence of  $N$  photons, as in  $N$ -photon absorption. Usually, lower-order nonlinearities are stronger than higher-order nonlinearities. Microscopic cascading allows to synthesize higher-order nonlinearities out of lower-order nonlinearities by means of local-field effects, and, therefore, has a potential in application for high-order nonlinear optical

materials.

## 1.4 Lorentz–Maxwell–Bloch Equations

Within the next two chapters, we will extensively use Maxwell–Bloch equations with the Lorentz model used for accounting for local-field effects. We call this formalism “Lorentz–Maxwell–Bloch Equations.” We find it informative to describe the formalism in the current chapter.

A collection of two-level atoms with ground and excited states denoted respectively by  $a$  and  $b$ , interacting with an optical field closely tuned to an atomic resonance of the system, can be described by the Maxwell–Bloch equations [41, 56]

$$\dot{\sigma} = \left( i\Delta - \frac{1}{T_2} \right) \sigma - \frac{1}{2} i\kappa E w \quad (1.19a)$$

and

$$\dot{w} = -\frac{w - w_{\text{eq}}}{T_1} + i(\kappa E \sigma^* - \kappa^* E^* \sigma). \quad (1.19b)$$

Here  $E(t)$  is the slowly varying amplitude of the macroscopic electric field  $\tilde{E}(t) = E(t) \exp(-i\omega t) + \text{c. c.}$ , and the total (linear and nonlinear) polarization  $\tilde{P}(t) = P(t) \exp(-i\omega t) + \text{c. c.}$  involves

$$P(t) = N\mu^* \sigma(t), \quad (1.20)$$

where  $N$  is the number density of atoms,  $\mu$  is the dipole transition moment of the two-level system from the ground to excited state, and  $\sigma(t)$  is the slowly-varying amplitude of coherence  $\tilde{\sigma}(t)$ , that is,

$$\tilde{\sigma}(t) = \sigma(t) \exp(-i\omega t). \quad (1.21)$$

In Eqs. (1.19),  $\kappa = 2\mu/\hbar$ ,  $\Delta = \omega - \omega_{ba}$  is the detuning of the optical field frequency  $\omega$  from the atomic resonance frequency  $\omega_{ba}$ ,  $T_1$  and  $T_2$  are respectively the population and coherence relaxation times,  $w$  is the population inversion, and  $w_{\text{eq}}$  is its equilibrium value. According to the prescription of Lorentz [5], the field that appears in Eqs. (1.19) is actually the local field  $E_{\text{loc}}$ , given by Eq. (1.6). Substituting Eq. (1.6) into the Maxwell–Bloch Eqs. (1.19), we obtain

$$\dot{\sigma} = \left( i\Delta + i\Delta_L w - \frac{1}{T_2} \right) \sigma - \frac{1}{2} i\kappa w E \quad (1.22a)$$

and

$$\dot{w} = -\frac{w - w_{\text{eq}}}{T_1} + i(\kappa E \sigma^* - \kappa^* E^* \sigma). \quad (1.22b)$$

The term  $\Delta_L w$  entering the equation for  $\sigma$  introduces an inversion-dependent frequency shift, which is a consequence of local-field effects; the quantity  $\Delta_L$  is called Lorentz red shift and is given by

$$\Delta_L = -\frac{4\pi N |\mu|^2}{3 \hbar}. \quad (1.23)$$

The steady-state solutions to Eqs. (1.22) are

$$w = \frac{w_{\text{eq}}}{1 + \frac{|E|^2/|E_s^0|^2}{1 + T_2^2(\Delta + \Delta_L w)^2}} \quad (1.24a)$$

and

$$\sigma = \frac{\mu}{\hbar} \frac{wE}{\Delta + \Delta_L w + i/T_2}. \quad (1.24b)$$

In (1.24a) we introduced saturation field strength  $E_s^0$ , defined as

$$|E_s^0|^2 = \frac{\hbar^2}{4T_1 T_2 |\mu|^2}. \quad (1.25)$$

The total polarization can be expressed in terms of the total susceptibility  $\chi$ , including linear and nonlinear optical response, as  $P = \chi E$ . From (1.20), we find that

$$\chi = \frac{P}{E} = \frac{N\mu^* \sigma}{E}. \quad (1.26)$$

Substituting the steady-state solution for the coherence  $\sigma$  in the form (1.24b) into Eq. (1.26), we obtain

$$\chi = \frac{N|\mu|^2 T_2}{\hbar} \frac{w}{T_2(\Delta + \Delta_L w) + i}. \quad (1.27)$$

We use the results presented in this Section for describing laser gain properties of composite optical materials in Chapter 2, and as an approach to treat the microscopic cascading in high-order nonlinear response in Chapter 3.

## 1.5 Dye-Doped Cholesteric Liquid Crystal Lasers

Dye-doped cholesteric liquid crystals (CLCs) are self-assembling mirrorless distributed-feedback low-threshold laser structures. The idea of lasing in CLCs was first proposed by Goldberg and Schnur in 1973 [74]. Independently, Kukhtarev proposed the idea and developed a theory of CLC distributed feedback lasers in 1978 [75]. First experimental observation of lasing action in CLCs and a number of follow-up experiments were performed by Ilchishin, *et al.* [76–78] in 1980, almost twenty years before the nature of lasing in CLCs at the photonic band edge was explained by Kopp, *et al.* [79]. Taheri, *et al.* [80] reported the observation of laser action in CLC structures shortly after Kopp. CLC lasers became a subject of a great interest over the past decade. They combine tunability of dye lasers together with compactness and robustness of semiconductor lasers. Because of their small size, tunability, and low-cost fabrication, these lasers have a great potential to be used in medicine and LCD technology.

Cholesteric liquid crystal structures are produced by mixing a nematic liquid crystal with a chiral additive that causes the nematic-like ordered molecules to arrange themselves into a helical structure. In the planes perpendicular to the helical axis of the structure the molecules have a nematic-like order, aligning along some preferred direction. This direction can be characterized by a unit vector called local director. The local director rotates from plane to plane as we look along the helical axis of the CLC structure. The distance along the helical axis needed for the director to complete a full circle is called helical pitch  $P$ .

Alignment of the rod-shaped molecules along a preferred direction causes the CLC structures to exhibit local birefringence. The refractive indices “seen” by the light polarized along the local director and in perpendicular direction are called extraordinary ( $n_e$ ) and ordinary ( $n_o$ ), respectively. When circularly polarized light with the same handedness as that of the helical structure propagates along the CLC helical axis, it sees a periodic modulation of the refractive index and a selective reflection, if the wavelength of the light is in a certain range. This range is defined by the pitch of the CLC according to

$$\Delta\lambda = P\Delta n, \quad (1.28)$$

where

$$\Delta n = n_e - n_o. \quad (1.29)$$

Thus, a CLC can be regarded as a 1D photonic crystal with the center of the photonic band gap defined by the wavelength

$$\lambda_c = nP, \quad (1.30)$$

where

$$n = \frac{n_o + n_e}{2} \quad (1.31)$$

is the average of the refractive indices of the CLC. Propagation of circularly polarized light with the handedness opposite to that of the CLC is unaffected by the structure



and experiences merely the average refractive index  $(n_o + n_e)/2$ . Here we call a circularly polarized wave right-handed if its electric field vector appears to rotate clockwise as the wave propagates towards an observer, and left-handed if its electric field vector rotates counter-clockwise. This is a standard definition of handedness of circularly polarized light [34].

If one dopes a CLC structure with an organic dye that has the emission spectrum overlapping with the CLC photonic band gap, one can observe changes in photoluminescence of the dye. The emission will be enhanced at the low- and high-frequency photonic band edges and suppressed at the band gap for the circularly polarized component with the same handedness as that of the CLC structure. The sharp rise of the photoluminescence at the band edges is due to the fact that the density of states is very high at these spectral ranges. The circularly polarized photoluminescence with the opposite handedness does not experience any changes in the CLC.

A CLC host can serve as a resonator for a laser dye doped into it. The enhancement of the dye photoluminescence at the band edges, caused by high density of electromagnetic states, leads to easily achievable low-threshold lasing [79]. The two lasing modes having the lowest threshold are situated at the band edges. The mode on the low-frequency band edge is comprised of two circularly polarized counter-propagating waves, resulting in a standing wave with the electric field vector aligned along the local director (provided that  $n_o < n_e$ ) [81]. The mode at the high-frequency band edge is similar to that at the low-frequency edge, except in this case the electric

field vector is perpendicular to the local director. Depending on the mutual alignment of the dye transition dipole moment and the local director, lasing oscillations can occur at the low-frequency, high-frequency, or at both band edges [81, 82].

There are several ways to characterize the orientation of the dye dipole moment with respect to the local director [81–84]. The most widely used characteristic is the dye emission order parameter  $S_{\text{em}}$ , given by the expression

$$S_{\text{em}} = \frac{I_{\parallel} - I_{\perp}}{I_{\parallel} + 2I_{\perp}}, \quad (1.32)$$

where  $I_{\parallel}$  is the fluorescence intensity of the nematic liquid crystal phase doped with the dye, measured for the radiation with the electric field parallel to the director, and  $I_{\perp}$  is the fluorescence intensity for the radiation with the electric field polarized perpendicular to the director. Obviously, the case  $S_{\text{em}} = 1$  corresponds to a perfect alignment of the dye dipole moment along the liquid crystal director, the case  $S_{\text{em}} = -1/2$  corresponds to a perfect alignment of the dye dipole moment perpendicular to the director, and the case  $S_{\text{em}} = 0$  corresponds to an isotropic orientation. In our work reported in Chapter 4, we use the characteristic given by Eq. (1.32) to describe the dye dipole moment alignment.

## 1.6 Planar Chiral Structures

A planar object is said to be chiral if it cannot be brought in congruence with its mirror image unless it is lifted from the plane [85]. Here we will distinguish between two forms of planar chirality: “molecular” and “structural.” The molecular chirality is a property of an individual particle to lack mirror symmetry (an example of such a particle is a gammadion), while the structural chirality is a property of the entire structure. For example, an array of particles possessing molecular chirality is, in whole, structurally chiral. Even a regular array of achiral particles can possess structural chirality, if the particles are arranged in such a way that the whole structure lacks mirror symmetry.

The observation of the chirality-sensitive diffraction in planar arrays of chiral gold nanoparticles by Papakostas *et al.* [85] has attracted a lot of attention to the interaction of light with artificial planar chiral structures. Because of their ability to change the polarization state of diffracted [85–89] and transmitted [90, 91] light, artificial planar chiral structures have a great potential of being used as polarization control devices. It has been shown that such structures can demonstrate specific optical activity three orders of magnitude stronger than that produced by quartz [90]. Polarization conversion and focusing of circularly-polarized light on transmission through a gammadion-shaped hole and arrays of chiral particles have been demonstrated both numerically [92–94] and experimentally [95]. The issue of temporal reversibility and spatial reciprocity in planar chiral structures has been a subject of a great contro-

versy [89,90,95–97]. Another property contributing to the practical importance of the artificial planar structures is their ability to display unusual nonlinear optical properties because of their broken symmetry imposed by the chirality itself or by small-scale irregularities. In particular, it has been shown by Canfield *et al.* [98–102] that the smallest manufacturing defects in the arrays of gold L-shaped nanoparticles can result in drastic enhancement of second-harmonic generation, and even in appearance of forbidden tensor components in second-harmonic output.

So far, in all the experimental investigations of the polarization changes of light in transmission [90,91] and diffraction [85–89] by planar chiral structures, the focus was made on studying the structures with chiral individual particles. To the best of our knowledge, there are no experimental studies of polarization changes in artificial planar structures with *achiral* particles arranged in a chiral fashion.

In Chapter 5 we report the observation of polarization changes in diffraction from periodic patterns with pure structural chirality. The polarization effects were found to be large, in fact, as large as those observed from reference patterns consisting of chiral particles. The results suggest that structural and molecular chirality are indistinguishable and cannot be separated from each other in diffraction experiments. Indeed, both cases lead to the lack of mirror (and point inversion) symmetry in the experimental geometry, making the whole setup “chiral.” The role of the chiral setup is further emphasized by the fact that our results can be explained by considering scattering from individual particles.

Here I have presented an overview of all projects that I have been working on during my Ph. D. research, and the basic concepts that these projects rely on. More details and my contributions in particular can be found in separate chapters devoted to the projects.

# Chapter 2

## Composite Laser Materials

### 2.1 Introduction

Nanocomposite materials can differ significantly in their optical properties from bulk constituent materials [9, 10, 25, 29, 103], and their growing importance in photonics calls for a better understanding and characterization of the role of local-field and other effects that influence their optical properties.

There are numerous works describing the nonlinear optical properties of composite materials [25–28]. However, there has not been a systematic study yet of their laser properties. In this chapter we present a study of the influence of the local-field effects on the laser properties of composite materials. We first present a general picture of the idea of composite laser in Section 2.2, and show the significance of the local-field effects in modifying laser properties. In Section 2.3 we present our experimental

study of the radiative lifetime of Maxwell Garnett-type composite materials based on liquid suspensions of Nd:YAG nanoparticles. We show that local-field effects can significantly vary the radiative lifetime of Nd:YAG. Local-field effects can come into play differently in different composite geometries, and separate theoretical studies of the laser properties of various composite geometries are needed. In Section 2.4 we present such studies for Maxwell Garnett and layered composite geometries. Finally, in Section 2.5 we summarize our theoretical and experimental studies of composite laser materials.

## 2.2 The Idea of Composite Lasers

In this section, we limit ourselves to a simple treatment of a composite material as a uniform medium characterized by a dielectric constant  $\epsilon_{\text{eff}}$ . At the present level of approximation, the Lorentz model can be used to describe the effects of the local field on the laser properties of the medium. We recall for convenience the expression for the Lorentz local field from Eq. (1.6),

$$\tilde{\mathbf{E}}_{\text{loc}} = \tilde{\mathbf{E}} + \frac{4\pi}{3}\tilde{\mathbf{P}}, \quad (2.1)$$

and the Lorentz local-field correction factor from Eq. (1.15),

$$L = \frac{\epsilon^{(1)} + 2}{3}, \quad (2.2)$$

relating the local and average fields by Eq. (1.5). As we pointed out in Section 1.2, composite materials can be treated as effective media, as the sizes of the particles of the constituent components are much smaller than the optical wavelength. Under this condition we can consider a composite material as an effective medium characterized by an effective (average) dielectric constant  $\epsilon_{\text{eff}}$ . Thus, at the present level of approximation, we can use Eq. (2.2) for the local-field correction factor with the effective dielectric constant in place of  $\epsilon^{(1)}$ .

### 2.2.1 Influence of Local-Field Effects on Laser Properties of Dielectric Materials

In this subsection we describe the modification of laser properties, such as the radiative lifetime, the small-signal gain coefficient, and the saturation intensity by the local-field effects. We undertake our analysis based on a simple argument of the validity of the Lorentz model for treating the local-field effects.

#### Radiative Lifetime

The radiative lifetime  $\tau$  of emitters in a dielectric material depends on the dielectric constant of the material. It is inversely proportional to the Einstein  $A$  coefficient, which, in turn, can be expressed through Fermi's golden rule as

$$A = \frac{1}{\tau} = \frac{2\pi}{\hbar} |V_{12}(\omega_0)|^2 \rho(\omega_0). \quad (2.3)$$



Here  $V_{12}(\omega_0)$  is the energy of interaction between the emitter and the electric field in the medium, and  $\rho(\omega_0)$  is the density of states at the emission frequency  $\omega_0$ . In a medium with refractive index  $n_{\text{eff}}$  in which the local-field effects are significant, the interaction energy scales as

$$V_{12,\text{loc}} \propto \frac{L}{\sqrt{n_{\text{eff}}}}. \quad (2.4)$$

The factor  $L$  enters the expression for the local-field-corrected interaction energy  $V_{12,\text{loc}}(\omega_0)$  because the local field acting on an individual emitter differs from the macroscopic average field. The factor  $\sqrt{n_{\text{eff}}}$  in the denominator of (2.4) comes from the mode normalization and thus appears in the expression for the electromagnetic energy density in a dielectric medium [13]. The density of states in the medium is proportional to the square of the effective refractive index:

$$\rho(\omega_0) \propto n_{\text{eff}}^2. \quad (2.5)$$

Using Eqs. (2.3) through (2.5), we can conclude that the local-field-corrected spontaneous emission rate  $A_{\text{loc}}$  in the medium with refractive index  $n_{\text{eff}}$  is related to the spontaneous emission rate in the medium of unit refractive index (we call it  $A_{\text{vac}}$ ) as

$$A_{\text{loc}} = n_{\text{eff}} |L|^2 A_{\text{vac}}. \quad (2.6)$$

The relation (2.6) has been shown to hold also when the effect of dispersion is included in  $V_{12,\text{loc}}$  and in the density of states [13]. The corresponding relation for the local-

field-corrected radiative lifetime  $\tau_{\text{loc}}$  in terms of the “vacuum” lifetime  $\tau_{\text{vac}}$  takes form

$$\tau_{\text{loc}} = \frac{\tau_{\text{vac}}}{n_{\text{eff}}|L|^2}. \quad (2.7)$$

Here and in all later sections of this chapter we assign the “vac” subscript to the variables denoting quantities in a medium with the same chemical environment as that of the dielectric medium under consideration, but with the refractive index equal to unity. The variables marked with the “loc” subscript denote the local-field-corrected quantities.

### Small-Signal Gain

Most laser gain media can be modeled as collections of two-level atoms, regardless of what the actual level diagram of the active medium is, because in most cases the nonradiative transitions are much faster than the radiative transition from the upper laser level. We use the two-level-atom model to derive the expression for the local-field-corrected small-signal gain.

We start from the driven wave equation

$$-\nabla^2 \tilde{E} + \frac{1}{c^2} \frac{\partial^2 \tilde{E}}{\partial t^2} = -\frac{4\pi}{c^2} \frac{\partial^2 \tilde{P}}{\partial t^2}. \quad (2.8)$$

(We limit ourselves to considering scalar fields for simplicity.) Here

$$\tilde{E}(t) = E(z)e^{-i\omega t} + \text{c. c.} = A_0 e^{i(\bar{k}z + \omega t)} + \text{c. c.} \quad (2.9)$$

is the average electric field. In the general case of a lossy or amplifying medium, the parameter  $\bar{k}$  is complex:  $\bar{k} = k + i\alpha_0/2$ . The real part of  $\bar{k}$  is the wave number,

$$\text{Re}(\bar{k}) \equiv k = \frac{\omega n_{\text{eff}}}{c}, \quad (2.10)$$

where  $n_{\text{eff}}$  is the effective refractive index of the medium, while the imaginary part of  $\bar{k}$  characterizes amplification or attenuation in the medium, according to

$$\text{Im}(\bar{k}) = \frac{1}{2}\alpha_0 = -\frac{1}{2}g_0. \quad (2.11)$$

Here  $\alpha_0$  and  $g_0$  are the small-signal intensity absorption and gain coefficients, respectively. We seek the solution for the local-field-corrected small-signal gain coefficient, which we denote as  $g_{0,\text{loc}}$ .

We take the polarization  $\tilde{P}$  entering the wave equation (2.8) to be linear:

$$\tilde{P} = \chi_{\text{loc}}^{(1)} \tilde{E}, \quad (2.12)$$

where  $\chi_{\text{loc}}^{(1)}$  is the local-field-corrected linear susceptibility. Using Eq. (1.27) for the susceptibility of a collection of two-level atoms and neglecting the nonlinear depen-

dence on the electric field, we obtain [56]

$$\chi_{\text{loc}}^{(1)} = -\frac{c\alpha_{0,\text{vac}}(\Delta)}{4\pi\omega_{ba}}L(T_2\Delta - i), \quad (2.13)$$

where  $\omega_{ba}$  is the frequency of the atomic transition,  $\Delta = \omega - \omega_{ba}$  is the detuning of the optical field with respect to the atomic transition frequency, and  $T_2$  is the coherence relaxation time. The “vacuum” absorption  $\alpha_{0,\text{vac}}(\Delta)$  experienced by a weak optical wave detuned from the resonance is given by [56]

$$\alpha_{0,\text{vac}}(\Delta) = -\frac{4\pi\omega_{ba}}{c} \frac{Nw_{\text{eq}}|\mu_{ba}|^2T_2}{\hbar(T_2^2\Delta^2 + 1)}, \quad (2.14)$$

where  $w_{\text{eq}}$  is the equilibrium value of the population inversion,  $N$  is the atomic number density, and  $\mu_{ba}$  is the transition dipole moment of the two-level atom.

The local-field correction factor  $L$ , given by Eq. (2.2) as  $L = (\epsilon_{\text{eff}} + 2)/3$ , can be shown to take the form

$$L = \frac{T_2\Delta + i}{T_2(\Delta - \Delta_L) + i}, \quad (2.15)$$

if one chooses to express  $\epsilon_{\text{eff}}$  in terms of atomic parameters as [5, 45]

$$\epsilon_{\text{eff}} = 1 - \frac{fr_e\lambda_0cN}{\Delta - \Delta_L + i/T_2}. \quad (2.16)$$

Here  $\Delta_L = -(fr_e\lambda_0cN)/3$  is the Lorentz red shift [45] ( $f$  is the oscillator strength of the atomic transition,  $r_e = e^2/mc^2$  is the classical electron radius, and  $\lambda_0$  is vacuum

transition wavelength). The Lorentz red shift appears in the expression for  $\epsilon_{\text{eff}}$  as a consequence of the local-field effects and leads to  $L \neq 1$  (note that if  $\Delta_L = 0$ , then  $L = 1$ , and there are no local-field effects).

Substituting the electric field given by Eqs. (2.9) through (2.11) and the polarization in the form of Eq. (2.12) into the wave equation (2.8), then taking the time and space derivatives and dropping the electric field that appears as a multiplicative factor on the both sides of the resulting equation, we end up with the equation

$$g_{0,\text{loc}} = -\frac{4\pi k}{n_{\text{eff}}^2} \text{Im} \left[ \chi_{\text{loc}}^{(1)} \right] \quad (2.17)$$

for the gain coefficient. Substituting the factor  $L$  given by (2.15) into the expression (2.13) for the linear susceptibility, and then (2.13) into (2.17), we arrive at the expression

$$g_{0,\text{loc}}(\Delta) = -\frac{\alpha_{0,\text{vac}}(\Delta)}{n_{\text{eff}}} \frac{\omega}{\omega_{ba}} |L|^2 = \frac{g_{0,\text{vac}}(\Delta)}{n_{\text{eff}}} \frac{\omega}{\omega_{ba}} |L|^2 \quad (2.18)$$

for the local-field-corrected small-signal gain in terms of the “vacuum” absorption coefficient  $\alpha_{0,\text{vac}}(\Delta)$ , or “vacuum” gain coefficient  $g_{0,\text{vac}}(\Delta)$  (*i. e.*, the absorption or gain coefficient in a medium with the unit refractive index). Assuming that the optical wave is in resonance with the atomic transition ( $\Delta = 0$ ), we find the following expression for the local-field-corrected gain coefficient:

$$g_{0,\text{loc}}(0) = \frac{g_{0,\text{vac}}(0)}{n_{\text{eff}}} |L|^2. \quad (2.19)$$

It is in agreement with that obtained by Milonni [13].

### Saturation intensity

In this subsection we use the following convention regarding the way we denote different variables. We assign the “vac” subscript to the variables describing quantities in a medium with unit refractive index, no subscripts to variables denoting non-local-field-corrected quantities in a medium with the refractive index  $n_{\text{eff}}$ , and the “loc” subscript to variables denoting local-field-corrected quantities.

The gain  $g$  for a homogeneous atomic transition saturates with increasing signal intensity  $I = (n_{\text{eff}}c|E|^2)/(2\pi)$  according to [104]

$$g = \frac{g_0}{1 + I/I_s}. \quad (2.20)$$

The saturation intensity is the intensity that reduces the small-signal gain coefficient to a half of its value; it is given in terms of the atomic transition parameters by [56]

$$I_s = \frac{cn_{\text{eff}}}{2\pi} \frac{\hbar^2}{4|\mu_{ba}|^2 T_1 T_2}. \quad (2.21)$$

Here  $T_1$  is the population relaxation time.

To account for local-field effects in Eq. (2.20) for saturated gain coefficient, one has to substitute the local-field-corrected counterparts of the quantities entering the equation. We have obtained an equation for the local-field-corrected small-signal gain

coefficient  $g_{0,\text{loc}}$  (see Eq. (2.19)). The local-field-corrected intensity can be written as

$$I_{\text{loc}} = \frac{n_{\text{eff}}c}{2\pi} |E_{\text{loc}}|^2 = \frac{n_{\text{eff}}c}{2\pi} |L|^2 |E|^2 = |L|^2 I. \quad (2.22)$$

The expression (2.21) for the saturation intensity contains two quantities that may be affected by local-field effects, namely:  $T_1$  and  $T_2$ . We assume that  $T_2$  does not depend on the local-field correction factor, as would be true for many line broadening mechanisms. Thus, we can simply retain the “vacuum” value of  $T_2$  in the equation for the saturation intensity.  $T_1$  is the lifetime of the upper laser level, which we assume to be purely radiative. Thus, the result (2.7) obtained earlier applies:

$$T_{1,\text{loc}} = \frac{T_{1,\text{vac}}}{n_{\text{eff}}|L|^2}. \quad (2.23)$$

Making use of Eq. (2.23) and the assumption that  $T_2$  does not introduce local-field correction to the expression for the saturation intensity, we find that

$$I'_s = \frac{cn_{\text{eff}}}{2\pi} \frac{\hbar^2}{4|\mu_{ba}|^2 T_{1,\text{loc}} T_{2,\text{vac}}} = \frac{cn_{\text{eff}}}{2\pi} \frac{\hbar^2 n_{\text{eff}} |L|^2}{4|\mu_{ba}|^2 T_{1,\text{vac}} T_{2,\text{vac}}}. \quad (2.24)$$

In Eq. (2.24) we denote the saturation intensity  $I'_s$  in order to discriminate it from both the non-local-field-corrected saturation intensity  $I_s$  and the local-field-corrected saturation intensity  $I_{s,\text{loc}}$ , as we did not account for all the local-field corrections affecting the saturation intensity yet.

The local-field-corrected saturated gain coefficient can be written as

$$g_{\text{loc}} = \frac{g_{0,\text{loc}}}{1 + \frac{I_{\text{loc}}}{I_s}} \quad (2.25)$$

in terms of the quantities given by Eqs. (2.19), (2.22), and (2.24). We define the local-field-corrected saturation intensity so that, if written in terms of it, Eq. (2.25) takes the form

$$g_{\text{loc}} = \frac{g_{0,\text{loc}}}{1 + \frac{I}{I_{s,\text{loc}}}}. \quad (2.26)$$

Making use of Eqs. (2.24) through (2.26), we express the local-field-corrected saturation intensity in terms of the “vacuum” saturation intensity as

$$I_{s,\text{loc}} = n_{\text{eff}}^2 I_{s,\text{vac}}. \quad (2.27)$$

## 2.2.2 Analysis

The basic operation of lasers can be characterized most simply in terms of the upper-level spontaneous emission lifetime  $\tau$ , the laser gain coefficient  $g$ , and the gain saturation intensity  $I_s$ . All three of these parameters can be controlled through use of a composite material geometry. In the simplest formulation of local-field effects, we can assume that these laser parameters depend only on the effective value  $n_{\text{eff}}$  of the refractive index of the host material. We showed in Subsection 2.2.1 that the basic



laser parameters scale with the effective refractive index according to

$$A_{\text{loc}} = n_{\text{eff}} |L|^2 A_{\text{vac}}, \quad (2.28a)$$

$$g_{0,\text{loc}} = \frac{|L|^2}{n_{\text{eff}}} g_{0,\text{vac}}, \quad (2.28b)$$

and

$$I_{\text{s,loc}} = n_{\text{eff}}^2 I_{\text{s,vac}}. \quad (2.28c)$$

The quantities marked with “vac” denote the values of the parameters in a medium with the same chemical environment, but with the refractive index equal to unity.

Treating the composite laser gain medium as an effective medium, and assuming that the amplification (and loss) at the laser transition frequency is small enough to neglect the imaginary part of the effective dielectric constant  $\epsilon_{\text{eff}}$ , we can express the local-field correction factor, given by Eq. (2.2), as

$$L = \frac{n_{\text{eff}}^2 + 2}{3}. \quad (2.29)$$

Making use of Eq. (2.29) for the factor  $L$ , we plot the local-field-corrected basic laser parameters, given by (2.28), in Figure 2.1. We choose the range of refractive indices available in dielectric composite materials. Clearly, significant control over the laser parameters is available through use of a composite geometry.

Control of the three laser parameters is crucial for the development of laser systems

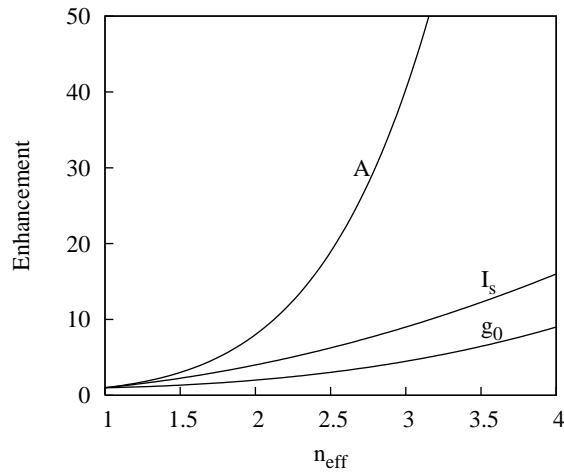


Figure 2.1: Variation of the principal parameters that control the basic operation of a laser with the effective refractive index of the composite material.

for the following reasons.

1. The upper state lifetime controls how large the pumping rate of the laser needs to be in order to establish a population inversion.
2. The gain coefficient determines the laser threshold condition. The gain needs to be large enough for the laser to reach threshold, but it is not desirable for the gain to be too large because excessive gain can lead to the development of parasitic effects such as amplified spontaneous emission.
3. The saturation intensity (and its related energy quantity, the saturation fluence) determine the output power of a laser, from the point of view that the output power is determined by the condition that the saturated round-trip gain must equal the round trip loss. In practice, the output intensity of most lasers is typically a factor of several times the saturation intensity.

Our assumption that local-field effects in composite laser gain media can be accounted for by using the Lorentz model with the effective refractive index entering the expression for the factor  $L$  is good for conceptual understanding of how the local-field effects help one to manipulate the laser parameters. We refer readers to Section 2.4 for a more precise and detailed analysis of Maxwell Garnett and layered composite geometries.

The theoretical analysis presented in this section has been published in the Journal of the Optical Society of America B [105].

## **2.3 Influence of Local-Field Effects on the Radiative Lifetime of Liquid Suspensions of Nd:YAG Nanoparticles**

It is well known that the rate of spontaneous emission depends in general on the environment of the emitter. The case in which an excited atom is inside a cavity or near a reflecting surface has been studied extensively both theoretically and experimentally [106]. Radiative processes in bulk dielectric media appear to be less well understood at a fundamental level, and in particular there has been much current interest in the effects of local fields on spontaneous emission [12].

Recent experimental work includes measurements of the radiative lifetimes of  $\text{Eu}^{3+}$  complexes in liquids [16], supercritical gases [17], and glass [18, 19]. In this section we

present the results of measurements of radiative lifetimes of Nd:YAG nanopowders in different liquids. Unlike previous experiments in which the  $\text{Eu}^{3+}$  is embedded in a ligand cage, surface effects must be considered in the case of nanoparticles of the type used in our work. However, despite these complications, the experiments described in this section allow some important conclusions to be drawn about local-field effects. Also, composite materials of the sort studied here may prove useful in the development of photonic devices, and thus an understanding of their optical properties is especially important.

We recall from Section 2.2 that the radiative lifetime in a dielectric medium can be related to its vacuum counterpart as

$$\tau_{\text{loc}} = \frac{\tau_{\text{vac}}}{n_{\text{eff}}|L|^2} \quad (2.30)$$

(see also Eq. (2.7)). Existing theoretical models predict different expressions for the local-field correction factor  $L$ . Two models, describing most of the experimental outcomes, are the virtual-cavity model (Lorentz model) [37], and the real-cavity model [11] (see Section 1.3.1 for a more detailed overview). Within this section we will refer to Lorentz model as “virtual-cavity model” in order to emphasize its difference from the real-cavity model. Using the virtual-cavity approach, one arrives at the expression (2.29) for the local-field correction factor [5, 6]. Here we rewrite this expression as

$$L = \frac{n_{\text{eff}}^2 + 2}{3} \quad (2.31)$$

in terms of the effective refractive index of the composite dielectric medium. We also rewrite the expression for the local-field correction factor following from the real-cavity model (1.18) as

$$L = \frac{3n_{\text{eff}}^2}{2n_{\text{eff}}^2 + 1}. \quad (2.32)$$

The expressions (2.31) and (2.32) for the local-field correction factor are very different, and lead to different results for the radiative lifetimes in a dielectric medium. In fact, they describe different physical situations [12, 20]. The Lorentz model applies only to homogeneous dielectric media [45], while the real-cavity model can also describe the local-field effects in a medium where the emitters enter in the form of inclusions, or dopants, creating tiny real cavities. Examples where the latter model applies well are dye molecules dissolved in water droplets suspended in different liquids [21, 22],  $\text{Eu}^{3+}$  organic complexes suspended in liquids [16] and supercritical gas [17], liquid suspensions of quantum dots [23] (with the interpretation of the results given in Ref. [20]), and  $\text{Eu}^{3+}$  ions embedded into a binary glass system  $x\text{PbO} - (1 - x)\text{B}_2\text{O}_3$  [18, 19].

To the best of our knowledge, there is only one reported experiment on the investigation of local-field effects on the radiative lifetime of liquid suspensions of nanoparticles [107].<sup>1</sup> Based on the theoretical analysis conducted by P. de Vries and A. Lagendijk [12], and on numerous examples of similar experiments [16, 17, 21–23], one would expect the radiative lifetime of liquid suspensions of nanoparticles to obey the

---

<sup>1</sup>The composites containing  $\text{Eu}^{3+}$  embedded in a ligand cage [16, 17] are fundamentally different from the sort of nanocomposite material considered in [107] and in the present work.

real-cavity model. Indeed, when placed in a liquid, the nanoparticles create real cavities, replacing some volume of the liquid. It is therefore somewhat surprising that the experimental measurements of the radiative lifetime of  $\text{Eu}^{3+} : \text{Y}_2\text{O}_3$  nanoparticles in liquids, reported in Ref. [107], obeyed the virtual-cavity model. We believe that more experimental studies are needed for a better understanding of local-field effects in liquid suspensions of nanoparticles.

Measurements of the fluorescence lifetime in suspensions of neodymium-doped yttrium-aluminum garnet (Nd:YAG) particles as a function of the refractive index of the surrounding medium were reported in Ref. [108], but not under conditions allowing a study of the influence of local-field effects, which require the particles and the distances between the particles to be much less than the optical wavelength. The observed changes in the fluorescence lifetimes of the Nd:YAG particles were purely the effect of the change in the refractive index on the density of states. The average size of the particles used by the authors of Ref. [108] was on the order of a wavelength of light (several hundreds of nanometers), which made the suspensions of such particles unsuitable for measurements of local-field effects due to the host liquid.

In this section we present the results of measurements of the radiative lifetime of  $\text{Nd}^{3+}$ :YAG nanoparticles dispersed in different liquids. Our goal is to measure the change in the radiative lifetime of emitters <sup>2</sup> caused by local-field effects and to establish which model for the local-field correction factor works best for our case.

---

<sup>2</sup>In our work we consider the  $\text{Nd}^{3+}$ :YAG nanoparticles to be the emitters in our composite materials.

### 2.3.1 Sample Preparation and Experiment

The Nd:YAG nanopowder used in our experiments was manufactured by TAL Materials company. According to the SEM photograph of the nanopowder (see Fig. 2.2), the average particle diameter was around 20 nm. The neodymium concentration was chosen to be 0.9 at. %, which is the standard value for Nd:YAG laser rods. Because of aggregation it was necessary to use appropriate surfactants to obtain good liquid suspensions.

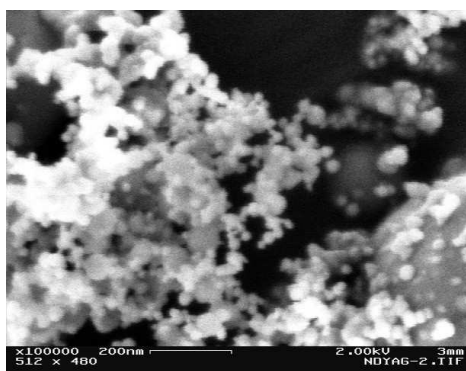


Figure 2.2: SEM picture of Nd:YAG nanopowder. The average particle size is 20 nm.

We used thirteen different organic and inorganic liquids for suspending the nanoparticles. The liquids and the corresponding values of their refractive indices are shown in Fig. 2.3. We used the Tween 80 surfactant for water and the aqueous immersion fluid manufactured by Cargille Laboratories, and 12-hydroxystearic acid for oil-based organic liquids (such as carbon tetrachloride and toluene). The aqueous suspensions were sonicated for five minutes, and the resultant dispersions were very stable; the nanoparticles remained in suspension for more than a month. A magnetic stirrer was

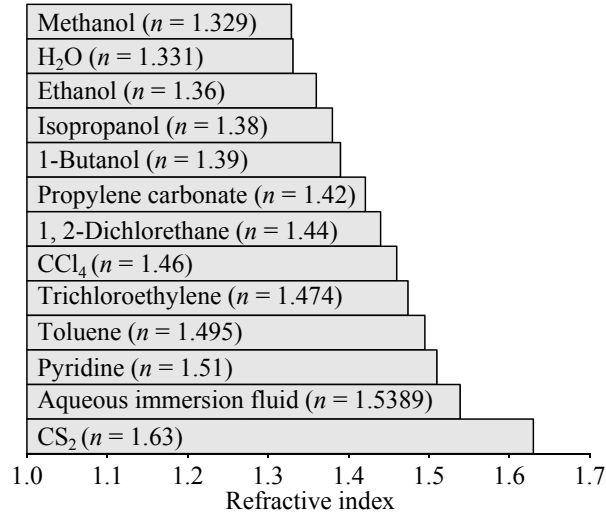


Figure 2.3: Liquids that we used for suspending Nd:YAG nanoparticles and the values of their refractive indices.

used to dissolve the surfactants and to suspend the nanoparticles in organic solvents. The most stable organic suspensions were achieved with alcohols, while the oil-based suspensions were only good enough for quick lifetime measurements and sedimented shortly after the measurements were done. The Nd:YAG volume fraction in all the samples was 0.11 vol. %.

As the volume fraction  $f_{\text{YAG}}$  of the nanoparticles in our samples is very low, we can treat our suspensions as Maxwell-Garnett-type composite materials, and use the relation (1.1) to calculate the effective refractive index  $n_{\text{eff}}$ , substituting the refractive index of the liquids in place of the host refractive index,  $n_{\text{h}}^2 = \epsilon_{\text{h}}$ , and the YAG refractive index in place of that of the inclusions,  $n_{\text{i}}^2 = \epsilon_{\text{i}}$ . The effective refractive indices of our samples are very close to the refractive indices of the liquids.

We used a Spectra Physics femtosecond laser system to optically excite neodymium



ions in the Nd:YAG nanoparticle suspensions. The scheme of the experimental setup is represented in Fig. 2.4. The radiation was generated by a mode-locked Tsunami

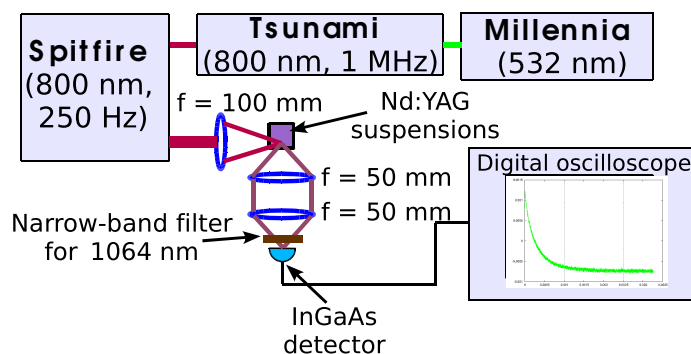


Figure 2.4: Experimental setup for measuring the radiative lifetime in liquid suspensions of Nd:YAG nanoparticles.

Ti:sapphire laser, providing 100-fs pulses with 800 nm central wavelength and an initial repetition rate of 80 MHz. The Tsunami laser output was sent to a Spitfire regenerative amplifier, and the repetition rate of the amplifier output was adjusted to 250 Hz, in order to provide enough time between successive pump pulses. The duration of the pulses exiting the regenerative amplifier was around 120 fs, and the pulse energy was close to 1 mJ. The pump radiation was focused into a cell containing the suspension by a lens with a focal length of 100 mm, and the fluorescence from the Nd:YAG nanoparticles was collected by a 50 mm  $\times$  50 mm condenser in a perpendicular geometry (see Fig. 2.4). A Thorlabs InGaAs detector and a Tectronix digital oscilloscope were used to observe and record the fluorescence decay curves. A narrow-band 10 nm FWHM filter with the central wavelength of 1064 nm, together with an additional long-pass filter, were placed in front of the detector to block scattered

pump radiation.

A typical time trace showing the fluorescence decay dynamics is shown in Fig. 2.5. In all our experiments we observed a non-exponential decay, and our data can be fitted

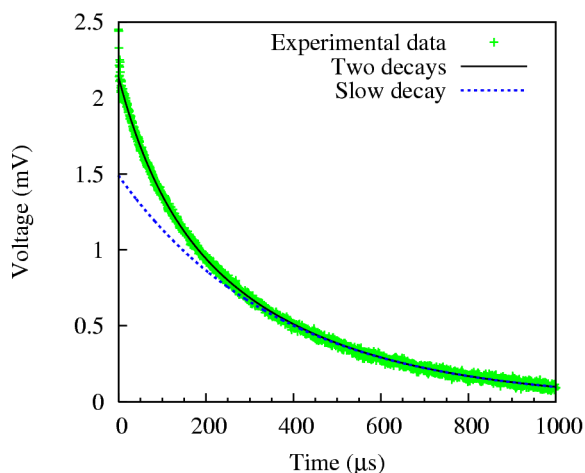


Figure 2.5: Typical fluorescence decay in the Nd:YAG nanopowder.

well with a sum of two exponentials with a 4:1 ratio of the slower to the faster decay times. All the slower decay exponentials have fluorescence decay times longer than the typical value  $230 \mu s$  for bulk Nd:YAG, while all the faster decay exponentials have decay times shorter than that of bulk Nd:YAG. We expect the fluorescence decay times in our Nd:YAG nanopowder suspensions to be longer than that in a bulk Nd:YAG crystal, because the effective refractive indices of our liquid suspensions (1.32–1.63) are smaller than the refractive index of a bulk Nd:YAG (1.82). This is one of the reasons why we chose the longer radiative decay time to be compared to different theories describing the local-field effects. Other reasons will be evident from our further analysis.

We performed a series of experiments to determine the origin of the shorter fluorescence decay component. Fluorescence decay dynamics similar to that shown in Figure 3 was previously observed in a bulk Nd:YAG crystal as a consequence of amplified spontaneous emission [109]. Measuring the fluorescence decay at different pump energies, we did not observe any variations in the two lifetimes and their corresponding amplitudes. We also observed no changes when we varied the geometry of the experiment. All this indicates that the amplified spontaneous emission is not the reason for the bi-exponential fluorescence decay dynamics in our experiments.

Another possible reason for the faster exponential in the fluorescence decay in our samples could be the contribution from ions sitting on the surfaces of the nanoparticles. In order to check this hypothesis, we measured the fluorescence lifetimes not only for the Nd:YAG nanopowder, but also for an Nd:YAG micropowder with a micrometer-scale particle size. We obtained the micropowder by crushing an Nd:YAG laser rod and grinding the pieces in a ball mill. The resultant decay dynamics displayed a bi-exponential character in both powders. The shorter decay time ( $130 \mu\text{s}$ ) was the same for both powders (within the error of our measurements), and the longer decay time was around  $600 \mu\text{s}$  for the nanopowder and more than two times shorter ( $270 \mu\text{s}$ ) for the micropowder. Furthermore, the relative contribution of the faster-decay exponential was much higher for the nanopowder, compared to the micropowder. The fact that the shorter lifetime is the same for both powders, and that the faster-exponential amplitude is relatively higher for the nanopowder, suggests

that the faster exponential in the fluorescence decay is due to the contribution from the  $\text{Nd}^{3+}$  ions sitting on the surfaces of the particles. Indeed, the structures of the surfaces of the nanoparticles and microparticles should be similar, while the relative surface area of the nanopowder is much larger than that of the micropowder. The crystal lattice surrounding of the surface ions is distorted, leading to the variations in their electric dipole moments and resulting in much shorter relative decay times. As surface effects are not the topic of our present research, we will concentrate on the analysis of the slower radiative decay component.

### 2.3.2 Data Analysis

The fluorescence lifetimes for the various host liquids (shown as points in Fig. 2.6) are obtained by fitting the time evolution of the fluorescence decay to the sum of two exponentials and taking the longer decay time as the relevant time for the reasons explained above. As the results of the fitting procedure were somewhat sensitive to the range of time values used in the fitting procedure, we repeated the fit for several different time ranges for each data point. The data points shown in Figure 2.6 represent averages of the results of these fits, and the error bars represent the standard deviations from the mean values.

The radiative lifetime of the nanoparticles can be expressed as a function of the

effective refractive index of their liquid suspensions by

$$\tau_{\text{rad}} = \frac{\tau_{\text{rad}}^{(\text{vac})}}{n_{\text{eff}} \left( \frac{n_{\text{eff}}^2 + 2}{3} \right)^2} \quad (2.33)$$

in the case when the local-field effects obey the Lorentz model, and by

$$\tau_{\text{rad}} = \frac{\tau_{\text{rad}}^{(\text{vac})}}{n_{\text{eff}} \left( \frac{3n_{\text{eff}}^2}{2n_{\text{eff}}^2 + 1} \right)^2} \quad (2.34)$$

when the local-field effects obey the real-cavity model. Expressions (2.33) and (2.34) can be obtained by substituting Eqs. (2.31) and (2.32), respectively, into Eq. (2.30). In the absence of local-field effects, the radiative lifetime can be expressed in terms of the effective refractive index of the suspension by the simple relation

$$\tau_{\text{rad}} = \frac{\tau_{\text{rad}}^{(\text{vac})}}{n_{\text{eff}}}. \quad (2.35)$$

Because we do not know its exact value, we will take the vacuum radiative lifetime  $\tau_{\text{rad}}^{(\text{vac})}$  as an adjustable parameter for fitting our experimental data to different models describing the local-field effects .

Generally, the measured decay time is not purely radiative and can be expressed in terms of the radiative and non-radiative decay times as

$$\frac{1}{\tau_{\text{measured}}} = \frac{1}{\tau_{\text{rad}}} + \frac{1}{\tau_{\text{nonrad}}}. \quad (2.36)$$

It is commonly assumed that the nonradiative decay time  $A_{\text{nonrad}}^{-1}$  does not depend on the refractive index of the surrounding material [16,22] and can be roughly expressed in terms of the radiative lifetime of ions in vacuum using the relation

$$\eta = \frac{A_{\text{rad}}^{(\text{vac})}}{A_{\text{rad}}^{(\text{vac})} + A_{\text{nonrad}}} \quad (2.37)$$

for the quantum yield  $\eta$  of the material. Quantum yield is the fraction of the energy decaying through the radiative channel, so the measured lifetime is purely radiative only in the case when the quantum yield of the material is close to unity.

We were unable to obtain reliable measurements of the absolute quantum yield of our Nd:YAG nanoparticles, in part because of the strong scattering that these particles produce. Instead, we have made use of published values of the quantum yield from bulk samples. Reported values of the quantum yield range from 0.48 (see Ref. [110]) to 0.995 (see Ref. [111]), with 0.6 being the value most often reported [112–114]. It appears that the quantum yield for a given sample depends sensitively on Nd concentration and on environmental issues. For this reason, we have fitted our data to three different models, given by the equations (2.33)–(2.35), using the quantum yield as an additional adjustable parameter.

We first fitted our experimental data to Eq. (2.33), which corresponds to the Lorentz model of local field, and obtained the best least square fit for the quantum yield value  $\eta \approx 0.17 \pm 0.02$ . This value of quantum yield does not fall into the range of the typical measured values of the Nd:YAG quantum yield. This suggests

that the Lorentz (virtual-cavity) model is not likely to describe our experimental outcome properly. Next we used Eq. (2.34) and obtained the best least-square fit of our experimental data for the quantum yield value  $\eta \approx 0.43 \pm 0.07$ . In this case, the value of the quantum yield falls into the range  $0.48 \leq \eta \leq 0.995$  within the error, from which we conclude that the real-cavity model gives a good description to our experimental data. Finally, we made an attempt to fit our experimental data to Eq. (2.35), which corresponds to the assumption that there are no local-field effects. The value of the quantum yield resulting in the best least-square fit is  $\eta \approx 1.13 \pm 0.18$ , which falls into the range of the measured quantum yield values within the error.

The value of the quantum yield giving the best least-square fit of our data with the real-cavity model coincides with the low limit of the measured Nd:YAG quantum yield, whereas such value for the no-local-field-effects model corresponds to the top limit. In order to have an additional argument in favor of one of the two models that give satisfactory descriptions to our experimental data, we present our experimental data together with the results of the least-square fits for the two limiting values of reported quantum yields, namely 1 and 0.48 in Figs. 2.6(a) and 2.6(b), respectively. Through visual inspection of these results, one can immediately rule out the virtual-cavity model. Under the assumption  $\eta = 1$ , both the real-cavity and the no-local-field-effects models agree reasonably well the experimental data, with no-local-field-effects model providing a slightly better fit [see Fig. 2.6(a)]. For the other limiting case, with the assumption that  $\eta = 0.48$  [see Fig. 2.6(b)], the real-cavity model gives the best

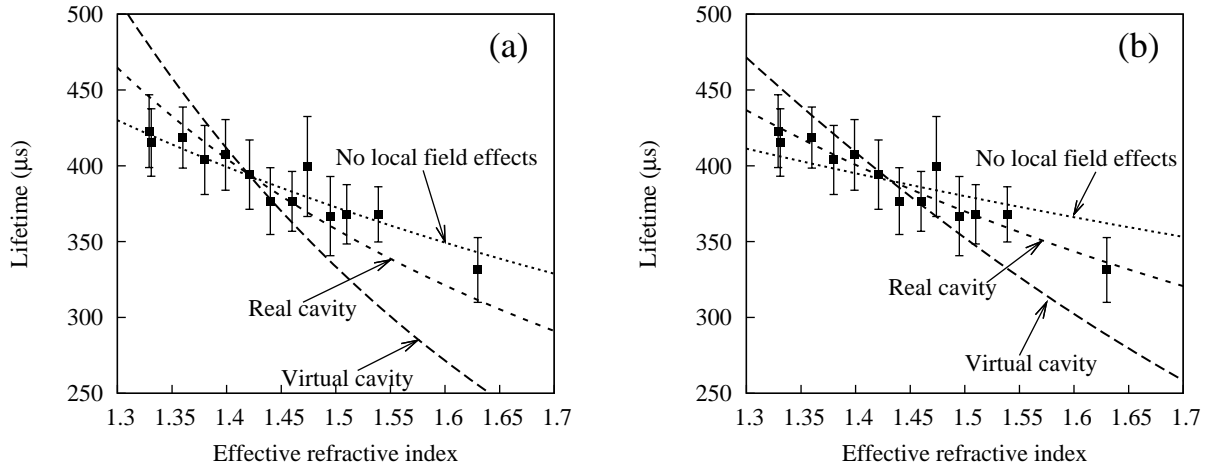


Figure 2.6: Experimentally measured radiative lifetimes of the Nd:YAG-nanopowder suspensions (points with error bars), and the best least-squares fits with various models (lines) under the assumption that the quantum yield of the nanopowder is (a) 1 and (b) 0.48.

fit, which agrees with our expectations based on the theoretical analysis performed in Ref. [12]. The no-local-field-effects model lies pretty close to our experimental data, too. However, there is no theoretical justification for assuming the validity of the no-local-field-effects model, as the physical properties of our samples were such that local field effects should have been present. That is, the sizes of the particles were more than 30 times smaller than the wavelength of light. Also the dispersions were stable in most of the samples, which indicates that even if some particle aggregation had occurred the aggregates were still smaller than the wavelength of light.

The experimental work reported in this section has been published in the Journal of the Optical Society of America B [24].



## 2.4 Optimization of Laser Gain Properties for Layered and Maxwell Garnett Composite Geometries

In Section 2.2 we show that the basic laser properties, such as the radiative lifetime of the upper laser level, small-signal gain coefficient, and saturation intensity can be controlled independently by means of local-field effects [105]. There we made an approximation, treating a composite material of any geometry as a quasi-homogeneous medium characterized by an effective refractive index, with the local-field effects accounted for using the Lorentz model. The Lorentz model of local field has been shown to be applicable to homogeneous media [12]. However, local-field effects can manifest themselves differently in composite materials, and separate theoretical models for describing the laser properties of different composite geometries [10] are needed. In this section, we present such models for layered and Maxwell Garnett composite geometries. One can follow the recipe that we give in the current section to assess the laser properties of more complex composite systems as well.

In Section 1.3.1 we presented an overview of the Lorentz and Onsager models, which are used for describing local-field effects in homogeneous (non-composite) media. In Subsection 2.4.1 of the current section we present the modifications to the Lorentz model for the case in which only a fraction of the atoms or molecules comprising a medium is in resonance with the applied optical field. In Subsection 2.4.2

we consider composite materials of layered geometry under the assumption that one of the constituents contains molecules or atoms that are in resonance with the optical field. We derive the complex susceptibility for such a system, from which one can deduce the absorption and gain coefficients. In the process of the derivation, we obtain a modified local-field-induced frequency shift, similar to the well-known Lorentz red shift [45] in “pure” systems with only one type of molecules or atoms. We perform similar calculations for the Maxwell Garnett composite geometry in Subsection 2.4.3. In Subsection 2.4.4 we analyze the results obtained in the previous subsections, considering two physical systems corresponding to the layered and Maxwell Garnett composite geometries.

### 2.4.1 Lorentz local field in a resonant medium

In present work we consider composite materials consisting of two homogeneous constituents. When studying local-field effects in composite systems one should account for the local field in the constituents, together with the local field modifications imposed by the geometry of the composite. Within this study, we limit ourselves to the case in which the homogeneous constituents obey the Lorentz model of the local field. One can easily extend our formalism to the case of Onsager-type constituents.

We first consider a homogeneous medium with pure resonant molecules or atoms (we call them emitters) illuminated by an optical field of frequency  $\omega$ . We assume that the field is tuned close to a resonance of the emitters. In that case we can

treat the medium roughly as a collection of two-level atoms, and can apply a well-known formalism, based on the Maxwell–Bloch equations [41], to describe the optical properties of such a medium. This formalism is described in Section 1.4. We insert the Lorentz local field (2.1) into the Maxwell–Bloch Equations (1.19) for the slowly varying amplitude  $\sigma^{(1)}$  of the coherence  $\tilde{\sigma}^{(1)}(t) = \sigma^{(1)} \exp(-i\omega t) + \text{c.c.}$  and population inversion  $w$  to obtain:

$$\dot{\sigma}^{(1)} = \left( i\Delta + i\Delta_{\text{L}}w - \frac{1}{T_2} \right) \sigma^{(1)} - \frac{1}{2}i\kappa w E, \quad (2.38a)$$

$$\dot{w} = -\frac{w - w_{\text{eq}}}{T_1} + i(\kappa E(\sigma^{(1)})^* - \kappa^* E^* \sigma^{(1)}). \quad (2.38b)$$

Here  $\Delta = \omega - \omega_0$  is the detuning of the optical frequency  $\omega$  from the atomic resonance frequency  $\omega_0$ ,  $T_1$  and  $T_2$  are the population and coherence relaxation times, respectively,  $w_{\text{eq}}$  is the equilibrium value of the population inversion, and  $\kappa = 2\mu/\hbar$ , where  $\mu$  is the dipole moment of the atomic transition. Here and below, we use a tilde to denote the time-dependent quantities, and similar variables without a tilde to denote their slowly-varying amplitudes. Within this study we are only concerned with the linear optical response of the laser gain media. In order to emphasize it, we added the superscript “(1)” to the coherence  $\sigma^{(1)}$ . The inversion-dependent frequency shift  $\Delta_{\text{L}}w$  involves a shift of the resonance of the atomic transition. Here  $\Delta_{\text{L}}$  is known as

Lorentz red shift [45] and is given by

$$\Delta_L = -\frac{4\pi}{3} \frac{N|\mu|^2}{\hbar}. \quad (2.39)$$

The slowly-varying amplitude  $P$  of the macroscopic polarization can be expressed in terms of the linear susceptibility  $\chi^{(1)}$  as  $P = \chi^{(1)}E$ . We find from Eq. (1.20) that

$$\chi^{(1)} = \frac{N\mu^*\sigma^{(1)}}{E}. \quad (2.40)$$

Substituting the steady-state solution of Eq. (2.38a) for the coherence  $\sigma^{(1)}$ , given by Eq. (1.24b) in Section 1.4, yields

$$\chi^{(1)} = \frac{N|\mu|^2}{\hbar} \frac{w_{\text{eq}}}{\Delta + \Delta_L w_{\text{eq}} + i/T_2}. \quad (2.41)$$

Here  $w_{\text{eq}}$  is the equilibrium value of the population inversion (*e.g.*, in the case of an uninverted system,  $w_{\text{eq}} = -1$ ). Now we can find small-signal gain ( $g_0$ ) and absorption ( $\alpha_0$ ) coefficients of the medium from Eq. (2.17):

$$g_0 = -\alpha_0 = -\frac{4\pi\omega}{c\sqrt{\epsilon}} \text{Im} \chi^{(1)}. \quad (2.42)$$

The dielectric permittivity  $\epsilon$  entering Eq. (2.42) describes the dielectric properties of the entire material structure away from its resonances.

The above analysis is valid for the case of “pure resonant emitters” (PRE) in

which all emitters are of the same sort. However, when dealing with laser gain media, it is more typical to have a system with atoms or molecules of two or more sorts. Therefore, it is useful to modify the above two-level model to consider the case in which one has a background (host) material with the transition frequencies far from that of the optical field, doped with some portion of atoms with a transition frequency in resonance with the optical field. We refer to this case as “resonant emitters in a background” (REB). For this kind of medium, we can split the total polarization entering Eq. (2.1) for the Lorentz local field (we call it  $P_{\text{tot}}$  from now on) into a contribution coming from the atoms of the background medium and a contribution from the resonant atoms:

$$P_{\text{tot}} = N_{\text{bg}} \alpha_{\text{bg}} E_{\text{loc}} + N_{\text{res}} \mu_{\text{res}}^* \sigma_{\text{res}}^{(1)}, \quad (2.43)$$

where  $\alpha_{\text{bg}}$  is the polarizability of a background atom. Here and below the parameters with the subscripts “bg” and “res” refer to the background and resonant atoms or molecules of the medium. As we consider only media in which the Lorentz model of local field is valid, both resonant and background types of molecules or atoms should experience the same Lorentz local field.

One can relate the polarizability  $\alpha_{\text{bg}}$  to the dielectric constant of the background material  $\epsilon_{\text{bg}}$  using the Clausius–Mossotti (or Lorentz–Lorenz) relation [6, 37, 40]

$$\frac{\epsilon_{\text{bg}} - 1}{\epsilon_{\text{bg}} + 2} = \frac{4\pi}{3} N_{\text{bg}} \alpha_{\text{bg}}, \quad (2.44)$$

also obtained in Section (1.3.1) (see Eq. (1.12)). Substituting Eq. (3.17) into Eq. (2.1) for the local field and using Clausius–Mossotti relation (2.44) and Eq. (2.2) for the local-field correction factor, we find

$$E_{\text{loc}} = L_{\text{bg}} \left( E + \frac{4\pi}{3} P_{\text{res}} \right). \quad (2.45)$$

The current expression for the local field reduces to Eq. (2.1) if one considers a vacuum to be a background medium.

Next, we find the susceptibility of the medium from the relationship  $\chi^{(1)} = P_{\text{tot}}/E$ . Substituting Eq. (3.17) and the steady-state solution (1.24b) for  $\sigma_{\text{res}}^{(1)}$  into the above relationship for  $\chi^{(1)}$ , we arrive at the result

$$\chi^{(1)} = \chi_{\text{bg}}^{(1)} + \frac{N_{\text{res}} |\mu_{\text{res}}|^2}{\hbar} \frac{L_{\text{bg}}^2 w_{\text{eq, res}}}{\Delta + \Delta'_{\text{L}} w_{\text{eq, res}} + i/T_{2, \text{res}}} \quad (2.46)$$

for the linear susceptibility of the REB medium. The frequency shift  $\Delta'_{\text{L}}$  is a modified Lorentz red shift, given by

$$\Delta'_{\text{L}} = -\frac{4\pi}{3} \frac{N_{\text{res}} |\mu_{\text{res}}|^2}{\hbar} L_{\text{bg}} = L_{\text{bg}} \Delta_{\text{L}}. \quad (2.47)$$

This enhancement of the Lorentz red shift by  $L_{\text{bg}}$  due to the influence of the background dielectric medium had been previously noted in [115].

### 2.4.2 Linear Susceptibility of Layered Composite Materials

Layered composite materials [10, 27] are periodic structures consisting of alternating layers of two or more homogeneous materials with different optical properties. We presented an overview of layered composite materials in Section 1.2.1. Here we consider a layered composite material comprised of two types of homogeneous media (we call them  $a$  and  $b$ ) with different optical properties (see Fig. 1.1(c)).

Let us assume that both components  $a$  and  $b$  of our layered composite material respond linearly to the applied optical field. Assume that the field of frequency  $\omega$  is tuned close to one of the resonances of the component  $a$ , but does not coincide with any of the resonances of the component  $b$ . We further follow the recipe given in [27] for deriving the local field in a layer  $a$ .

We choose an axis  $Z$  to be perpendicular to the layers and focus on describing the  $Z$ -component of the electric field and polarization. We define  $E$  and  $P$  to be the average macroscopic field and polarization in the composite material, respectively,  $e_a$  and  $e_b$  to denote mesoscopic fields in layers  $a$  and  $b$ , respectively,  $E_{a,\text{loc}}$  as a local field in layer  $a$ , and  $p_a$  and  $p_b$  as mesoscopic polarizations in layers  $a$  and  $b$ , respectively. For simplicity of notation, we do not write the indices  $z$ , indicating  $Z$ -components, next to the fields and polarizations. Following the results obtained in [27] we can write

$$e_j = E + 4\pi P - 4\pi p_j, \quad (2.48)$$

where  $j = a, b$  for the mesoscopic fields in layers  $a$  and  $b$ . The macroscopic polarization

is related to the mesoscopic polarizations in layers  $a$  and  $b$  as

$$P = f_a p_a + f_b p_b \quad (2.49)$$

with the volume fractions obeying the relationship  $f_a + f_b = 1$ . As the applied optical field's frequency does not coincide with any of the resonances of the medium  $b$ , we can simply write

$$p_b = \chi_b^{(1)} e_b \quad (2.50)$$

for the mesoscopic field and polarization in a layer  $b$ , with  $\chi_b^{(1)}$  denoting the linear susceptibility in the layer. Using Eq. (2.50) and the relationship  $\epsilon_b = 1 + 4\pi\chi_b^{(1)}$  for the dielectric constant and susceptibility in layer  $b$ , we obtain from Eq. (2.48) the expressions for the mesoscopic fields in terms of the average field  $E$  and the mesoscopic polarization  $p_a$  in the form

$$e_a = \frac{\epsilon_b}{1 + 4\pi f_a \chi_b^{(1)}} E - \frac{4\pi f_b}{1 + 4\pi f_a \chi_b^{(1)}} p_a \quad (2.51a)$$

and

$$e_b = \frac{1}{1 + 4\pi f_a \chi_b^{(1)}} E + \frac{4\pi f_a}{1 + 4\pi f_a \chi_b^{(1)}} p_a. \quad (2.51b)$$

Next we want to express the local field  $E_{a,\text{loc}}$  in a layer  $a$  in terms of the average field  $E$  and the mesoscopic polarization  $p_a$ . Here we distinguish two cases: the case of PRE, in which all the atoms or molecules of the material  $a$  are of the same sort, and



the case of REB, in which only a part of the atoms or molecules of the homogeneous medium  $a$  are in resonance with the optical field.

### Case of pure resonant emitters

We first treat the simpler case of PRE in the constituent  $a$ . In this case, the local field in the medium  $a$  takes the form

$$E_{a,\text{loc}} = e_a + \frac{4\pi}{3} p_a. \quad (2.52)$$

Substituting Eq. (2.51a) into Eq. (2.52), we find the expression for the local field in terms of the average field and the mesoscopic polarization in a layer  $a$ ,

$$E_{a,\text{loc}} = \frac{\epsilon_b}{1 + 4\pi f_a \chi_b^{(1)}} E + \frac{4\pi}{3} \frac{f_a \epsilon_b - 2f_b}{1 + 4\pi f_a \chi_b^{(1)}} p_a. \quad (2.53)$$

The effective susceptibility of the layered composite material can be found from  $\chi_{\text{eff}}^{(1)} = P/E$ . Substituting  $p_b$  in the form of Eq. (2.50) and  $p_a$  in the form of Eq. (1.20) into Eq. (2.49) for the macroscopic polarization and using Eq. (2.51b) for  $e_b$  and the steady-state solution (1.24b) for the coherence  $\sigma_a^{(1)}$ , we finally obtain the expression for the effective susceptibility of a layered composite material with PRE in the constituent  $a$ :

$$\chi_{\text{eff}}^{(1)} = \frac{f_a \epsilon_b^2}{(1 + 4\pi f_a \chi_b^{(1)})^2} \frac{N_a |\mu_a|^2}{\hbar} \frac{w_{\text{eq},a}}{\Delta + \Delta_1 w_{\text{eq},a} + i/T_{2,a}} + \frac{f_b \chi_b^{(1)}}{1 + 4\pi f_a \chi_b^{(1)}}. \quad (2.54)$$

The local-field-induced frequency shift  $\Delta_1$  of the resonance feature has the form

$$\Delta_1 = -\frac{4\pi}{3} \frac{|\mu_a|^2 N_a}{\hbar} \frac{f_a \epsilon_b - 2f_b}{1 + 4\pi f_a \chi_b^{(1)}}. \quad (2.55)$$

The subscript “ $a$ ” next to the atomic parameters indicates that they refer to the resonant constituent  $a$ . One can easily verify that in the limiting case of  $f_a \rightarrow 1$  and  $f_b \rightarrow 0$  Eq. (2.54) reduces to Eq. (2.41) for the susceptibility of a pure homogeneous medium, and Eq. (2.55) takes the form of Eq. (2.39) for the Lorentz red shift. In the opposite limiting case of  $f_a \rightarrow 0$  and  $f_b \rightarrow 1$ , the effective susceptibility reduces to  $\chi_b^{(1)}$ .

### Case of resonant emitters in a background

Now we consider the case of REB in layers  $a$ . In that case, the local field  $E_{a,\text{loc}}$  in the layer  $a$  can be expressed as

$$E_{a,\text{loc}} = e_a + \frac{4\pi}{3} (p_{a,\text{bg}} + p_{a,\text{res}}). \quad (2.56)$$

The background and resonant contributions to the total mesoscopic polarization of the material  $a$  are given by

$$p_{a,\text{bg}} = N_{a,\text{bg}} \alpha_{a,\text{bg}} E_{a,\text{loc}} \quad (2.57a)$$

and

$$p_{a,\text{res}} = N_{a,\text{res}} \mu_{a,\text{res}}^* \sigma_{a,\text{res}}^{(1)}. \quad (2.57b)$$

Substituting Eqs. (2.57a) and (2.51a) into Eq. (2.56) yields the expression for the local field in terms of the average field and the resonant contribution to the mesoscopic polarization,

$$E_{a,\text{loc}} = \frac{L_{a,\text{bg}} \epsilon_b}{1 + 4\pi(f_a \chi_b^{(1)} + f_b \chi_{a,\text{bg}}^{(1)})} E + \frac{4\pi L_{a,\text{bg}}(1 + 4\pi f_a \chi_b^{(1)} - 3f_b)}{3(1 + 4\pi(f_a \chi_b^{(1)} + f_b \chi_{a,\text{bg}}^{(1)}))} p_{a,\text{res}}. \quad (2.58)$$

We find the effective susceptibility from  $\chi_{\text{eff}}^{(1)} = P/E$ , using Eqs. (2.49), (2.50), (2.51b), (2.57), (2.58), and the steady-state solution (1.24b) for coherence  $\sigma_{a,\text{res}}^{(1)}$ :

$$\begin{aligned} \chi_{\text{eff}}^{(1)} &= f_a \frac{\epsilon_b}{1 + 4\pi f_a \chi_b^{(1)}} \frac{\epsilon_b}{1 + 4\pi(f_a \chi_b^{(1)} + f_b \chi_{a,\text{bg}}^{(1)})} \\ &\times \left[ \chi_{a,\text{bg}}^{(1)} + L_{a,\text{bg}} \left( \frac{4\pi \chi_{a,\text{bg}}^{(1)}(1 + 4\pi f_a \chi_b^{(1)} - 3f_b)}{3(1 + 4\pi(f_a \chi_b^{(1)} + f_b \chi_{a,\text{bg}}^{(1)}))} + 1 \right) \right. \\ &\times \left. \frac{N_{a,\text{res}} |\mu_{a,\text{res}}|^2}{\hbar} \frac{w_{\text{eq, res}}}{\Delta + \Delta'_1 w_{\text{eq, res}} + i/T_{2,\text{res}}} \right] + \frac{f_b \chi_b^{(1)}}{1 + 4\pi f_a \chi_b^{(1)}}. \end{aligned} \quad (2.59)$$

The frequency shift  $\Delta'_1$  of the resonant feature is given by

$$\Delta'_1 = -\frac{4\pi |\mu_{a,\text{res}}|^2 N_{a,\text{res}} L_{a,\text{bg}} (1 + 4\pi f_a \chi_b^{(1)} - 3f_b)}{3 \hbar (1 + 4\pi(f_a \chi_b^{(1)} + f_b \chi_{a,\text{bg}}^{(1)}))}. \quad (2.60)$$

In the limit  $f_a \rightarrow 1$  and  $f_b \rightarrow 0$  Eq. (2.59) reduces to Eq. (2.46), and the frequency shift (2.60) reduces to the modified Lorentz red shift (2.47). In the opposite limiting

case of  $f_a \rightarrow 0$  and  $f_b \rightarrow 1$  we obtain  $\chi_{\text{eff}}^{(1)} = \chi_b^{(1)}$ .

### 2.4.3 Linear Susceptibility of Maxwell Garnett Composite Materials

The Maxwell Garnett type of composite geometry is a collection of small particles (the inclusions) distributed in a host medium (see Section 1.2.1, Fig. 1.1(a)). The effective dielectric constant of a Maxwell Garnett composite material is described by Eq. (1.1).

Here we derive the local-field-corrected total susceptibility function for a Maxwell Garnett composite material with homogeneous host and inclusion materials. Because of the geometry of Maxwell Garnett composite materials, the local field is uniform in the inclusion medium and non-uniform in the host [25]. We limit ourselves to treating the case of resonant species in inclusions, as treating a more complicated case of resonance in a host is beyond the scope of the present work. Following our recipe, one can numerically solve the problem to deduce the total susceptibility and associated frequency shift of the resonant feature for the latter case.

Assuming that both the host and inclusion materials respond linearly to the applied optical field and following the prescriptions given in the Ref. [25], we derive Eq. (A.8) for the mesoscopic electric field  $\mathbf{e}_i$  in an inclusion in the Appendix A. Here we drop the vector notation, as the inclusion medium is assumed to be isotropic and

uniform:

$$e_i = \frac{3\epsilon_h}{3\epsilon_h - 4\pi f_h \chi_h^{(1)}} \left[ E - \frac{4\pi}{3\epsilon_h} f_h p_i \right]. \quad (2.61)$$

In the above equation  $\chi_h^{(1)}$  and  $f_h$  are the linear susceptibility and volume fraction of the host, respectively, and  $p_i$  is the mesoscopic polarization in an inclusion. As in the previous subsection, we consider the cases of PRE and REB in inclusions.

### Case of pure resonant emitters

We obtain the expression for the local field  $E_{i,\text{loc}}$  acting on the emitters in an inclusion from Eq. (2.1):

$$E_{i,\text{loc}} = e_i + \frac{4\pi}{3} p_i. \quad (2.62)$$

Substituting Eq. (2.61) yields

$$E_{i,\text{loc}} = \frac{3\epsilon_h}{3\epsilon_h - 4\pi f_h \chi_h^{(1)}} E + \frac{4\pi}{3} \frac{\epsilon_h(2 + f_i) - 2f_h}{3\epsilon_h - 4\pi f_h \chi_h^{(1)}} p_i. \quad (2.63)$$

Substituting the local field (2.63) into the Maxwell–Bloch equations (1.19), we find their steady-state solutions.

The macroscopic polarization  $P$  is an average of the mesoscopic polarization  $p(r)$ :

$$P = \int \tilde{\Delta}(r - r') p(r') dr'. \quad (2.64)$$

The weighting function  $\tilde{\Delta}(r)$  is defined in Ref. [25] and in the Appendix A. Introduc-

ing the functions

$$p(r) = \begin{cases} p_i(r) & \text{if } r \in \text{inclusion,} \\ p_h(r) & \text{if } r \in \text{host} \end{cases} \quad (2.65)$$

We can represent the macroscopic polarization as an average of the mesoscopic polarizations  $p_i$  and  $p_h$  in the inclusions and host:

$$P = \int \tilde{\Delta}(r - r') p_i(r') dr' + \int \tilde{\Delta}(r - r') p_h(r') dr'. \quad (2.66)$$

We can represent the macroscopic electric field  $E$  as an average of the mesoscopic electric fields in the inclusion and host in a similar way. Since the mesoscopic polarization and electric field in an inclusion are uniform, the first terms on the right-hand side of Eq. (2.66) is equal to  $f_i p_i$ . Similarly, one can obtain  $f_i e_i$  for the electric field. Using this result, we find the expression for the macroscopic polarization:

$$P = f_i p_i(r) + \chi_h^{(1)} E - f_i \chi_h^{(1)} e_i(r). \quad (2.67)$$

Substituting Eq. (2.61) for  $e_i$ , Eq. (1.20) for the resonant  $p_i$ , and the steady-state solution for  $\sigma_i^{(1)}$  to Eq. (2.67) for the macroscopic polarization, and using the relationship  $\chi_{\text{eff}}^{(1)} = P/E$ , we finally obtain the expression for the effective susceptibility

of a Maxwell Garnett composite material with a resonance in the inclusions:

$$\begin{aligned} \chi_{\text{eff}}^{(1)} &= f_i \left( \frac{3\epsilon_h}{3\epsilon_h - 4\pi f_h \chi_h^{(1)}} \right)^2 \frac{N_i |\mu_i|^2}{\hbar} \frac{w_{\text{eq},i}}{\Delta + \Delta_{\text{MG}} w_{\text{eq},i} + i/T_2} \\ &\quad + f_h \frac{\chi_h^{(1)}(2\epsilon_h + 1)}{3\epsilon_h - 4\pi f_h \chi_h^{(1)}}. \end{aligned} \quad (2.68)$$

The Maxwell Garnett frequency shift  $\Delta_{\text{MG}}$  of the resonance feature has the form

$$\Delta_{\text{MG}} = -\frac{4\pi}{3} \frac{N_i |\mu_i|^2}{\hbar} \frac{\epsilon_h(2 + f_i) - 2f_h}{3\epsilon_h - 4\pi f_h \chi_h^{(1)}}. \quad (2.69)$$

The subscript “i” next to the atomic parameters indicates that they refer to the inclusion material. It is easy to verify that Eq. (2.68) reduces to Eq. (2.41), and the frequency shift (2.69) reduces to the Lorentz red shift (2.39) in the limit  $f_i \rightarrow 1$  and  $f_h \rightarrow 0$ . We obtain  $\chi_{\text{eff}}^{(1)} = \chi_h^{(1)}$  in the opposite limiting case.

### Case of resonant emitters in a background

Here we consider the case of REB in inclusions. The local field  $E_{i,\text{loc}}$  acting on an emitter in an inclusion is given by Eq. (2.63) in terms of the macroscopic field  $E$  and the mesoscopic polarization  $p_i$  in an inclusion, but we need to express it in terms of the field  $E$  and the resonant part  $p_{i,\text{res}}$  of the polarization  $p_i$ , which is now

$$p_i = p_{i,\text{bg}} + p_{i,\text{res}}. \quad (2.70)$$

The background non-resonant and resonant contributions to the mesoscopic polarization of an inclusion are given by

$$p_{i, \text{bg}} = N_{i, \text{bg}} \alpha_{i, \text{bg}} E_{i, \text{loc}} \quad (2.71\text{a})$$

and

$$p_{i, \text{res}} = N_{i, \text{res}} \mu_{i, \text{res}}^* \sigma_{i, \text{res}}^{(1)} \quad (2.71\text{b})$$

Substituting Eqs. (2.70) and (2.71) into Eq. (2.63) yields the expression

$$E_{i, \text{loc}} = \frac{3\epsilon_{\text{h}} L_{i, \text{bg}}}{3\epsilon_{\text{h}} + 4\pi f_{\text{h}} (\chi_{i, \text{bg}}^{(1)} - \chi_{\text{h}}^{(1)})} E + \frac{4\pi}{3} L_{i, \text{bg}} \frac{\epsilon_{\text{h}} (2 + f_{\text{i}}) - 2f_{\text{h}}}{3\epsilon_{\text{h}} + 4\pi f_{\text{h}} (\chi_{i, \text{bg}}^{(1)} - \chi_{\text{h}}^{(1)})} p_{i, \text{res}} \quad (2.72)$$

for the local field in terms of the macroscopic field and resonant contribution to the mesoscopic polarization. Substituting the local field in the form of Eq. (2.72) into the Maxwell–Bloch equations (1.19), we find the steady-state solution for coherence  $\sigma_{i, \text{res}}^{(1)}$ .

One can find the effective susceptibility from  $\chi_{\text{eff}}^{(1)} = P/E$  by substituting  $P$  from Eq. (2.67) with  $e_i$  given by Eq. (2.61) and  $p_i$  given by Eqs. (2.70) and (2.71), and the



steady-state solution for  $\sigma_{i,\text{res}}^{(1)}$ :

$$\begin{aligned} \chi_{\text{eff}}^{(1)} = & f_i \frac{3\epsilon_h}{3\epsilon_h - 4\pi f_h \chi_h^{(1)}} \frac{3\epsilon_h}{3\epsilon_h + 4\pi f_h (\chi_{i,\text{bg}}^{(1)} - \chi_h^{(1)})} \\ & \times \left[ \chi_{i,\text{bg}}^{(1)} + L_{i,\text{bg}} \left( \frac{4\pi}{3} \frac{\chi_{i,\text{bg}}^{(1)} [\epsilon_h (2 + f_i) - 2f_h]}{3\epsilon_h + 4\pi f_h (\chi_{i,\text{bg}}^{(1)} - \chi_h^{(1)})} + 1 \right) \right. \\ & \left. \times \frac{N_{i,\text{res}} |\mu_{i,\text{res}}|^2}{\hbar} \frac{w_{\text{eq, res}}}{\Delta + \Delta'_{\text{MG}} w_{\text{eq, res}} + i/T_{2,\text{res}}} \right] + f_h \chi_h^{(1)} \frac{2\epsilon_h + 1}{3\epsilon_h - 4\pi f_h \chi_h^{(1)}}. \end{aligned} \quad (2.73)$$

The frequency shift  $\Delta'_{\text{MG}}$  is given by

$$\Delta'_{\text{MG}} = -\frac{4\pi}{3} \frac{N_{i,\text{res}} |\mu_{i,\text{res}}|^2}{\hbar} \frac{L_{i,\text{bg}} [\epsilon_h (2 + f_i) - 2f_h]}{3\epsilon_h + 4\pi f_h (\chi_{i,\text{bg}}^{(1)} - \chi_h^{(1)})}. \quad (2.74)$$

In the limit  $f_i \rightarrow 1$  and  $f_h \rightarrow 0$  Eq. (2.73) reduces to Eq. (2.46), and the frequency shift (2.74) reduces to the modified Lorentz red shift (2.47). In the opposite limit,

$$\chi_{\text{eff}}^{(1)} = \chi_b^{(1)}.$$

#### 2.4.4 Analysis

In this subsection we analyze the results for the effective linear susceptibility obtained in the previous subsections for the layered and Maxwell Garnett composite materials.

##### Layered Geometry

The local-field-corrected effective linear susceptibility for a layered composite material with the resonance in the layers  $a$  is given by Eq. (2.54) for the case in which all the

atoms or molecules of  $a$  are of the same sort (PRE case), and by Eq. (2.59) for the case in which the component  $a$  consists of particles of different sorts (REB case). One can find the small-signal gain coefficient of the layered composite material by substituting an expression for the effective susceptibility into Eq. (2.42).

Here we analyze the behavior of the small-signal gain as a function of various parameters, choosing a Rhodamine 6G-doped PMMA laser gain medium as the resonant species  $a$  in our layered composite material. The parameters of the gain medium that we used for our analysis are the emission peak wavelength  $\lambda_0 = 590$  nm, the transverse relaxation time  $T_2 = 100$  fs, the transition cross section  $\sigma_{\text{tr}} = 2 \times 10^{-16}$  cm<sup>2</sup>, the Rhodamine molecular concentration  $N = 1.8 \times 10^{18}$  cm<sup>-3</sup>, and the refractive index of PMMA,  $n_{\text{bg}} = 1.4953$ . We take the component  $b$  to be an unknown material and vary its refractive index to see how it affects the optical response of Rhodamine-doped PMMA.

Rhodamine-doped PMMA is an example of the REB case, and, therefore, one should use Eq. (2.59) in order to describe the effective susceptibility of the system with Rhodamine-doped PMMA resonant layers. We compare the model given by Eq. (2.59) to the case of PRE, described by Eq. (2.54), in order to test whether one can use the latter approximation in case of REB. Using the PRE model in this physical case implies that we neglect the presence of PMMA, assuming that the Rhodamine molecules are sitting in a vacuum.

We also find it informative to compare the results given by the more precise REB

model (2.59) to that of the simplified model that we proposed in Section 2.2 (see Eq. (2.28b)). The approximation underlying the simplified model is that a composite laser gain medium is represented as a quasi-homogeneous medium characterized by an effective refractive index, and the local-field effects are accounted for by the Lorentz model for homogeneous media. For the purpose of comparison, we adapt this simplified model to our REB case in the following way. We take the expression (2.46) for the linear susceptibility of a medium with REB, substituting  $\chi_{\text{eff}}^{(1)}$ , deduced from Eq. (1.4) for  $\epsilon_{\text{eff}}$  of a layered composite material, in place of  $\chi_{\text{bg}}^{(1)}$ , and  $L_{\text{eff}} = (\epsilon_{\text{eff}} + 2)/3$  in place of  $L_{\text{bg}}$ . We also multiply the atomic densities appearing in the expression by the volume fraction  $f_a$  to take into account the fact that, changing the volume fraction of the resonant component, we change the density of the resonant molecules. Then we substitute the resulting expression for  $\chi^{(1)}$  to Eq. (2.28b) to find the small-signal gain coefficient, corresponding to the simplified model.

Setting the equilibrium value of the population inversion  $w_{\text{eq}} = 1$ , which corresponds to a fully inverted amplifying system, and the detuning of the optical field with respect to the resonance  $\Delta = 0$ , we plot the small-signal gain calculated using the effective susceptibility given by Eq. (2.59) as a function of the refractive index of the non-resonant component  $n_b$  in Fig. 2.7(a), and of  $f_a$  in Fig. 2.8. In addition, we plot the gain coefficients derived from Eq. (2.54) and from the simplified model from Section 2.2 as functions of  $n_b$  in Figs. 2.7(b) and 2.7(c), respectively. The comparison between parts (a) and (b) of Fig. 2.7 indicates that the results for the cases of

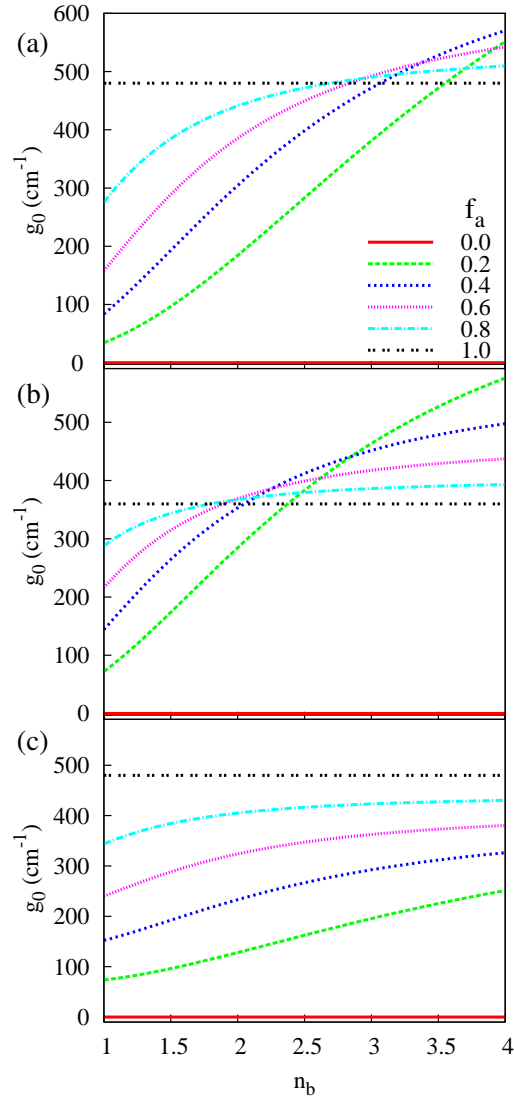


Figure 2.7: Small-signal gain of a layered composite material as a function of the refractive index of the non-resonant component for different values of the volume fraction of the resonant component: (a) REB case [derived from Eq. (2.59)], (b) PRE case [from Eq. (2.54)], (c) the simplified model.

PRE and REB differ significantly, which means that the approximation based on the assumption that all the atoms or molecules of the resonant species are of the same sort does not work in the REB case. The comparison of Figs. 2.7(a) and 2.7(c)

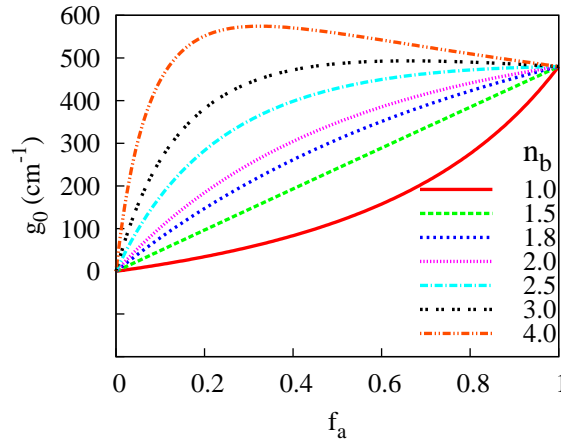


Figure 2.8: Small-signal gain of a layered composite material as a function of the volume fraction of the resonant component for different values of the refractive index of the non-resonant component. The gain is derived from Eq. (2.59) for the REB case.

shows moreover that the simplified model is insufficiently precise. Therefore, as we stated earlier in Section 2.2, it is only good enough for a proof-of-principle study, and separate, more precise models for each composite geometry are required for an accurate description of the optical response.

It can be seen from Figs. 2.7 and 2.8 that the gain coefficient tends to grow with the increase of the refractive index of the non-resonant component. The reason for this behavior is that for the light polarized perpendicular to the layers, the electric field tends to localize in the regions of a dielectric with lower refractive index [27]. Therefore, the higher refractive index of the non-resonant layers is, the more the electric field is displaced into the resonant layers, which causes a stronger gain. The behavior of the gain coefficient as a function of  $f_a$  is more complex. It grows monotonously with the increase of  $f_a$  for small refractive indices. In the case  $n_b = n_{bg}$  the growth is

linear. For high values of the refractive index the small-signal gain displays a rapid growth with the increase of the volume fraction until it reaches a maximum value, corresponding to an optimal value of  $f_a$ , after which it starts to decrease with further increase of  $f_a$ . This behavior can be understood as follows. The initial growth of  $g_0$  with  $f_a$  is due to the fact that the number of the resonant molecules in the medium increases. On the other hand, increasing  $f_a$ , we make our layers with the resonant molecules thicker, and the local field, highly concentrated in these layers because of the high value of  $n_b$ , spreads over the layers, and each individual molecule “feels” a smaller value of the local field. This causes the gain to decrease with the increase of  $f_a$  beyond an optimal value. Thus, in order to achieve maximum gain or absorption in a layered composite material, one needs to use a non-resonant component with a high refractive index, while keeping the volume fraction of the resonant component low.

Setting  $f_a = 0.5$  and  $n_b = 1.8$ , we plot in Fig. 2.9 the small-signal gain for REB in the component  $a$  as a function of the frequency detuning  $\Delta$  of the optical field with respect to the molecular resonance for different values of  $w_{\text{eq}}$ . Variation of the population inversion from  $w_{\text{eq}} = -1$ , corresponding to an uninverted system, to  $w_{\text{eq}} = 1$ , describing a fully inverted system, clearly shows how the composite medium changes from an absorber to an amplifier. In reality, it is not possible to achieve a full inversion, so, most physical cases correspond to  $w_{\text{eq}} < 0.5$ .

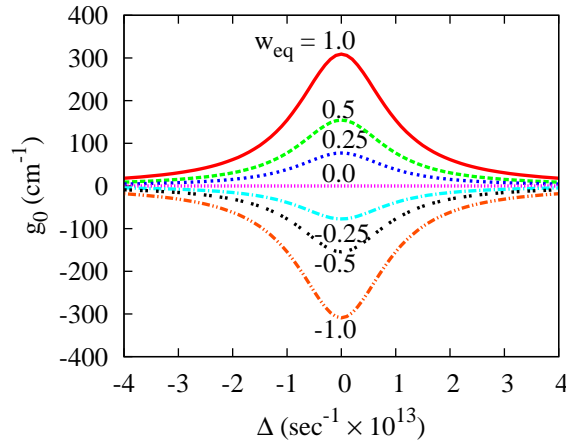


Figure 2.9: Small-signal gain of a layered composite material as a function of the detuning of the optical field with respect to the molecular resonant frequency. Marked on the graphs are the values of equilibrium population inversion.

### Maxwell Garnett Geometry

The linear effective susceptibility for the Maxwell Garnett composite geometry for the case of PRE and REB in inclusions is given by Eqs. (2.68) and (2.73), respectively. Substituting these expressions into Eq. (2.17), we obtain the small-signal gain coefficients for the cases of PRE and REB.

We take for our analysis a Maxwell Garnett composite material with Nd:YAG nanoparticles as inclusions. We use the emission wavelength  $\lambda_0 = 1.064 \mu\text{m}$ , the transverse relaxation time  $T_2 = 3 \text{ ms}$ , the transition cross section  $\sigma_{\text{tr}} = 4.6 \times 10^{-19} \text{ cm}^2$ , the neodymium atomic concentration  $N = 1.37 \times 10^{20} \text{ cm}^{-3}$  (this value corresponds to 1 at. % of Nd in YAG), and the YAG refractive index  $n_{\text{bg}} = 1.82$ . We take the host to be an unknown medium, and vary its refractive index  $n_{\text{h}}$  to see how it affects the optical response of Nd:YAG nanoparticles.

Nd:YAG corresponds to the case of REB, which means that the effective susceptibility of the Maxwell Garnett composite material with Nd:YAG inclusions obeys Eq. (2.73). As in the previous section, we compare the small-signal gain coefficients, corresponding to the REB model, given by Eq. (2.73), to the PRE model, given by Eq.(2.68), and to the simplified model from Section 2.2, adapted to our case, in order to test the applicability of the latter two approximations. The simplified model is derived from Eq. (2.46) with  $\chi_{\text{eff}}^{(1)}$  and  $L_{\text{eff}}$ , deduced from Eq. (1.1) for  $\epsilon_{\text{eff}}$  of the Maxwell Garnett composite material, in place of  $\chi_{\text{bg}}^{(1)}$  and  $L_{\text{bg}}$ . In addition, we multiply the atomic density in the resulting equation by the inclusion volume fraction  $f_i$  in order to account for its change with the change of  $f_i$ . Then we substitute the resulting expression for  $\chi^{(1)}$  into Eq. (2.17) to deduce the gain coefficient.

Setting the equilibrium value of the population inversion  $w_{\text{eq}} = 1$  and the detuning  $\Delta = 0$ , we plot the small-signal gain coefficients derived from the REB [Eq. (2.73)] and PRE [Eq. (2.68)] models, and from the simplified model, as functions of the refractive index of the host  $n_h$  in Figs. 2.10(a), 2.10(b), and 2.10(c), respectively. The dependence of  $g_0$ , derived from Eq. (2.73), on the inclusion volume fraction  $f_i$  is depicted in Fig. 2.11. A comparison of the part a with the parts b and c of Fig. 2.10 suggests that, as in the case of the layered composite geometry, the PRE approximation and simplified model do not agree with the more precise description of the Maxwell Garnett composite material with REB in inclusions.

One can see from Figs. 2.10 and 2.11 that the small-signal gain of the Maxwell



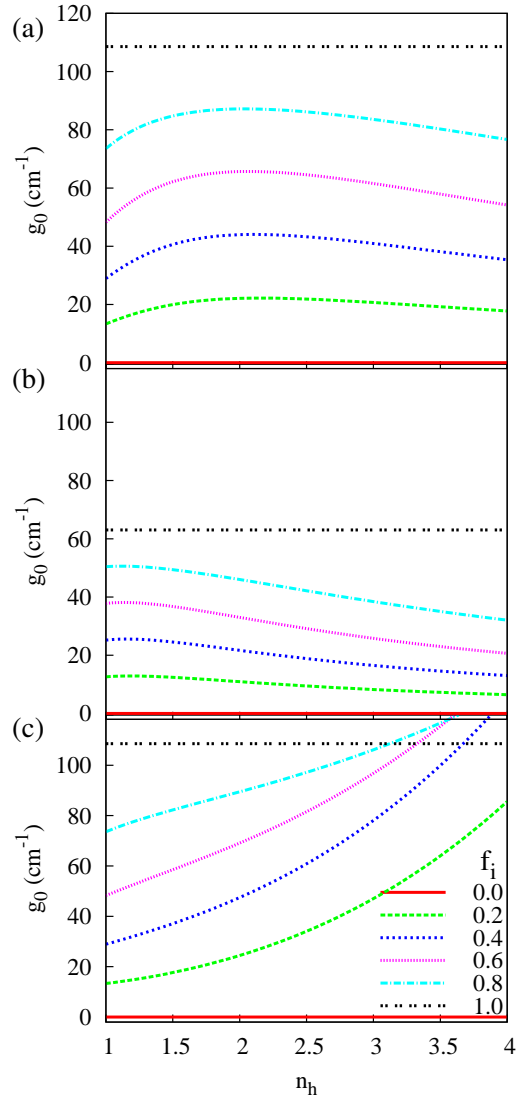


Figure 2.10: Small-signal gain of a Maxwell Garnett composite material as a function of the refractive index of the non-resonant host for different values of the inclusion volume fraction: (a) REB case [from Eq. (2.73)], (b) PRE case [from Eq. (2.68)], (c) the simplified model from.

Garnett composite geometry exhibits a monotonic growth with the increase of  $f_i$ . It increases to some maximum value with the increase of the host refractive index, and then decreases with further growth of  $n_h$ . The monotonic growth of  $g_0$  with  $f_i$  is due

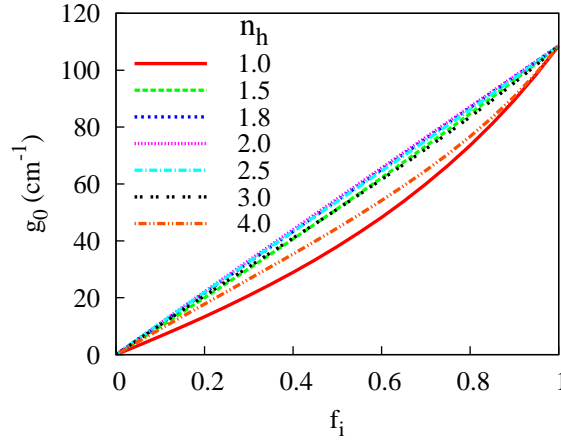


Figure 2.11: Small-signal gain of a Maxwell Garnett composite material as a function of the inclusion volume fraction for different values of the host refractive index.  $g_0$  is derived from Eq. (2.73) for REB case.

to the fact that, unlike in layered composite materials, the increase of the inclusion volume fraction in the Maxwell Garnett composite material is not accompanied by the decrease in the local field in an inclusion. The reason to the complex behavior of  $g_0$  as a function of  $n_h$  is as follows. It is seen from Eq (2.17) that  $g_0 \propto [\sqrt{\epsilon_{\text{eff}}}]^{-1} \text{Im} \chi_{\text{eff}}^{(1)}$ . Due to the electric field localization in the component with the lower refractive index,  $\text{Im} \chi_{\text{eff}}^{(1)}$  monotonically grows with the increase of  $n_h$ . However, the term  $[\sqrt{\epsilon_{\text{eff}}}]^{-1}$ , where  $\epsilon_{\text{eff}}$  is given by Eq. (1.1), decreases with the increase of  $n_h$ , and at some value of the host refractive index its decrease overcompensates the growth of  $\text{Im} \chi_{\text{eff}}^{(1)}$ . As a result,  $g_0$  starts to decrease with further increase of  $n_h$ .

It is important to keep in mind that the Maxwell Garnett model works well only for low volume fractions of the inclusions ( $f_i \lesssim 0.5$ ). It does not account for a percolation phenomenon that occurs when  $f_i$  is higher than a certain value.

In Fig. 2.12 we plot the small-signal gain coefficient as a function of the detuning  $\Delta$  for different values of the equilibrium population inversion  $w_{\text{eq}}$  with the fixed values  $f_i = 0.01$  and  $n_h = 1.3$ . As in the case of the layered composite geometry, one can

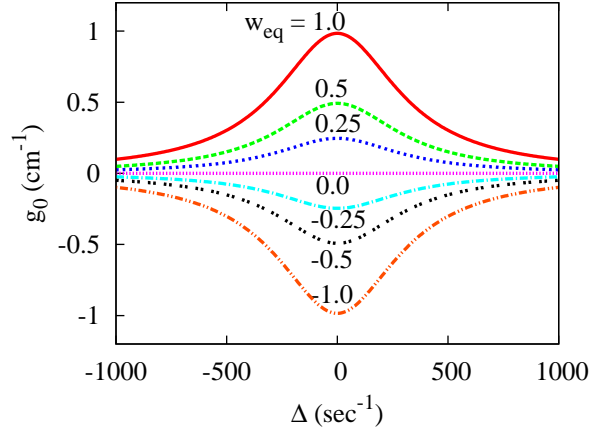


Figure 2.12: Small-signal gain of a Maxwell Garnett composite material as a function of the detuning of the optical field with respect to the molecular resonant frequency. Marked on the graphs are the values of equilibrium population inversion.

see the change from absorption to amplification as  $w_{\text{eq}}$  changes from -1 to 1.

The work reported in Section 2.4 is going to be submitted to the Journal of Physics A [116].

## 2.5 Conclusions

We have proposed a method for controlling and tailoring the basic laser properties of laser gain media, such as the radiative lifetime of the upper laser level, the small-signal gain coefficient, and the saturation intensity. The idea behind the method is

designing composite materials by mixing two or more materials on a nanoscale to obtain new laser gain media with the laser properties enhanced compared to those of the constituents. The enhancement can be achieved by implementing local-field effects that can significantly modify optical properties of materials. The composite-material approach has been used for enhancing the nonlinear properties of dielectric [25–29, 31, 32] and metal-dielectric [30, 117] composites. However, we are unaware of any previous systematic study of the modification of the laser properties of composite materials by the local-field effects. Our idea of composite laser has been published in the the Journal of the Optical Society of America [105].

Together with the simple proof-of-principle study, we also developed more sophisticated theoretical models describing the linear effective susceptibility of layered and Maxwell Garnett composite materials with resonant components of two types. The first type is a simple case of a resonant medium in which all the molecules or atoms are of the same sort. The second type of resonant component corresponds to a situation in which only a fraction of the molecules or atoms of the medium are in resonance with the optical field. The latter model is more realistic, as most of the laser gain media consist of species of different sorts. Along the way, we derived the expressions for the frequency shifts of the resonant features with respect to the actual resonances, which are the analogs of the famous Lorentz red shift in a homogeneous medium. These frequency shifts for the layered and Maxwell Garnett composite geometries with pure resonant emitters and resonant emitters in a background differ from the

Lorentz red shift and from each other.

We analyzed our theories of Layered and Maxwell Garnett composites for the following two physical cases. The first case is a layered composite material with the resonant component consisting of Rhodamine-doped PMMA. The second case is a Maxwell Garnett composite material with Nd:YAG nanoparticles as resonant inclusions. The layered geometry seems to be more promising for tailoring the optical properties of the composite laser gain media: under certain conditions the gain coefficient of the layered composite geometry can exceed the gain coefficients of its constituents. The theoretical models for layered and Maxwell Garnett composite geometries are to be submitted to the Journal of Physics A [116].

We have also experimentally investigated the influence of local-field effects on the radiative lifetimes of liquid suspensions of Nd:YAG nanoparticles. To determine which model (the real-cavity, the virtual-cavity model, or no-local-field-effects model) gives the best description of our experimental data, we compared the data with the predictions of these models. We find that we can rule out the virtual cavity model as it is in obvious disagreement with our data for any of the values of the quantum yield that we considered. We also find that the real cavity model can be used to provide a good fit to our data for the range of possible quantum yields. However, we cannot rule out the no-local-fields model on experimental grounds. If we assume that quantum yield is unity, the no-local-fields model is also in good agreement with our data. However, there is no theoretical reason to believe that local field effects would

not occur in these materials, and for this reason we feel that the real-cavity model best describes our experimental results. This work has been published in the Journal of the Optical Society of America [24].

## Chapter 3

# Microscopic Cascading in

# Fifth-Order Nonlinear

# Susceptibility Induced by

# Local-Field Effects

### 3.1 Introduction

The development of lithographic materials that can allow one to overcome the Rayleigh limit is crucial for improving the spatial resolution in optical lithography. Many approaches have been undertaken in this direction. It has been realized [118] and experimentally demonstrated [119] that  $N$ -photon absorbing materials allow one to achieve

$N$ -fold resolution enhancement in interference lithography. Boto, *et al.* [118] proposed to expose an  $N$ -photon lithographic material to an interference pattern produced by a quantum-mechanically entangled source. This procedure would allow one to record a fringe pattern with unit visibility and a period  $N$  times smaller than the Rayleigh  $\lambda/2$  limit. However, realization of the idea in the laboratory remains a challenge for experimentalists working in the field of quantum imaging.

Here we propose a novel principle for designing  $N$ -photon absorbing lithographic materials and materials with tailored high-order nonlinear response based on microscopic cascaded nonlinear effects.

Cascaded nonlinearities have proven to be very useful in the field of nonlinear optics because they allow a sequence of low-order responses to mimic a high-order response. Because lower-order nonlinearities are typically much stronger than higher-order nonlinearities, cascaded lower-order processes can be much more efficient than higher-order processes. It is useful to distinguish macroscopic cascading from microscopic cascading. Macroscopic cascading occurs as a result of propagation effects [62, 65, 67]. Somewhat more subtle is the origin of microscopic cascading, in which higher-order effects are induced in the response at the molecular level [60, 68].

In this chapter we show both theoretically and experimentally that there are microscopic cascaded effects in high-order nonlinearities, induced by local-field effects, that can be very significant and useful for various applications. In Section 3.2 we present a theoretical analysis of the nonlinear response of a medium, treated up to the



fifth order of nonlinearity, with local-field effects taken into account. We first address this problem by solving the Lorentz–Maxwell–Bloch equations (see Section 1.4). We expand the total susceptibility as a Taylor series in the electric field. We find that the resulting expression for the fifth-order nonlinear susceptibility is in disagreement with the straight-forward generalization of Bloembergen’s result [55] to fifth-order response. We resolve this apparent contradiction by solving the problem using a more careful implementation of Bloembergen’s approach [68]. The detailed calculation shows that there is no disagreement between the results of the local-field-corrected Maxwell–Bloch equations and that careful implementation. Moreover, the results show that there is a cascaded contribution coming from the third-order microscopic hyperpolarizability, together with the naively expected fifth order nonlinear term. This cascaded contribution is a consequence of local-field effects.

In Section 3.3 we analyze the relative values of the contributions from the fifth- and third-order microscopic hyperpolarizabilities to  $\chi^{(5)}$ , and we find that under certain conditions the cascaded third-order contribution can be as large as the direct fifth-order contribution.

In Section 3.4 we describe an experiment that allows us to separate the influence of microscopic cascading from the more-well-known macroscopic cascading, and we find conditions under which microscopic cascading is the dominant effect.

## 3.2 Theoretical Prediction of Microscopic Cascading

### 3.2.1 Maxwell–Bloch equations approach

A collection of two-level atoms with ground and excited states denoted respectively by  $a$  and  $b$ , interacting with an optical field closely tuned to an atomic resonance of the system, can be described by the Maxwell–Bloch equations (1.19). Accounting for local-field effects using the Lorentz local field (1.6) leads to a modified form of Eqs. (1.19), given by (1.22). Here we recall the steady-state solutions to Eqs. (1.22) for the case  $w_{\text{eq}} = -1$ :

$$w = -\frac{1}{1 + \frac{|E|^2/|E_s^0|^2}{1 + T_2^2(\Delta + \Delta_L w)^2}}; \quad (3.1a)$$

$$\sigma = \frac{\mu}{\hbar} \frac{wE}{\Delta + \Delta_L w + i/T_2}. \quad (3.1b)$$

Here  $E_s^0$  is the saturation field strength, defined by Eq. (1.25), and  $\Delta_L$  is the Lorentz red shift, given by Eq. (1.23).

As a consequence of the presence of the local-field-induced inversion-dependent frequency shift  $\Delta_L w$  in Eq. (3.1a), the steady-state solution for the population inversion  $w$  becomes a cubic equation. In a certain range of parameters it has three real roots with absolute values not exceeding unity. The existence of three different

physically meaningful solutions for the population inversion is associated with the phenomenon of local-field-induced optical bistability [41, 43, 44], first discussed by Hopf, Bowden, and Louisell [41]. In Appendix B we identify the parameter space in which Eq. (3.1a) has multiple physical solutions, and show that it cannot be reached for the example system that we consider in Section 3.3, the excitation of a collection of sodium atoms at frequencies close to the  $3s \rightarrow 3p$  resonance.

For such systems, the nonlinear response can be studied through an approximate solution of Eq. (3.1a), obtained through a power-series expansion with respect to the electric field parameter  $x = |E|^2/|E_s^0|^2$ . Assuming  $x$  to be a small quantity, we perform a Taylor series expansion of  $w$  in terms of  $x$ , retaining only terms up to the second power, as we are interested only in treating saturation effects up to the fifth order in  $E$ . The resultant solution for  $w$  takes the form

$$w = -1 + \frac{1}{1 + T_2^2(\Delta - \Delta_L)^2} \frac{|E|^2}{|E_s^0|^2} - \frac{1 + T_2^2(\Delta^2 - \Delta_L^2)}{[1 + T_2^2(\Delta - \Delta_L)^2]^3} \frac{|E|^4}{|E_s^0|^4}. \quad (3.2)$$

The total susceptibility  $\chi$ , including linear and nonlinear interactions, is obtained in Section 1.4 and is given by Eq. (1.27), which we recall here:

$$\chi = \frac{N|\mu|^2 T_2}{\hbar} \frac{w}{T_2(\Delta + \Delta_L w) + i} = \frac{N|\mu|^2}{\hbar} \frac{(-w)}{(\omega_{ba} + \Delta_L(-w) - \omega) - i/T_2}. \quad (3.3)$$

Eqs. (3.2) and (3.3) illustrate the physical effect of the nonlinearity: it is through the modification of the inversion parameter  $w$  from its equilibrium value of  $-1$ , and that

modification is twofold. First, the overall amplitude of the response is modified by the fact that  $-w$  differs from unity, and second, the resonant frequency is modified from  $\omega_{ba} + \Delta_L$  (the Lorentz-shifted low-intensity resonance frequency) to  $\omega_{ba} + \Delta_L(-w)$ .

It is convenient to represent the total susceptibility as a power series expansion with respect to the electric field:

$$\chi = \chi^{(1)} + 3\chi^{(3)}|E|^2 + 10\chi^{(5)}|E|^4 + \dots \quad (3.4)$$

Then, substituting the expansion of the population inversion (3.2) into Eq. (3.3) and making use of the representation (3.4) of the total susceptibility, we find the expressions for the linear and the nonlinear susceptibilities to be

$$\chi^{(1)} = -\frac{N|\mu|^2 T_2}{\hbar} \frac{T_2(\Delta - \Delta_L) - i}{1 + T_2^2(\Delta - \Delta_L)^2}, \quad (3.5a)$$

$$\chi^{(3)}|E_s^0|^2 = \frac{N|\mu|^2 T_2}{3\hbar} \times \frac{(T_2\Delta + i)[T_2(\Delta - \Delta_L) - i]^2}{[1 + T_2^2(\Delta - \Delta_L)^2]^3}, \quad (3.5b)$$

and

$$\chi^{(5)}|E_s^0|^4 = -\frac{N|\mu|^2 T_2}{10\hbar} \frac{(T_2\Delta + i)[1 - iT_2\Delta_L + T_2^2(\Delta - \Delta_L)(\Delta + 2\Delta_L)]}{[1 + T_2^2(\Delta - \Delta_L)^2]^3 [T_2(\Delta - \Delta_L) + i]^2}. \quad (3.5c)$$

### 3.2.2 The Naïve Local-Field Correction

We next attempt to bring expressions (3.5) for the local-field-corrected susceptibilities to the form of Bloembergen's result. The straight-forward generalization [56, 57] of the Bloembergen's result to the case of the saturation effects [which are described by an odd-order nonlinearity as  $\chi^{(i)} = \chi^{(i)}(\omega = \omega + \omega - \omega + \dots)$ ] reads

$$\chi^{(i)} = N\gamma_{\text{at}}^{(i)}|L|^{i-1}L^2, \quad (3.6)$$

where  $\gamma_{\text{at}}^{(i)}$  is the  $i$ th-order microscopic hyperpolarizability (ineq1).

Using Eqs. (1.19) and (1.21) for an isolated atom in free space, we write

$$\tilde{p}(t) = p \exp(-i\omega t) + \text{c. c.} \quad (3.7)$$

with

$$p = \mu^* \sigma \quad (3.8)$$

for the atom's dipole moment  $p$ . The Taylor series expansion for  $p$  with respect to the electric field yields

$$p = \gamma_{\text{at}}^{(1)} E + 3\gamma_{\text{at}}^{(3)} |E|^2 E + 10\gamma_{\text{at}}^{(5)} |E|^4 E + \dots \quad (3.9)$$

Here

$$\gamma_{\text{at}}^{(1)} = -\frac{|\mu|^2 T_2}{\hbar} \frac{T_2 \Delta - i}{1 + T_2^2 \Delta^2} \quad (3.10)$$

is the linear polarizability, and

$$\gamma_{\text{(at)}}^{(3)} |E_s^0|^2 = \frac{|\mu|^2 T_2}{3\hbar} \frac{T_2 \Delta - i}{(1 + T_2^2 \Delta^2)^2} \quad (3.11a)$$

and

$$\gamma_{\text{(at)}}^{(5)} |E_s^0|^4 = -\frac{|\mu|^2 T_2}{10\hbar} \frac{T_2 \Delta - i}{(1 + T_2^2 \Delta^2)^3} \quad (3.11b)$$

are the third-order and fifth-order microscopic hyperpolarizabilities, respectively.

The definition of the factor  $L$  in terms of the dielectric function  $\epsilon^{(1)}$  is given by Eq. (1.15). The next step is to find an expression for the factor  $L$  in terms of the detuning  $\Delta$  and the Lorentz red shift  $\Delta_L$ . Setting  $w = -1$  in Eq. (3.3), we arrive at

$$\chi^{(1)} = -\frac{N|\mu|^2 T_2}{\hbar} \frac{1}{T_2(\Delta - \Delta_L) + i}, \quad (3.12)$$

and so

$$\epsilon^{(1)} = 1 + 4\pi\chi^{(1)} = 1 - \frac{4\pi N|\mu|^2 T_2}{\hbar} \frac{1}{T_2(\Delta - \Delta_L) + i}. \quad (3.13)$$

Using (3.13) in (1.15), we obtain

$$L = \frac{T_2 \Delta + i}{T_2(\Delta - \Delta_L) + i}. \quad (3.14)$$

Making use of Eq. (3.10) for microscopic polarizability, Eqs. (3.11) for microscopic hyperpolarizabilities, and Eq. (3.14) for factor  $L$ , we find that

$$N\gamma_{\text{at}}^{(1)}L = \chi^{(1)} \quad (3.15\text{a})$$

of Eq. (3.5a),

$$N\gamma_{\text{at}}^{(3)}|L|^2L^2 = \chi^{(3)} \quad (3.15\text{b})$$

of Eq. (3.5b), but

$$N\gamma_{\text{at}}^{(5)}|L|^4L^2 \neq \chi^{(5)} \quad (3.15\text{c})$$

of Eq. (3.5c). In fact,

$$N\gamma_{\text{at}}^{(5)}|L|^4L^2 = \chi^{(5)} \frac{1 + T_2^2(\Delta - \Delta_L)^2}{1 - iT_2\Delta_L + T_2^2(\Delta - \Delta_L)(\Delta + 2\Delta_L)}. \quad (3.16)$$

Thus, the naïve local-field correction (3.6) in terms of  $L$ 's is in disagreement with the correct result derived from the Maxwell–Bloch equations.

To find the origin of this disagreement, we address the problem of treating the saturation up to the fifth order of nonlinearity, following the recipe suggested by Bloembergen [55], rather than using the straight-forward generalization given by Eq. (3.6). Our calculations are presented in the following subsection.

### 3.2.3 Bloembergen's approach

The polarization  $P$  entering Eq. (2.1) is the total polarization, given by the sum of the contributions proportional to first, third and fifth power of the *local* electric field as

$$P = P^{(1)} + P^{(3)} + P^{(5)} + \dots \quad (3.17)$$

Here

$$P^{(1)} = N\gamma_{\text{at}}^{(1)} E_{\text{loc}}, \quad (3.18a)$$

$$P^{(3)} = N\gamma_{\text{at}}^{(3)} |E_{\text{loc}}|^2 E_{\text{loc}}, \quad (3.18b)$$

and

$$P^{(5)} = N\gamma_{\text{at}}^{(5)} |E_{\text{loc}}|^4 E_{\text{loc}}. \quad (3.18c)$$

Using Eq. (2.1) in (3.18a), we obtain

$$P^{(1)} = \frac{\epsilon^{(1)} - 1}{4\pi} \left[ E + \frac{4\pi}{3} P^{(3)} + \frac{4\pi}{3} P^{(5)} + \dots \right]. \quad (3.19)$$

The electric displacement vector  $D$  is defined as

$$D = E + 4\pi P = E + 4\pi P^{(1)} + 4\pi P^{(3)} + 4\pi P^{(5)} + \dots \quad (3.20)$$



Substituting (3.19) into (3.20), we find that

$$D = \epsilon^{(1)}E + 4\pi P^{\text{NLS}}, \quad (3.21)$$

where

$$P^{\text{NLS}} = L(P^{(3)} + P^{(5)} + \dots) \quad (3.22)$$

is the nonlinear source polarization, introduced by Bloembergen [55].

Substituting expression (3.19) for the polarization  $P^{(1)}$  into Eq. (3.17) for the total polarization, we find that

$$P = \chi^{(1)}E + P^{\text{NLS}}. \quad (3.23)$$

Substituting Eq. (2.1) for the local field into Eqs. (3.18b) and (3.18c) for the polarizations  $P^{(3)}$  and  $P^{(5)}$  and dropping out the terms scaling with higher than the fifth power of the electric field, we obtain

$$\begin{aligned} P^{(3)} = & 3N\gamma_{\text{at}}^{(3)}|L|^2L|E|^2E \\ & + \left[ 24\pi N^2(\gamma_{\text{at}}^{(3)})^2|L|^4L^2 + 12\pi N^2|\gamma_{\text{at}}^{(3)}|^2|L|^6 \right] |E|^4E \end{aligned} \quad (3.24a)$$

and

$$P^{(5)} = 10N\gamma_{\text{at}}^{(5)}|L|^4L|E|^4E. \quad (3.24b)$$

Note that  $P^{(3)}$  contains terms proportional to the fifth power of the electric field.

Substituting (3.24) into (3.22), and (3.22) into (3.23), we find the total polarization

to be

$$\begin{aligned}
P &= \chi^{(1)}E + 3N\gamma_{\text{at}}^{(3)}|L|^2L^2|E|^2E \\
&\quad + \left[ 24\pi N^2(\gamma_{\text{at}}^{(3)})^2|L|^4L^3 + 12\pi N^2|\gamma_{\text{at}}^{(3)}|^2|L|^6L \right. \\
&\quad \left. + 10N\gamma_{\text{at}}^{(5)}|L|^4L^2 \right] |E|^4E + \dots .
\end{aligned} \tag{3.25}$$

Alternatively, the total polarization can be represented as a Taylor series expansion with respect to the average electric field as

$$P = \chi E = \chi^{(1)}E + 3\chi^{(3)}|E|^2E + 10\chi^{(5)}|E|^4E + \dots . \tag{3.26}$$

Equating (3.25) and (3.26), we obtain

$$\chi^{(1)} = N\gamma_{\text{at}}^{(1)}L, \tag{3.27a}$$

$$\chi^{(3)} = N\gamma_{\text{at}}^{(3)}|L|^2L^2, \tag{3.27b}$$

and

$$\chi^{(5)} = N\gamma_{\text{at}}^{(5)}|L|^4L^2 + \frac{24\pi}{10}N^2(\gamma_{\text{at}}^{(3)})^2|L|^4L^3 + \frac{12\pi}{10}N^2|\gamma_{\text{at}}^{(3)}|^2|L|^6L. \tag{3.27c}$$

Using expression (3.14) for the local-field correction factor, obtained in Section 3.2.2, one can show that Eqs. (3.27) for the local-field-corrected first, third, and fifth order

susceptibilities are equivalent to Eqs. (3.5), obtained using Maxwell-Bloch approach. Thus, two different approaches – the Lorentz–Maxwell–Bloch equations and Bloembergen’s approach – bring us to the same result for the local-field-corrected susceptibilities. This is of course not surprising, since both approaches are just different ways of implementing Bloembergen’s scheme.

The expressions for local-field-corrected  $\chi^{(1)}$  and  $\chi^{(3)}$  do not display any peculiarity, while Eq. (3.27c) for  $\chi^{(5)}$  deserves special attention. The first term on the right-hand side of the equation is due to a direct contribution from the fifth-order microscopic hyperpolarizability, while the two extra terms come from the contribution of the third-order microscopic hyperpolarizability. These extra contributions are a manifestation of local-field effects. We denote for convenience the direct contribution to the fifth-order susceptibility as

$$\chi_{\text{dir}}^{(5)} = N\gamma_{\text{at}}^{(5)}|L|^4L^2. \quad (3.28)$$

Similarly, the sum of the second and third terms on the left-hand side of (36c) (the microscopic cascaded contribution to  $\chi^{(5)}$ ) can be denoted as

$$\chi_{\text{micro}}^{(5)} = \frac{12\pi}{10}N^2 \left[ 2(\gamma_{\text{at}}^{(3)})^2|L|^4L^3 + |\gamma_{\text{at}}^{(3)}|^2|L|^6L \right]. \quad (3.29)$$

Then the total local-field-corrected  $\chi^{(5)}$ , which is the sum of the two contributions,

can be written as

$$\chi^{(5)} = \chi_{\text{dir}}^{(5)} + \chi_{\text{micro}}^{(5)}. \quad (3.30)$$

As we pointed out in preceding sections of this paper, the result that we obtained for  $\chi^{(5)}$  does not agree with that predicted by a straight-forward generalization of the Bloembergen's result given by Eq. (3.6). It is evident from Eqs. (3.6) and (3.27c) that the generalization (3.6) predicts the direct term only (the term proportional to  $\gamma_{\text{at}}^{(5)}$ ) in the expression for the local-field-corrected  $\chi^{(5)}$ , and does not account for the cascaded contributions coming from the third-order microscopic hyperpolarizability. We have shown in this section that the cascaded terms arise from substituting the *nonlinear* local field into the expression (3.18b) for  $P^{(3)}$ . If we were limiting ourselves to considering the third-order nonlinearity (i. e., the lowest-order nonlinearity in our system), then we would need only to substitute the linear local field,

$$E_{\text{loc}} = E + \frac{4\pi}{3} P^{\text{L}},$$

into equation (3.18b) to deduce that

$$P^{(3)} = 3N\gamma_{\text{at}}^{(3)} |L|^2 L |E|^2 E,$$

instead of  $P^{(3)}$  in the form of Eq. (3.24a). Thus, one clearly cannot simply use the generalization (3.6) to treat nonlinearity of the order higher than the lowest order of the nonlinearity present in the system of interest.

To develop insight into the relative contributions of the third- and fifth-order hyperpolarizabilities to the local-field-corrected fifth-order susceptibility (3.27c), we conduct a comparative analysis of the direct and cascaded terms. The analysis identifies the importance of the cascaded terms, and is presented in the following section.

### 3.3 Numerical Analysis

We perform our analysis based on a realistic example, taking the values of parameters for the sodium  $3s \rightarrow 3p$  transition. The transition dipole moment is  $|\mu| = 5.5 \times 10^{-18}$  esu and the population relaxation time is  $T_1 = 16$  ns. The value of the coherence relaxation time  $T_2$  can be found according to [45]

$$\gamma_2 = \frac{\gamma_{\text{nat}}}{2} + \gamma_{\text{self}}.$$

Here  $\gamma_2 = 1/T_2$  is the atomic linewidth,  $\gamma_{\text{nat}} = 1/T_1$  is the natural (radiative) linewidth, and the collisional contribution  $\gamma_{\text{self}}$  is given by

$$\gamma_{\text{self}} = \frac{4\pi N |\mu|^2}{\hbar} \sqrt{\frac{2J_g + 1}{2J_e + 1}},$$

where  $J_g$  and  $J_e$  are the angular momentum quantum numbers of the ground and excited states, respectively (for the sodium  $3s \rightarrow 3p$  transition,  $J_g = 0$  and  $J_e = 1$ ).

In the theoretical analysis developed in Section 3.2 we have implicitly used the

rotating wave approximation (RWA) to describe the atomic response. Before proceeding here we confirm the validity of that approximation for our example of the sodium  $3s \rightarrow 3p$  transition. We begin by comparing our RWA expression (3.12) to a more precise expression in which the RWA approximation is not made,

$$\chi_{\text{non-RWA}}^{(1)} = \frac{N|\mu|^2}{\hbar} \left[ \frac{1}{(\omega_{ba} - \omega + \Delta_L) - i/T_2} + \frac{1}{(\omega_{ba} + \omega - \Delta_L) + i/T_2} \right], \quad (3.31)$$

where it is the second term in (3.31) that is missing in the RWA. Evaluating  $\text{Re}(\chi_{\text{non-RWA}}^{(1)})/\text{Re}(\chi^{(1)})$  and  $\text{Im}(\chi_{\text{non-RWA}}^{(1)})/\text{Im}(\chi^{(1)})$  over the range of atomic densities and frequency detunings that we use in this section, we find that even at  $N = 10^{17} \text{ cm}^{-3}$  the maximum deviations of those ratios from unity are only a fraction of a percent. And even if the ratios are raised to the third and fifth powers, as a rough sense of how the higher order susceptibilities will be sensitive to expressions beyond the RWA, we find that their maximum deviations from unity are at most a few percent. Thus we feel comfortable in using the RWA in our identification of the range of validity of different approximations, and in our comparison of the contributions of the direct and cascaded fifth order terms.

Our goal is to identify the parameter space where the power-series expansion of the local-field-corrected susceptibility, including the total  $\chi^{(5)}$  (3.27c), is valid. This defines what we call the “full fifth-order model.” Along the way it will be useful to also identify the ranges of validity of some other susceptibility models:

- (a) the local-field-corrected  $\chi^{(1)}$ , which is the expression for the total susceptibility neglecting the nonlinear interactions (we refer to this as the “linear model”);
- (b) the power-series expansion for the local-field-corrected total susceptibility given up to the third order of nonlinearity (we refer to this expansion as the “third-order model”);
- (c) the power-series expansion for the local-field-corrected total susceptibility given up to fifth order of nonlinearity neglecting the cascaded contribution (we refer to this as the “direct fifth-order model”);
- (d) the full expression for the susceptibility obtained without accounting for local-field effects, given as [56]

$$\chi = \frac{-N|\mu|^2 T_2}{\hbar} \frac{\Delta T_2 - i}{1 + \Delta^2 T_2^2 + |E|^2/|E_s^0|^2} \quad (3.32)$$

(we refer to this model as “full model without LFE”).

We identify the range of parameters over which the models are valid by comparing them to the full expression for the local-field-corrected total susceptibility,

$$\chi = \frac{N|\mu|^2 T_2}{\hbar} \frac{w}{T_2(\Delta + \Delta_L w) + i}, \quad (3.33)$$

where the population inversion  $w$  is given by (3.1a) (we refer to this model as the

“full model”). In order for a model to be valid for a given range of parameters (the atomic density and electric field strength), we require that at a given atomic density and normalized electric-field strength  $|E|^2/|E_s^0|^2$  the difference between the full model and the other model at any detuning is not greater than 3% of the peak value of the full model. Using this criterion, the ranges over which the models are valid are marked with colored areas in Fig. 3.1. The full model of Eq. (3.33) is valid everywhere in

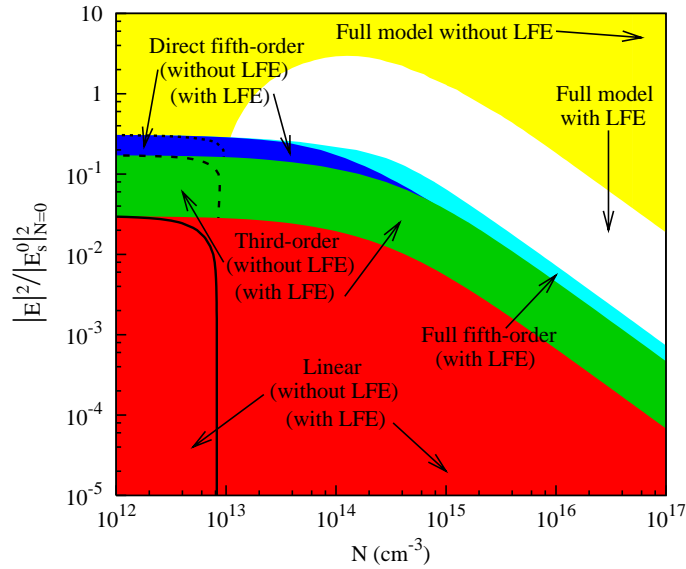


Figure 3.1: The ranges of validity of the various models described in the text for the total susceptibility of a collection of two-level atoms. The area at the bottom shows the range of validity of the linear model; local field effects (LFE) are important in the region on the right but can be ignored on the left. Moving upward on the plot, the next area shows the range of validity of the third-order model. Again, LFE can be ignored in the region on the left, and of course this model also accurately describes the response in the region below it. The next two regions show the ranges of validity of the direct fifth-order model and the full fifth-order model. In the white region above these colored regions, the full model of Eq. (3.33) must be used, and finally in the region at the top of the plot accurate predictions can be obtained by ignoring LFE as long as the full model of Eq. (3.32) is used.

the plot area. The full model without LFE can be used at higher strengths of the



applied field where the saturation effect is strong, while at small values of the atomic densities the local-field effects are unimportant and one can neglect them in both the full model and the power series expansions. The third-order model is valid in the range where the linear model is valid. The direct and full fifth-order models are valid in the range of validity of the third model; the full fifth-order model is also valid in the range of validity of the direct fifth-order model.

Comparing the full fifth-order model to other power-series expansion models, we conclude that the former has a broader range of validity. As well, we find that the full fifth-order model gives a more precise description of the local-field-corrected susceptibility than the other power-series expansions in the ranges where all these models are valid. As an example, we plot the real and imaginary parts of the local-field-corrected susceptibility given by the different models as the function of the normalized frequency detuning  $\Delta T_2$ , where the value of  $T_2$  is taken at zero atomic density, in Fig. 3.2. We see that for a given set of parameters all the power-series expansions describe the total susceptibility fairly well, but the inset reveals that the full fifth-order model works the best of all, as there is no apparent disagreement between it and the full model.

We now consider how the presence of the cascaded term affects the size and frequency dependence of  $\chi^{(5)}$ . In Fig. 3.3 we plot the ratio of the absolute values of the cascaded and direct terms as the function of the normalized detuning  $\Delta T_2$  for several values of the atomic density  $N$  within the range of  $1 \times 10^{14}$  to  $1 \times 10^{17}$   $\text{cm}^{-3}$ .

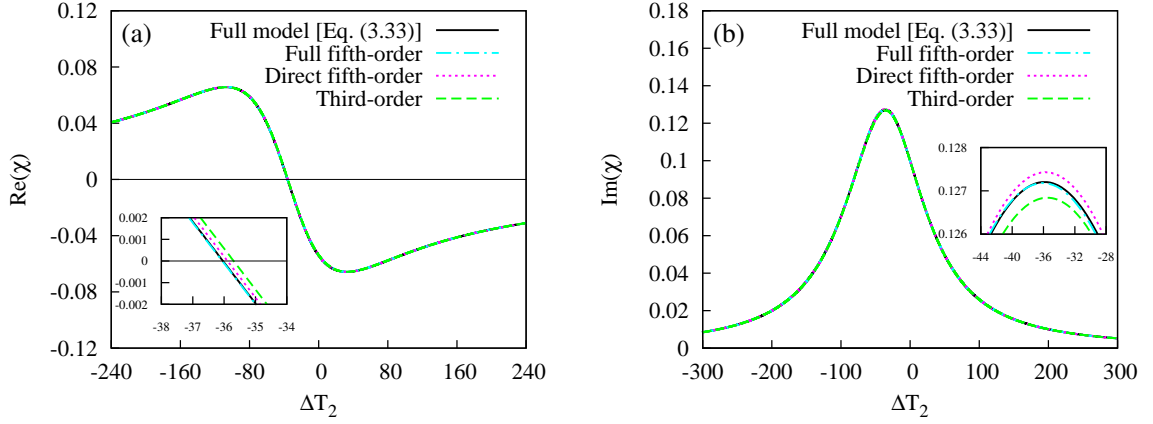


Figure 3.2: Real (a) and imaginary (b) parts of the total susceptibility of a collection of two-level atoms as functions of the detuning plotted for  $N = 10^{16} \text{ cm}^{-3}$  and  $|E|^2/|E_s^0|_{N=0}^2 = 10^{-3}$ . The susceptibility is given by different models, as depicted in the legend.

We take the value of  $T_2$  at  $N = 0$  in the normalized frequency detuning. It can be

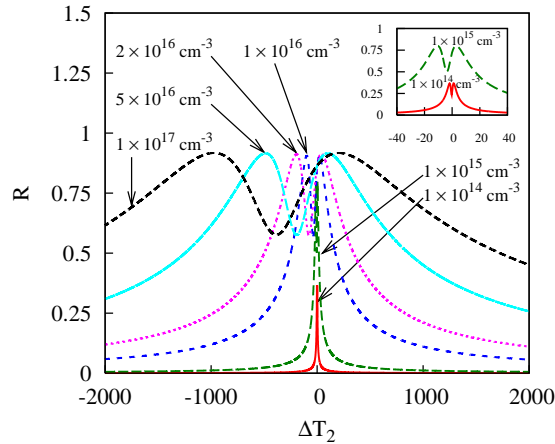


Figure 3.3: The ratio  $R = |\chi_{\text{micro}}^{(5)}|/|\chi_{\text{dir}}^{(5)}|$  of the absolute values of the microscopic cascaded and direct contributions to the local-field-corrected  $\chi^{(5)}$  as a function of the normalized detuning  $\Delta T_2$  plotted for several values of the atomic density falling into the range between  $1 \times 10^{14}$  and  $1 \times 10^{17} \text{ cm}^{-3}$ . The inset resolves the absolute values of the ratio for the atomic densities  $N = 10^{14}$  and  $10^{15} \text{ cm}^{-3}$ .

seen from Fig. 3.3 that the influence of the local-field effects is two-fold. First, the

local-field effects tend to shift the resonance feature towards lower frequencies by the amount  $\Delta_L$ . The frequency shift grows linearly with the increase of the density  $N$ . Second, the ratio  $|\chi_{\text{micro}}^{(5)}|/|\chi_{\text{dir}}^{(5)}|$  grows with increasing atomic density, as is especially clear from the inset in Fig. 3.3. This growth saturates at atomic densities higher than  $10^{16} \text{ cm}^{-3}$ , because homogeneous collisional broadening comes into play. Clearly, the cascaded term has a non-negligible contribution to the fifth-order susceptibility.

The result shown in Fig. 3.3, although informative, does not present a complete picture of the contribution to  $\chi^{(5)}$  from the cascaded term. We can learn more by considering the real and imaginary parts of  $\chi_{\text{dir}}^{(5)}$  and  $\chi_{\text{micro}}^{(5)}$ . These are plotted as functions of the normalized detuning  $\Delta T_2$ , where  $T_2$  is taken at  $N = 0$ , for different values of the atomic density in Fig. 3.4(a), 3.4(c), and 3.4(e). For the purpose of comparison, we also plot the total fifth-order susceptibility given by Eq. (3.30), which is the sum of the direct and cascaded contributions, and  $\chi_{\text{dir}}^{(5)}$  [see Fig. 3.4(b), 3.4(d), and 3.4(f)]. The microscopic cascaded terms make an insignificant contribution until atomic densities reach on the order of  $10^{13}$ – $10^{14} \text{ cm}^{-3}$  [see Fig. 3.4(a) and 3.4(b)]. As the atomic density increases, the contribution from the microscopic cascaded term becomes more pronounced, as one can see from Fig. 3.4(d). The difference becomes even more significant with further increase of the atomic density, and saturates at the densities higher than  $10^{16} \text{ cm}^{-3}$ .

Taking a careful look at the contribution to  $\chi^{(5)}$  from the microscopic cascaded term [better seen in Fig. 3.4(f)], one can see not only a line shape distortion and a

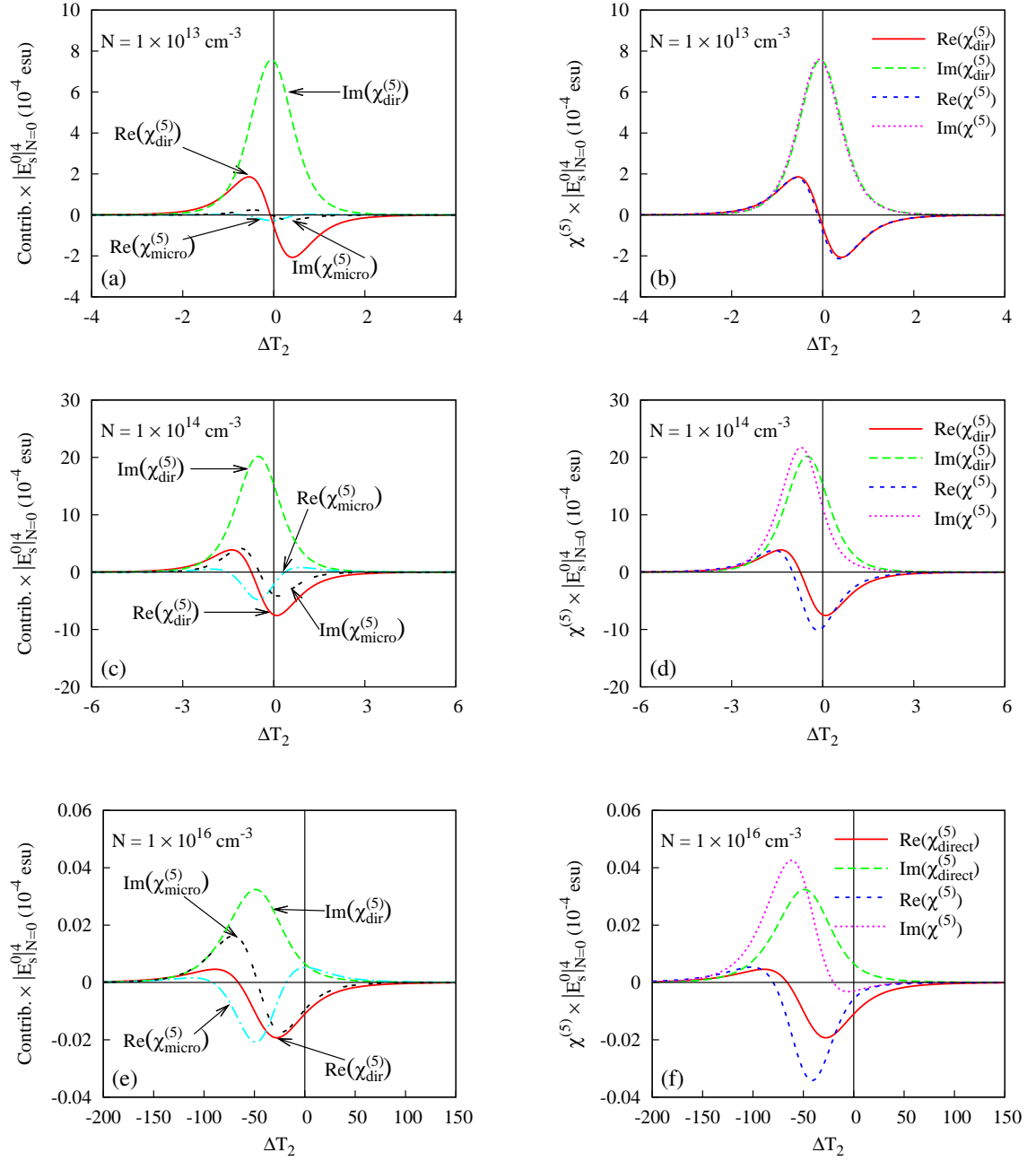


Figure 3.4: Real and imaginary parts of the direct and microscopic cascaded contributions to  $\chi^{(5)}$ ,  $\chi_{\text{dir}}^{(5)}$  and  $\chi_{\text{micro}}^{(5)}$  (a, c, e) and the sum of the contributions,  $\chi_{\text{total}}^{(5)}$ , plotted together with  $\chi_{\text{dir}}^{(5)}$  (b, d, f) as functions of the normalized detuning for different values of the atomic density  $N$ .

frequency shift of the maximum, but also a sign change of the imaginary part of  $\chi^{(5)}$  in a certain range of detuning. This sign change, of course, cannot be observed in the total response of the two-level atom, since there is net absorption.

### 3.4 Experimental Evidence and Applications of Microscopic Cascading

In the previous sections and in our recent publication [120], we have shown how local-field effects can act as a mechanism that leads to cascaded microscopic nonlinear response. In this section, we describe an experiment on separating the microscopic cascaded contribution to the fifth-order nonlinear susceptibility [121]. This is, to the best of our knowledge, the first experiment of this kind.

We recall the more general results for the local-field-corrected linear and nonlinear susceptibilities for a centrosymmetric medium from the previous sections (see Eqs. (3.27)):

$$\chi_{\text{LFC}}^{(1)} = N\gamma_{\text{at}}^{(1)}L, \quad (3.34a)$$

$$\chi_{\text{LFC}}^{(3)} = N\gamma_{\text{at}}^{(3)}|L|^2L^2, \quad (3.34b)$$

and

$$\begin{aligned}\chi_{\text{LFC}}^{(5)} &= N\gamma_{\text{at}}^{(5)}|L|^4L^2 \\ &+ \frac{24\pi}{10}N^2(\gamma_{\text{at}}^{(3)})^2|L|^4L^3 + \frac{12\pi}{10}N^2|\gamma_{\text{at}}^{(3)}|^2|L|^6L.\end{aligned}\quad (3.34c)$$

Here we added the subscripts “LFC” to the susceptibilities in order to distinguish them from the *effective* (total measured) fifth-order susceptibility, which we denote  $\chi_{\text{eff}}^{(5)}$ , as the latter has an extra, macroscopic (propagational) cascaded term which is not accounted for in the derivation of Eqs. (3.34).

We recall that the first term on the right-hand side of Eq. (3.34c) is due to the direct contribution from the fifth-order microscopic hyperpolarizability  $\gamma_{\text{at}}^{(5)}$ , while the two extra terms come from the cascaded contribution of the third-order microscopic hyperpolarizability  $\gamma_{\text{at}}^{(3)}$ . As earlier in this chapter, we refer to the direct term as  $\chi_{\text{dir}}^{(5)}$  [Eq. (3.28)], and to the microscopic cascaded terms as  $\chi_{\text{micro}}^{(5)}$  [Eq. (3.29)]. In such a way, our local-field-corrected fifth-order susceptibility can be represented as

$$\chi_{\text{LFC}}^{(5)} = \chi_{\text{dir}}^{(5)} + \chi_{\text{micro}}^{(5)}. \quad (3.35)$$

Based on the predictions of Eq. (3.34c), one can conclude that it should be possible to use microscopic cascading to induce a large cross section for three-photon absorption (which is proportional to the imaginary part of  $\chi^{(5)}$ ) by making use of a material with a large value of  $\gamma_{\text{at}}^{(3)}$ . The ability to excite three-photon absorption efficiently could

have important implications to nonlinear microscopy and to quantum imaging. This observation motivated us to undertake a proof-of-principle experiment in an attempt to isolate the microscopic cascaded contribution to the fifth-order susceptibility.

It is clear from Eq. (3.34c) that  $\chi_{\text{dir}}^{(5)}$  is proportional to the molecular (or atomic) density  $N$ , whereas  $\chi_{\text{micro}}^{(5)}$  is proportional to  $N^2$ . Hence, in order to experimentally separate the two contributions to the fifth-order susceptibility, one should measure the latter as a function of the molecular or atomic density. We have performed such a measurement in a mixture of carbon disulfide  $\text{CS}_2$  and fullerene  $\text{C}_{60}$ , both of which are highly-nonlinear materials.

Our experimental setup is based on a degenerate four-wave mixing (DFWM) scheme [122] (see Fig. 3.5) that allows one to separate the effects due to different orders of nonlinearity. Two beams of equal intensity at 532 nm from a frequency-doubled

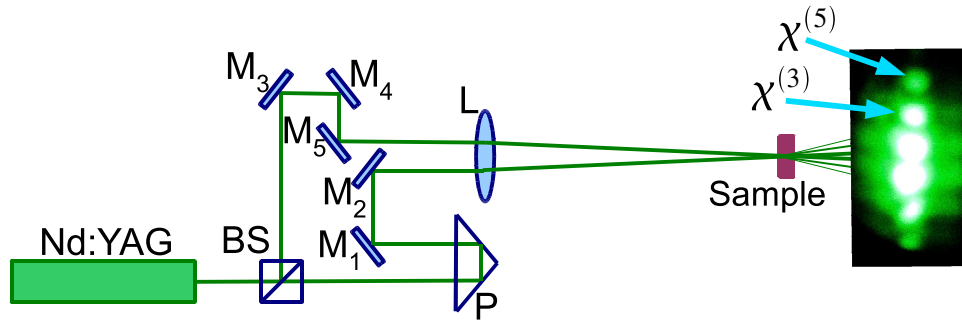


Figure 3.5: Experimental setup for DFWM. Nd:YAG - 35-ps, 10-Hz, 532-nm Nd:YAG laser, BS - beam splitter, P - prism (delay arm),  $M_1$ – $M_5$  - directing mirrors, L - focusing lens, Sample - 2-mm quartz cell containing a mixture of  $\text{CS}_2$  and  $\text{C}_{60}$ .

Nd:YAG laser producing 35-ps pulses were sent into a 2-mm quartz cell containing a mixture of carbon disulfide ( $\text{CS}_2$ ) and fullerene  $\text{C}_{60}$ , and we observed self-diffraction

phenomena (see the photograph in Fig. 3.5). The first order of diffraction is a consequence of the third-order nonlinear effect, while the second-order diffracted beam results from the fifth-order nonlinearity.

We measured the intensities of the first- and second-order diffracted beams for various concentrations of  $C_{60}$  in  $CS_2$ . In order to correct the nonlinear signals for the absorption present in the medium, we measured the linear absorption coefficient  $\alpha$  and multiplied our nonlinear signal intensities by the term  $(\alpha l \exp(\alpha l/2)/[1-\exp(-\alpha l)])^{2n}$ , where  $l$  is the length of the nonlinear medium, and  $2n+1$  is the order of the nonlinearity. We also performed an open-aperture Z-scan measurement [123] to account for the nonlinear absorption in our samples. Extracting the values of the normalized transmission  $T_{\text{norm}}$  from the Z-scan measurements, we divided our nonlinear intensities by  $(T_{\text{norm}})^{2n+1}$ . The third- and fifth-order nonlinear signal intensities, corrected for the linear and nonlinear absorptions and plotted on a logarithmic scale as functions of the incident beam intensity, displayed the slopes equal to 3 and 5, respectively (see Fig. 3.6).

The DFWM experiment yields the absolute values of the nonlinear susceptibilities. In order to extract these values from the measured intensities of the diffracted beams, we used the expression [124]

$$I_s = |\chi_{\text{meas}}^{(2n+1)}|^2 I^{2n+1} \left(\frac{n_0 c}{8\pi}\right)^{-2n} \left(\frac{n_0 c}{2\pi\omega l}\right)^{-2} \Xi(\theta), \quad (3.36)$$

relating the measured intensity  $I_s$  of the nonlinear signal to the corresponding non-



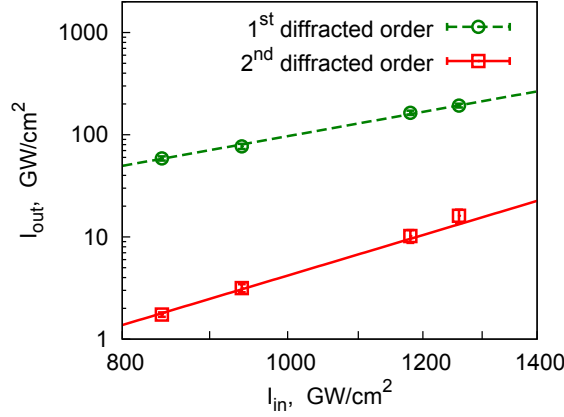


Figure 3.6: Intensities of the first (green circles) and second (red squares) diffracted orders, corresponding to  $\chi^{(3)}$  and  $\chi^{(5)}$  interactions, respectively, as functions of the incident beam intensity plotted on a logarithmic scale. The lines are the least-square fits by a cubic (green dashed line) and fifth-order (red solid line) polynomials.

linear susceptibility  $|\chi_{\text{meas}}^{(2n+1)}|$ . Here  $I_1$  and  $I_2$  are the intensity of an incident beam,  $c$  is the speed of light *in vacuo*,  $n_0$  is the refractive index of the medium,  $\theta$  is half-angle between the interacting beams in the experiment, and  $\Xi(\theta)$  is the phase mismatch term. We normalized our measured nonlinear susceptibilities to the known value of  $\chi^{(3)}$  of the pure CS<sub>2</sub>, which is  $2.2 \times 10^{-12}$  esu [56] in order to extract their values from the experimentally measured intensities.

In Fig. 3.7 we present the typical measured  $|\chi^{(3)}|$  and  $|\chi_{\text{eff}}^{(5)} \Xi(\theta)|$  as functions of the molar concentration  $N_{\text{C}_{60}}$  of C<sub>60</sub>. Here and below in the paper we do not make an attempt to correct the values of  $\chi_{\text{eff}}^{(5)}$  for the phase mismatch, as we cannot precisely determine the value of  $\Xi(\theta)$  in our experiment. The possible sources of error include lack of precision in measuring the angle between the interacting beams and

imperfections in the geometry of the experiment. We plot the product  $|\chi_{\text{eff}}^{(5)} \Xi(\theta)|$ , as we can extract its values from our experiment using Eq. (3.36) with a good precision.  $\text{CS}_2$  and  $\text{C}_{60}$  have nonlinear response of opposite sign, which is why both the third-

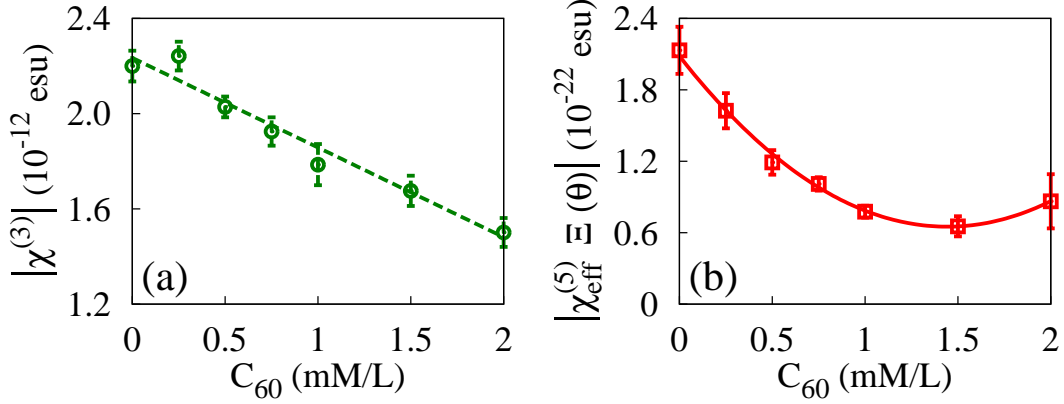


Figure 3.7: Typical experimental data for (a) third-order and (b) fifth-order nonlinear susceptibilities as functions of  $N_{\text{C}_{60}}$ . The lines represent a least-square fit with a function (a) linear and (b) quadratic with respect to  $N_{\text{C}_{60}}$ .

and fifth-order nonlinear susceptibilities in Fig. 3.7 decrease with the increase of  $N_{\text{C}_{60}}$ . It is clear from the graphs that  $|\chi^{(3)}|$  depends on  $N_{\text{C}_{60}}$  linearly, whereas  $|\chi_{\text{eff}}^{(5)}|$  has a quadratic dependence due to cascading. However, as we pointed out earlier in this section, the total measured fifth-order susceptibility should also include the macroscopic (propagational) cascaded contribution,

$$|\chi_{\text{eff}}^{(5)}| = |\chi_{\text{LFC}}^{(5)} + \chi_{\text{macro}}^{(5)}| = |\chi_{\text{dir}}^{(5)} + \chi_{\text{micro}}^{(5)} + \chi_{\text{macro}}^{(5)}|. \quad (3.37)$$

Both microscopic and macroscopic cascaded effects have a quadratic dependence on the atomic density [68], and thus separating the contributions of the two cascaded

effects is not straightforward.

In order to resolve the problem of identification of the microscopic cascaded contribution, we solve the driven wave equation [56],

$$\nabla^2 \tilde{E} - \frac{\epsilon^{(1)}}{c^2} \frac{\partial^2 \tilde{E}}{\partial t^2} = \frac{4\pi}{c^2} \frac{\partial^2 \tilde{P}^{\text{NL}}}{\partial t^2}, \quad (3.38)$$

for the direct and microscopic cascaded contributions to  $|\chi_{\text{eff}}^{(5)}|$ , and, separately, for the macroscopic cascaded contribution. Here  $\tilde{P}^{\text{NL}}(t) = P^{\text{NL}} \exp(-i\omega t) = P_0^{\text{NL}} \exp[i(kr - \omega t)]$  denotes the nonlinear polarization. The same kind of relationship is valid for the electric field amplitude:  $\tilde{E}(t) = E \exp(-i\omega t) = A \exp[i(kr - \omega t)]$ . The total fifth-order nonlinear polarization consists of three contributions, corresponding to the direct and the two cascaded mechanisms:

$$P^{(5)} = P_{\text{dir}}^{(5)} + P_{\text{micro}}^{(5)} + P_{\text{macro}}^{(5)}. \quad (3.39)$$

Here we dropped the temporal dependence, as we are dealing with a degenerate nonlinear effect. Next we will write the separate contributions to the total  $P^{(5)}$  in terms of the electric fields of the interacting waves. After that, we will separately substitute them into Eq. (3.38) and solve it to obtain the corresponding contributions to the electric field amplitude, generated by means of the fifth-order nonlinear process.

In order to illustrate how different contributions to the nonlinear signal are generated, we present a phase matching diagram of our DFWM experiment in Fig. 3.8.

The fundamental electric waves “1” and “2”, propagating at an angle  $2\theta$  with respect

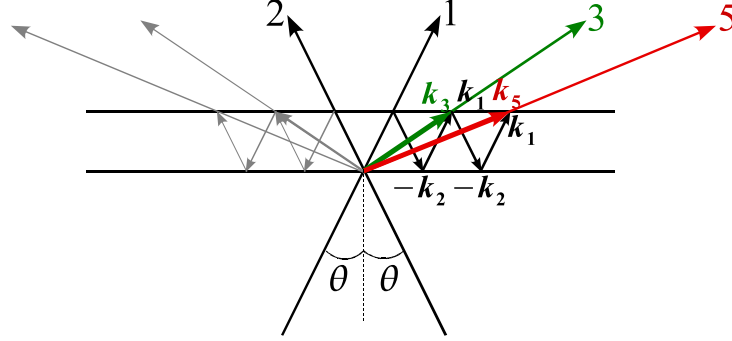


Figure 3.8: Phase matching diagram for generating first and second diffracted order waves (“3” and “5,” respectively). “1” and “2” are the interacting fundamental waves.  $\mathbf{k}_i$  are the  $k$ -vectors of the corresponding waves.

to each other, interact in the nonlinear medium and produce the diffracted waves “3” and “5”. The direct and microscopic cascaded contributions to  $|\chi_{\text{eff}}^{(5)}|$  have the same phase matching condition, as they both are intrinsic properties of the nonlinear response on the molecular or atomic scale. However, it is not possible to achieve full phase matching for these terms, as the nonlinear process is degenerate. That is why it is more informative to present the expression for the wave vector mismatch for the direct and microscopic cascaded contributions to  $|\chi_{\text{eff}}^{(5)}|$ , which is

$$\Delta\mathbf{k}_{5,\text{dir}} = \mathbf{k}_5 - (3\mathbf{k}_1 - 2\mathbf{k}_2). \quad (3.40)$$

Here  $\mathbf{k}_1$  and  $\mathbf{k}_2$  are the wave vectors of the fundamental interacting beams, and  $\mathbf{k}_5$  is the wave vector of the generated fifth-order nonlinear signal (see Fig. 3.8). The corresponding relationship between the nonlinear polarization and the electric fields

is

$$P_{\text{dir}}^{(5)} + P_{\text{micro}}^{(5)} = 10(\chi_{\text{dir}}^{(5)} + \chi_{\text{micro}}^{(5)})E_1^2(E_2^*)^2. \quad (3.41)$$

Solving Eq. (3.38) for the nonlinear polarization given by Eq. (3.41), we find the expression

$$A_{\text{dir}}^{(5)} + A_{\text{micro}}^{(5)} = \frac{5\pi}{3n_0^2\theta^2}(\chi_{\text{dir}}^{(5)} + \chi_{\text{micro}}^{(5)})A_1^3(A_2^*)^2 \left[ \exp\left(i\frac{12\omega n_0}{c}\theta^2 l\right) - 1 \right] \quad (3.42)$$

for the amplitudes of the electric field, corresponding to the direct and microscopic contributions to the fifth-order nonlinear signal.

The macroscopic cascaded term, which is a propagational contribution of the generated third-order nonlinear signal to the fifth-order nonlinear signal, results from a two-step process with the corresponding wave-vector mismatches:

$$\Delta\mathbf{k}_3 = \mathbf{k}_3 - (2\mathbf{k}_1 - \mathbf{k}_2); \quad (3.43a)$$

$$\Delta\mathbf{k}_{5,\text{macro}} = \mathbf{k}_5 - (\mathbf{k}_3 + \mathbf{k}_1 - \mathbf{k}_2). \quad (3.43b)$$

The nonlinear polarization takes form

$$P_{\text{macro}}^{(5)} = 6\chi^{(3)}E_1E_2^*E_3, \quad (3.44)$$

where the electric field  $E_3$ , generated through a  $\chi^{(3)}$  nonlinear interaction, can be

found from Eq. (3.38):

$$E^{(3)} = \frac{3\pi}{2n_0^2\theta^2} \chi^{(3)} A_1^2 A_2^* \left[ \exp\left(i\frac{4\omega n_0}{c}\theta^2 l\right) - 1 \right] \exp(ik_3 r). \quad (3.45)$$

Using Eqs. (3.43b), (3.44), and (3.45), we solve Eq. (3.38) to obtain the relationship

$$A_{\text{macro}}^{(5)} = \frac{35\pi^2}{8n_0^4\theta^4} (\chi^{(3)})^2 A_1^3 (A_2^*)^2 \left\{ \frac{1}{3} \left[ \exp\left(i\frac{12\omega n_0}{c}\theta^2 l\right) - 1 \right] - \frac{1}{2} \left[ \exp\left(i\frac{8\omega n_0}{c}\theta^2 l\right) - 1 \right] \right\} \quad (3.46)$$

for the macroscopic cascaded contribution to the fifth-order nonlinear signal.

Inspecting Eqs. (3.42) and (3.46), one can see that the amplitudes of the electric field of the direct and microscopic cascaded contributions have a different dependence on the angle  $\theta$  and the cell length  $l$ , compared to that of the macroscopic cascaded term. In Fig. 3.9 we plot the absolute values of the angular dependences of Eqs. (3.42) and (3.46), normalized to unity at  $\theta = 0$ , as functions of the angle  $\theta$ . These dependences characterize the efficiencies of the direct, microscopic, and macroscopic cascaded contributions to  $|\chi_{\text{meas}}^{(5)}|$ . The normalized efficiency of the direct and microscopic cascaded contributions is shown with the red solid line, and the efficiency of the macroscopic cascaded contribution is shown with the green dashed line. As the efficiencies are normalized, we cannot extract the information about the relative values of the contributions to the total measured  $|\chi_{\text{eff}}^{(5)}|$ . However, the graphs show approximate positions of the minima and maxima of the efficiencies. It is also

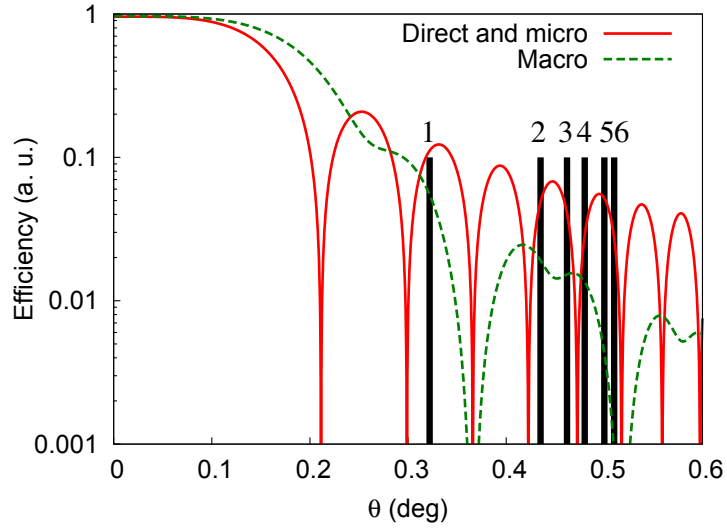


Figure 3.9: Efficiencies of the direct and microscopic cascaded contributions (red solid line) and the macroscopic cascaded contribution (green dashed line) as functions of the half-angle between the interacting beams. Vertical lines show the experimental cases.

important that the efficiency of the macroscopic cascaded process decreases much more rapidly than that of the direct and microscopic cascaded contributions with the increase of the angle between the interacting beams. Measuring the third- and fifth-order nonlinear signals at different angles between the interacting beams, it is possible to discriminate between different contributions to  $|\chi_{\text{eff}}^{(5)}|$ .

The macroscopic cascaded contribution to the total electric field generated by the fifth-order nonlinear process is proportional to  $|\chi^{(3)}|^2$ . Hence, in our experiment  $|\chi_{\text{macro}}^{(5)}| = C_m |\chi^{(3)}|^2$ , where  $C_m$  is some parameter independent of  $N_{\text{C}_{60}}$ . Neglecting the direct and microscopic cascaded contributions to the fifth-order susceptibility of pure  $\text{CS}_2$ , as their values do not change the dependence of  $|\chi_{\text{eff}}^{(5)}|$  on  $N_{\text{C}_{60}}$ , we can find  $C_m$  from  $|\chi_{\text{eff}}^{(5)} \Xi(\theta)| / |\chi^{(3)}|^2$  at  $N_{\text{C}_{60}} = 0$ . Then, multiplying the concentration dependence

of  $|\chi^{(3)}|^2$  by the value of  $C_m$ , we find  $|\chi_{\text{macro}}^{(5)} \Xi(\theta)|$ . We can estimate  $|\chi_{\text{dir}}^{(5)} + \chi_{\text{micro}}^{(5)}|$  from Eq. (3.37), finding that  $|\chi_{\text{eff}}^{(5)}| - |\chi_{\text{macro}}^{(5)}| \leq |\chi_{\text{dir}}^{(5)} + \chi_{\text{micro}}^{(5)}|$ .

We have measured the nonlinear susceptibilities at four values of the angle between the interacting beams (marked in Fig. 3.9 with thick vertical lines with the numbers on top). The results of the measurements are presented in Fig. 3.10 where we plot the values of  $|\chi_{\text{eff}}^{(5)} \Xi(\theta)|$  and  $|\chi_{\text{macro}}^{(5)} \Xi(\theta)|$  as functions of the  $C_{60}$  molar concentration.

For  $\theta \approx 0.3^\circ$ , corresponding to position 1 in Fig. 3.9, we observed no difference between the  $|\chi_{\text{eff}}^{(5)} \Xi(\theta)|$  and  $|\chi_{\text{macro}}^{(5)} \Xi(\theta)|$  [see Fig. 3.10 (a)]. This fact suggests that for this experimental geometry the macroscopic cascaded contribution to  $|\chi_{\text{eff}}^{(5)}|$  is much larger than the direct and microscopic cascaded contributions. We repeated the measurement, increasing the angle to  $0.43^\circ$  (position 2 in Fig. 3.9). The resulting measured values of  $|\chi_{\text{eff}}^{(5)} \Xi(\theta)|$  and  $|\chi_{\text{macro}}^{(5)} \Xi(\theta)|$  are represented in Fig. 3.10 (b). One can see a clear difference between  $|\chi_{\text{eff}}^{(5)} \Xi(\theta)|$  and  $|\chi_{\text{macro}}^{(5)} \Xi(\theta)|$ . This means that, together with the macroscopic cascaded contribution, we observe the presence of other contributions to  $|\chi_{\text{eff}}^{(5)}|$ , which are the direct and microscopic cascaded terms. Taking a careful look at position 2 in Fig. 3.9, one can see that, compared to position 1, the curve characterizing the efficiency of the macroscopic cascaded contribution drops significantly, while the curve describing the efficiency of other two contributions decreases by a much smaller amount. This explains why we were not capable of observing the direct and microscopic cascaded contributions in  $|\chi_{\text{eff}}^{(5)}|$  at position 1,



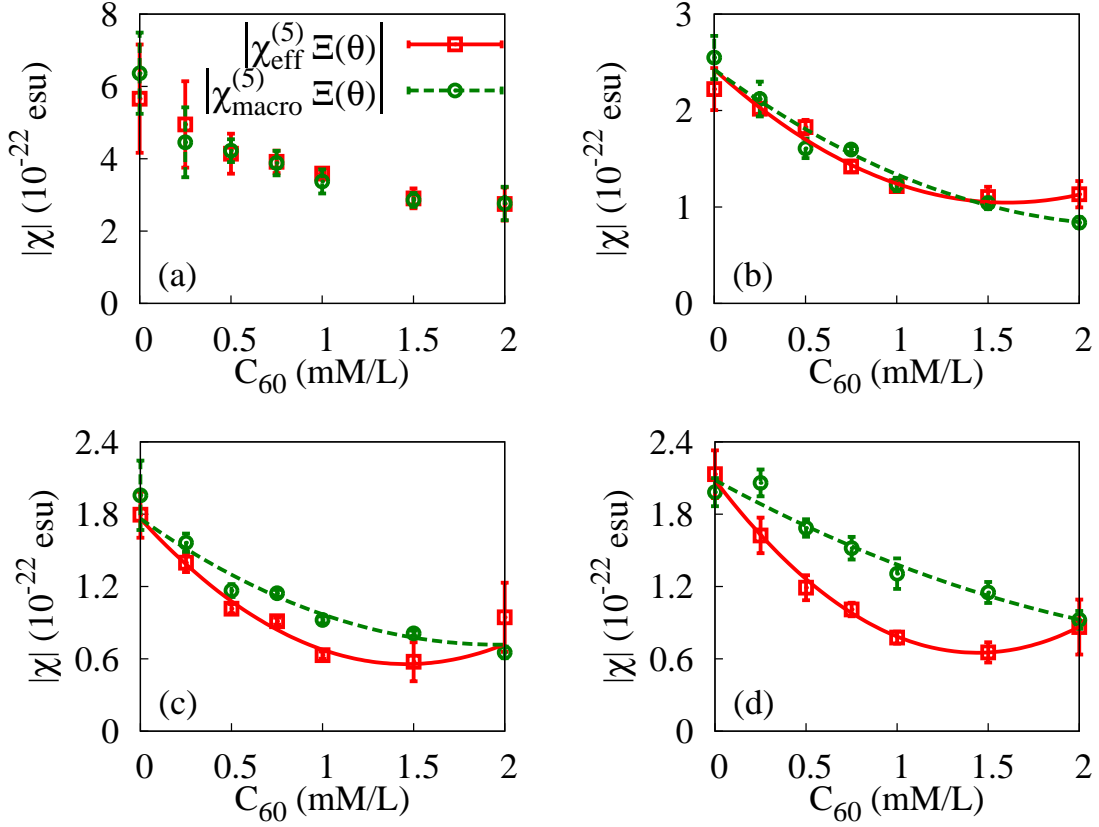


Figure 3.10: Experimentally measured  $|\chi_{\text{eff}}^{(5)} \Xi(\theta)|$  and  $|\chi_{\text{macro}}^{(5)} \Xi(\theta)|$  as functions of  $N_{C_{60}}$ . The measurements are done at the angles between the interacting beams corresponding to (a) position 1 in Fig. 3.9, (b) position 2, (c) position 3, and (d) position 4. The least-square fits to the experimental data are shown with lines.

but see these contributions in the experimental data taken at position 2.

The angles corresponding to positions 3 and 4 in Fig. 3.9 are in close vicinity to the minimum of the macroscopic cascading efficiency curve. The corresponding results are presented in Figs. 3.10 (c) and 3.10 (d). The large difference between  $|\chi_{\text{eff}}^{(5)} \Xi(\theta)|$  and  $|\chi_{\text{macro}}^{(5)} \Xi(\theta)|$  indicates that the macroscopic cascaded contribution is not the dominant contribution to  $|\chi_{\text{eff}}^{(5)}|$ . Observation of positions 3 and 4 in Fig. 3.9 and the

corresponding data in Figs. 3.10 (c) and 3.10 (d) shows a good correlation between the efficiency curves and the experimental data. Indeed, position 3 corresponds to the decrease of the macroscopic cascaded contribution efficiency, and position 4 is very close to the minimum of this curve, while the efficiencies of the direct and macroscopic cascaded contributions is relatively high at these positions. As a result, we observed a large difference between  $|\chi_{\text{eff}}^{(5)} \Xi(\theta)|$  and  $|\chi_{\text{macro}}^{(5)} \Xi(\theta)|$  in Fig. 3.10 (c), and an even larger difference in Fig. 3.10 (d).

We next estimate the values of the three contributions to  $|\chi_{\text{eff}}^{(5)}|$  using the data of Fig. 3.10 (d). The difference of the least-square fits of  $|\chi_{\text{eff}}^{(5)} \Xi(\theta)|$  and  $|\chi_{\text{macro}}^{(5)} \Xi(\theta)|$  contains terms linear and quadratic in  $N_{\text{C}_{60}}$ . They allow us to estimate  $|\chi_{\text{dir}}^{(5)} \Xi(\theta)|$  and  $|\chi_{\text{micro}}^{(5)} \Xi(\theta)|$ , respectively. Using the data for  $N_{\text{C}_{60}} = 2$  mM/L we extracted the following values for the three contributions:  $|\chi_{\text{macro}}^{(5)} \Xi(\theta)| \approx 9.4 \times 10^{-23}$  esu, and  $|\chi_{\text{dir}}^{(5)} \Xi(\theta)| \approx |\chi_{\text{micro}}^{(5)} \Xi(\theta)| \approx 1.2 \times 10^{-22}$  esu. These estimates show that under the conditions of Fig. 3.10 (d) the microscopic cascaded contribution is more significant than the macroscopic cascaded contribution. The microscopic cascaded term can potentially be larger than the direct term by increasing the molar concentration of  $\text{C}_{60}$ , as the former term scales as the square of the concentration. In obtaining the values presented above, we made several approximations. First, we neglected the direct and microscopic cascaded contributions to  $|\chi_{\text{eff}}^{(5)}|$  of pure  $\text{CS}_2$  liquid, because these contributions do not depend on  $N_{\text{C}_{60}}$  and we are concerned only with the shape of the concentration dependence of  $|\chi_{\text{eff}}^{(5)} \Xi(\theta)|$ . In addition, we assumed that all three

contributions to  $|\chi_{\text{eff}}^{(5)}|$  have equal complex phases. This assumption allowed us to estimate the numbers, although there is no fundamental reason to accept the validity of this assumption. Nonetheless, our primary experimental conclusion, that the microscopic cascaded contribution makes a significant contribution to  $|\chi_{\text{eff}}^{(5)}|$  remains valid irrespective of this assumption.

### 3.5 Conclusions

Performing a theoretical analysis of the local-field-corrected nonlinear susceptibilities up to the fifth order of nonlinearity, we uncovered the mechanism of microscopic cascading induced purely by local-field effects. Although this effect had been noticed earlier to occur in third-order nonlinearities, it had been largely overlooked or underestimated in higher-order nonlinear effects. We performed an experimental study that allowed us to estimate the relative value of the microscopic cascaded contribution to the total measured fifth-order nonlinear susceptibility. Our study showed that under certain conditions microscopic cascading can be the dominant effect compared to other contributions to the fifth-order nonlinearity, including the direct process and the macroscopic (propagational) cascaded effect.

Microscopic cascading of the sort we analyze here could play an important role in developing materials with tailored high-order nonlinear response, for instance for applications in high-resolution imaging. In most of the cases, it is easier to employ the macroscopic cascaded process, relying on a lower-order nonlinear susceptibility, to

mimic a higher-order nonlinear effect. However, there can be situations in which this process is unaccessible. For example, for some experimental geometries it may be not possible to obtain an efficient macroscopic cascading, which we have demonstrated with some of our experimental data. Moreover, one can think of an experimental case in which this contribution may be significantly suppressed. That is why it is important to be aware of an intrinsic property of a high-order nonlinearity, the local-field-induced microscopic cascaded contribution, which can be potentially made more powerful than the direct contribution to the high-order nonlinear process. This knowledge should help one to eventually implement the microscopic cascaded effect for achieving a multi-photon absorption, which occurs locally, meaning that the macroscopic cascaded effect is of no use for this phenomenon. Our study presented in this chapter is the first significant step towards achieving an efficient multiphoton absorption relying on the local-field-induced microscopic cascading phenomenon.

Theoretical work reported in Chapter 3 has been recently published in *Physical Review A* [120]. The experimental work reported in Section 3.4 is to be submitted to *Physical Review Letters* [121].

# Chapter 4

## Enhanced Laser Performance of Cholesteric Liquid Crystals Doped with Oligofluorene

### 4.1 Introduction

Cholesteric liquid crystal structures are produced by mixing a nematic liquid crystal with a chiral additive that causes the nematically-ordered molecules to arrange themselves into a helical structure. Dye-doped cholesteric liquid crystals (CLCs) are self-assembling mirrorless distributed-feedback low-threshold laser structures. I have presented a general overview of this kind of laser structures in Section 1.5. Here I report my work in the field of dye-doped CLCs.

We recall the definition of the emission order parameter from Section 1.5, as this concept is the basis of our studies reported in the current chapter. When inserted into a CLC structure, some of organic dyes tend to align with their transition dipole moments along the local director of the CLC. The degree of alignment is characterized by the quantity called “order parameter,” defined according to Eq. (1.32) as

$$S_{\text{em}} = \frac{I_{\parallel} - I_{\perp}}{I_{\parallel} + 2I_{\perp}}, \quad (4.1)$$

where  $I_{\parallel}$  is the fluorescence intensity of the nematic liquid crystal phase doped with the dye, measured for the radiation with the electric field parallel to the director, and  $I_{\perp}$  is the fluorescence intensity for the radiation with the electric field polarized perpendicular to the director. Obviously, the case  $S_{\text{em}} = 1$  corresponds to a perfect alignment of the dye dipole moment along the liquid crystal director, the case  $S_{\text{em}} = -1/2$  corresponds to a perfect alignment of the dye dipole moment perpendicular to the director, and the case  $S_{\text{em}} = 0$  corresponds to an isotropic orientation.

Dyes with high order parameters are believed to have a number of advantages over the dyes with lower order parameters [82, 125]. As most of the molecules’ dipole moments of such dyes are well-aligned with respect to the local director, the threshold for lasing oscillations at low-frequency band edge is lower and the efficiency is higher as compared to the dyes with low order parameter (under the condition that all other characteristics of the dyes are similar). As there is little or no competition between the modes corresponding to the low- and high-frequency band edges for the energy

of the pump radiation, the highly oriented dyes can exhibit highly-stable single-mode oscillations, generating laser radiation only into the mode at the low-frequency edge. As opposed to the highly oriented dyes, the dyes with lower order parameters can yield two lasing peaks, corresponding to the low- and high-frequency band edges. It causes the output radiation to be multi-mode and unstable, as the two frequency modes compete for the pumping energy. Therefore, to achieve better performance in CLC lasers, including lower threshold, higher efficiency, and higher stability, it is important to search for new laser dyes with high order parameters. In reality, one never deals with two identical dyes with the only difference in their optical properties being the value of the emission order parameter. That is why comparing two laser dyes with different order parameters, one has to take into account other optical properties that can influence laser threshold and efficiency, such as the radiative lifetime, quantum yield, and the characteristics of the triplet state typical to all organic dyes. The above characteristics are important if one wants to establish the influence of the order parameter on the laser threshold and efficiency.

A generation of low-threshold mirrorless distributed-feedback self-assembling lasers is being actively developed. Since the work published by Kopp *et al.* [79] brought light into the origin of lasing in CLC, there were a great number of reports on lasing in dye-doped [80,82,84,125–134] and undoped [135] CLCs, as well as in liquid crystal elastomers [136], polymer network devices [137,138], glassy liquid crystals [139], and cholesteric blue phase [140]. Various methods of tunability in such kind of structures

have been addressed by many researchers: electrical [138], temperature [76, 84, 141], mechanical [136], optical [142–145], and through concentration [146] and pitch [147] gradients. Fluorescence behavior in CLC structure has been extensively investigated both theoretically [81, 148, 149] and experimentally [81, 83, 149–152]. For optimization of the laser performance of dye-doped CLCs, their laser characteristics as functions of different parameters, such as the CLC structure thickness and dye concentration [127], temperature [84], excitation rate [129], incident angle and polarization of the pump radiation [133], and the size of the pump spot [134] have been studied.

DCM dye [4-(dicyanomethylene)-2-methyl-6-(4-dimethylaminoethyl)-4H-pyran] is very popular among researchers working in the field of CLC lasers [84, 126–128, 133, 134, 136–138], as this dye can be well incorporated into most of the CLC hosts. On the other hand, DCM has a low order parameter with a value of around 0.4 [82]. To the best of our knowledge, there are very few publications reporting an attempt to find a better dye with higher order parameter for use in CLC lasers [82, 125, 153].

Here we report a new laser dye, oligofluorene OF2, developed in the laboratory of Prof. Shaw Horng Chen [154]. We refer to this dye as OF throughout this chapter. The emission order parameter of OF is 0.60, which is significantly higher than that of DCM. We perform a comparative study of the new oligofluorene dye and the commonly used DCM doped into the same CLC material. For both dyes, we find the optimal concentrations at which their laser performances in CLC are the best. We demonstrate that oligofluorene has a higher laser output and stability than does



DCM.

In Section 4.2, we describe the procedure of preparing the dye-doped CLC samples for our studies. In Section 4.3, we present the description of the experimental setup that we used for laser experiments with CLC structures. In Section 4.4, we discuss frequency mode competition that influences spatial and temporal stability of CLC lasers. Section 4.5 is devoted to our experimental results. We summarize our work in Section 4.6. Sample preparation and their initial quality test was performed by Simon Wei, a graduate student from Prof. Shaw Horng Chen's group. All the laser experiments with dye-doped CLC structures, reported in the current work, were performed by myself.

## 4.2 Sample Preparation

We mixed the nematic liquid crystal (ZLI-2244-000, Merck) with the chiral twisting agent (CB15, Merck) and fluorescent dyes to produce right-handed helical structures. We filled 22- $\mu\text{m}$ -thick glass cells with the dye-doped mixture. The walls of the cells were coated with polyimide and rubbed to align the helical axis perpendicular to the substrates. The cells were prepared in clean room conditions.

The new fluorescent dye OF, an oligomer consisting of a central red-emitting segment end-capped by tetrafluorenes with aliphatic pendants [154], was used as a highly oriented candidate for lasing in CLC in our studies. We prepared six samples with different OF concentrations: 1.00, 1.25, 1.50, 2.00, 2.50, and 3.00 wt. %. For the

purpose of comparison, we prepared the samples doped with 0.50, 0.75, 1.00, 1.25, and 1.50 wt. % of DCM dye. We also prepared a CLC sample with 1.75 wt. % DCM, but the clusters of DCM crystals were observed in this sample under a microscope, which indicates that films with high concentration of DCM encounter phase separation due to limited solubility of DCM in our CLC host. Nevertheless, the ranges of the weight percent of the dyes used in our studies cover the optimal dye concentrations for the best performances of both DCM and OF, and these concentrations for the two dyes are different. Even though the weight percent concentrations of DCM used in our samples are slightly lower than those of OF, the corresponding molar concentrations of DCM are almost an order of magnitude higher. For example, 1.00 wt. % of DCM corresponds to a molar concentration  $2.64 \times 10^{-2}$  M/l, while 1.00 wt. % of OF corresponds to a molar concentration  $2.76 \times 10^{-3}$  M/l. Observation under a microscope showed that the CLC structures had large monodomain areas (the areas without pitch fluctuations). The reflection spectra of the samples revealed an excellent alignment, displaying sharp interference fringes (see Fig. 4.1). The depressed baseline on the short-wavelength side of the stop-band in Fig. 4.1 is because of the dye's light absorption in the visible region that diminishes the observed reflection from the dye-doped CLC film.

The pitch length of a CLC structure depends on the concentrations of both chiral agent and fluorescent dye. We have done a regression calculation to evaluate the helical twisting power of the chiral agent in the absence of a dye. We then calculated

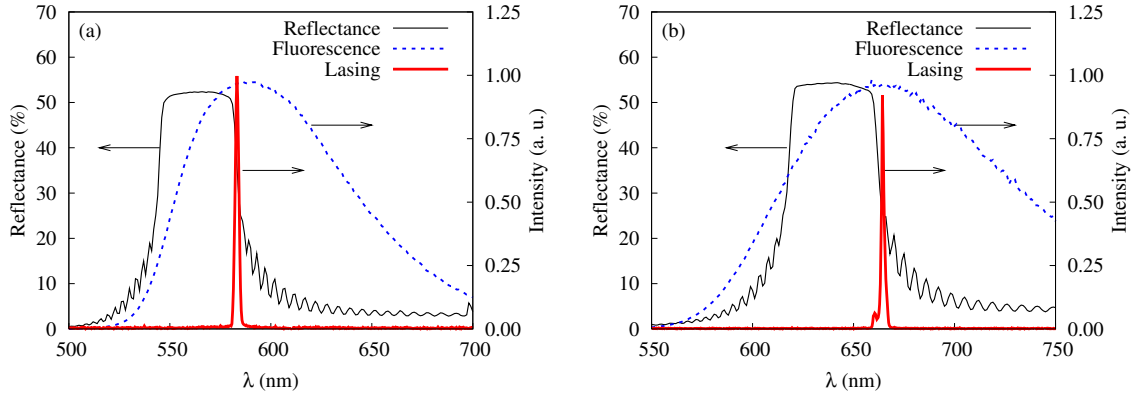


Figure 4.1: The reflectance (thin solid line) and lasing (bold solid line) spectra of (a) 1.25 wt. % DCM-doped CLC sample and (b) 3.00 wt. % OF-doped CLC sample plotted together with the fluorescence spectra of the dyes (dashed line).

how much the presence of 1.00 wt. % of a dye increases the pitch length. Following these calculations, one can match the low-frequency band edge to the dye's maximum fluorescence wavelength with the precision  $\pm 10$  nm. As an example, the reflection and fluorescence spectra of CLCs doped with 1.25 wt. % DCM and 3.00 wt. % OF are presented in Figure 4.1.

In order to evaluate the emission order parameters of DCM and OF dyes, we measured the emission intensities polarized parallel and perpendicular to the director in the nematic liquid crystals doped with the dyes. Then we used Eq. (4.1) to find the values of the emission order parameters to be 0.36 for DCM and 0.60 for OF. These values were obtained for 22- $\mu\text{m}$ -thick samples. Additional measurements have shown that the emission order parameters of 2.5- $\mu\text{m}$ -thick DCM- and OF-doped nematic liquid crystals are 0.41 and 0.70, respectively. We also measured the absorption order parameters of the samples and found that their values for DCM- and OF-

doped nematic liquid crystals are 0.43 and 0.76, respectively, and do not change with the sample thickness. Note that the absorption order parameter can also be defined by Eq. (4.1), if one replaces the fluorescence intensities by corresponding intensity absorption coefficients. The values that are significant for our analysis are the emission order parameters for 22- $\mu\text{m}$ -thick samples (this thickness corresponds to the thickness of our CLC samples for laser measurements).

### 4.3 Experimental Setup

Our experimental setup is depicted in Fig. 4.2. We used a frequency-doubled Nd:YAG laser EKSPLA (Altos), generating 532-nm 35-ps pulses (FWHM) with the 10 Hz repetition rate, as a pump source for the dye-doped CLC structures. The laser produced

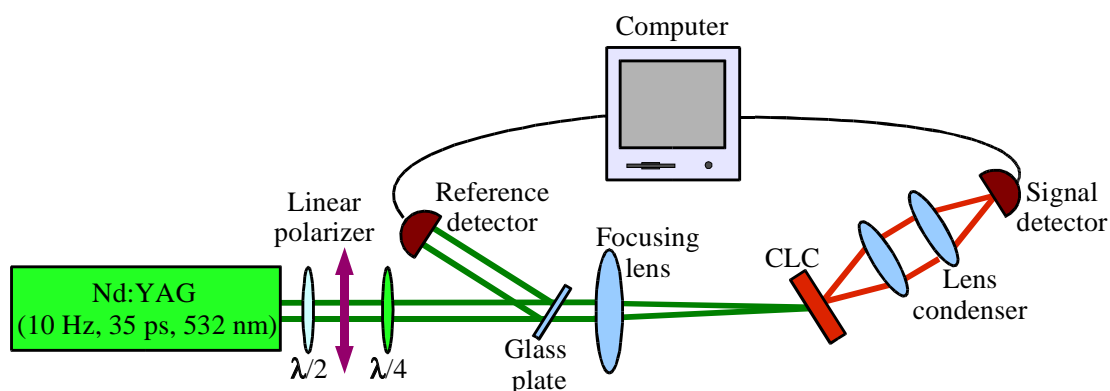


Figure 4.2: Experimental Setup.

nearly Gaussian pulses with diameter 3.3 mm FWHM with respect to the intensity at the position of the focusing lens. A lens of 20 cm was used to focus the laser

beam onto the sample into a spot of 28  $\mu\text{m}$  FWHM. We used a half-wave plate and a linear polarizer to control the pump energy. In order to ensure maximum absorption and minimum scattering loss of the pump radiation, we converted the linearly polarized light exiting the polarizer to left circularly polarized (LCP) light by means of a quarter-wave plate. The LCP pump radiation penetrated inside a right-handed CLC sample and got efficiently absorbed by the dye molecules without losses due to reflection off the CLC structure.

The laser radiation originating from the sample was collected by a lens condenser comprised of two lenses with the focal lengths 5 cm each. The collected laser radiation was sent to an energy meter or Ocean Optics spectrometer USB-2000 with 1 nm resolution. The spectrometer was used to record the laser spectra of the samples. A sample was mounted on a 3D translation stage (not shown in Fig. 4.2) to provide fine adjustment of focusing and optimization of alignment.

For measuring the energy of the CLC laser radiation a reference-signal setup configuration was used. We reflected 10 % of the pump beam by a microscopic glass plate to the reference energy meter, while the signal energy meter was used to measure the energy of the CLC laser output. The energy meters were connected to a computer. Using software, we set a range of acceptable values of the reference energy for each data point. This way we eliminated the influence of shot-to-shot fluctuations in the pump laser and significantly increased signal-to-noise ratio in our data.

## 4.4 Stability and Frequency Mode Competition

Using an electron-multiplied cooled EM-CCD camera (Andor Technologies), we recorded the intensity distributions of DCM- and OF-doped CLC laser outputs (see Fig. 4.3). We applied the pump fluence approximately twice the threshold in order to record the intensity distributions. It can be seen from the figure that DCM has a highly

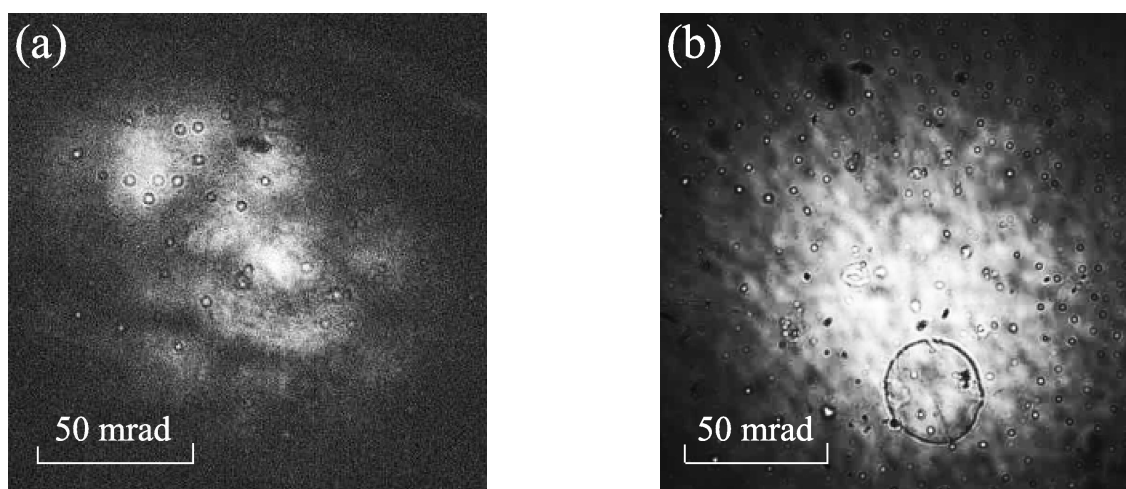


Figure 4.3: Intensity distribution of the laser output measured using a CCD camera in (a) 1.00 wt. % DCM-doped CLC and (b) 2.00 wt. % OF-doped CLC. The dark ring at the bottom of the picture is a camera artifact.

non-uniform intensity distribution in its output, while OF displays a much more uniform intensity distribution. The spatial pattern of DCM-doped CLC was found to change significantly in time, while that of OF remained stable.

We attribute the highly unstable behavior of DCM-doped CLC to the strong degree of competition between the low- and high-energy photonic band edge modes. The nature of the competition between the frequency modes is as follows. The molecules of a dye with an order parameter  $S_{em} > 0$  tend to align with their transition dipole

moments along the local director of a CLC structure. However, there are nonzero components of the dye molecules' dipole moments perpendicular to the local director, as  $S_{\text{em}}$  is typically less than 1. This implies that the dye's emission contributes to both frequency modes of the CLC situated at the low- and high-energy band edges. The two band edge frequency modes compete with each other for the use of the pump energy. When the CLC structure doped with the dye is pumped at the wavelength of the dye's absorption, laser generation is most likely to occur at the low-energy band edge frequency mode, as most of the dye's emission contributes to that mode. At low pump energies the low-energy band edge mode suppresses the high-energy edge mode, as the preferred orientation of the dye's dipole moments is along the local direction. As the pump energy grows higher, the competition between the low- and high-energy band edge frequency modes for the use of the pump energy becomes stronger. At a certain level of the pump the high-energy edge mode can reach its threshold and the resulting output spectrum will contain two peaks: a stronger peak corresponding to the low-energy edge mode, and a weaker peak of the high-energy edge mode.

Typical lasing spectra of our samples are shown in Fig. 4.1, together with the reflectance of the CLC structures and fluorescence spectra of the dyes. Both DCM- and OF-doped CLCs displayed lasing at the low-energy band edge. As the order parameter of DCM is much smaller than that of OF, it is supposed to be relatively easy to observe the second peak in the lasing spectrum of DCM, corresponding to the high-energy band edge frequency mode [82, 125, 153]. Nevertheless, the second

peak in the laser outputs of DCM and OF failed to appear, as the lasing degradation and damage of our CLC host occurred with the increase of the pump fluence before the high-frequency mode reached its threshold. However, DCM would experience a stronger competition between the low- and high-energy band edge frequency modes, regardless whether its lasing spectrum does or does not contain the second peak. We believe that this competition between the band edge frequency modes caused the temporal and spatial instabilities that we observed in DCM-doped CLC laser output.

## 4.5 Lasing Output

We measured the lasing output characteristics of OF- and DCM-doped CLC samples in two different regimes. The first regime corresponds to the sample position precisely at the focal point of the lens used to focus the pump radiation. In this regime we observed laser output of a sample in the form of a single spot corresponding to the single *transverse* fundamental spatial mode (see Fig. 4.4(a)). Due to this reason, we call this regime “transverse single-mode.” We positioned the sample precisely to the focal point of the lens by translating it laterally on the micrometer stage while measuring the laser output at a very low pump level (slightly higher than the threshold). This way, we optimized for the maximum output energy, which helped us to ensure that the sample is precisely at the focus.

In the second regime we defocused the pump radiation by longitudinally translating the sample 14 mm away from the focal point of the lens. In this case, we



observed a ring pattern at the sample's output, corresponding to generation of several transverse spatial modes (see Fig. 4.4(b)). We call the second regime "transverse multi-mode." The pump spot diameters in transverse single-mode and multi-mode regimes were 28 and 230  $\mu\text{m}$  FWHM, respectively. We have done a comparative study of the laser performances of DCM- and OF-doped CLCs in both regimes.

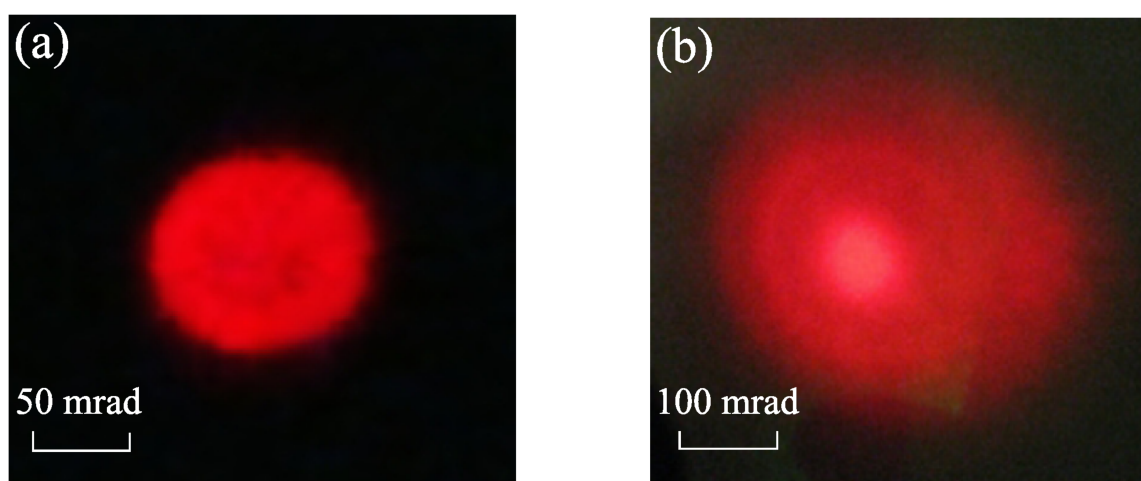


Figure 4.4: (a) A photograph of a single transverse mode observed in the lasing output of the 2.00 wt. % OF-doped CLC in transverse single-mode regime. (b) A photograph of a ring pattern observed in the lasing output of the 2.00 wt. % OF-doped CLC in transverse multi-mode regime.

### 4.5.1 Transverse single-mode regime

Laser output characteristics in transverse single-mode regime, in which the samples were positioned precisely at the focal point of the lens focusing the pump radiation, are presented in Fig. 4.5. The way we obtained the data points in Fig. 4.5 is by averaging over 30 measurements for each pump energy setting and evaluating the standard

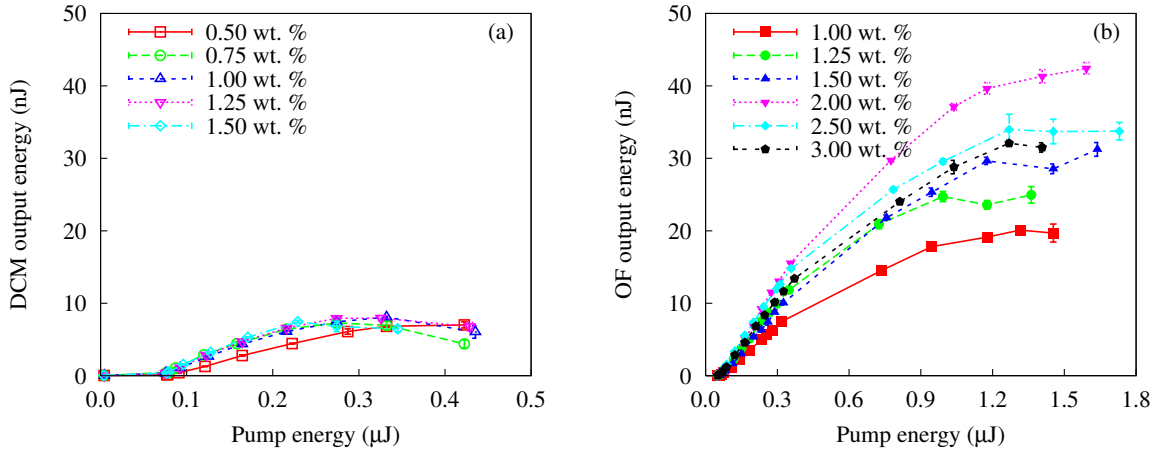


Figure 4.5: Laser output energy plotted as a function of the incident pump energy of (a) DCM- and (b) OF-doped CLC samples in transverse single-mode regime.

deviation. Different curves correspond to different concentrations of DCM and OF, as reflected in the legends. The ranges of the pump energies, shown on the  $X$ -axes of the graphs, are different, as the output characteristics of DCM-doped CLCs saturated much more rapidly with increasing the pump energy. The  $Y$ -axes of the graphs, representing the output energy of the samples, have the same scale, and it is obvious that OF produces 5 times more output energy in transverse single-mode regime, as compared to DCM. The output vs. pump energy characteristics in transverse single-mode regime were reproducible within 10%. The standard deviation of the measured output energy was less than 10%. The lasing threshold fluences of all DCM and OF samples are approximately the same and are around  $7 \text{ mJ/cm}^2$ . The slope efficiencies derived from the linear parts of the output characteristics as the ratios of the output energy changes to the changes in the incident pump energy are presented in Fig. 4.6. It is clear from Figs. 4.5 and 4.6 that there is an optimal concentration for each laser

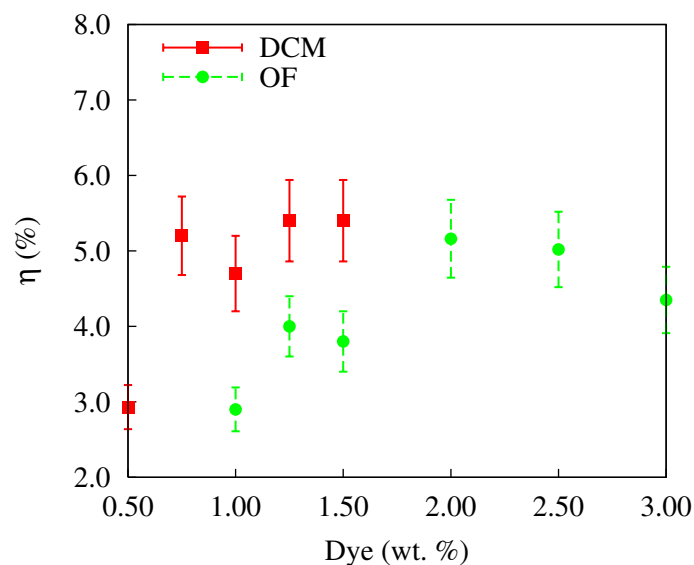


Figure 4.6: Slope efficiency of the laser output of DCM- (squares) and OF-doped CLC samples (circles) as a function of the dye weight percent in transverse single-mode regime.

dye at which the CLC laser demonstrates the top performance, yielding the highest output energy and slope efficiency. At the dyes concentrations lower than the optima, there is not enough dye molecules in CLC to produce much energy and efficiency. At high dye concentrations the pump radiation gets absorbed within several microns from the front surface of the sample and cannot get inside the CLC structure far enough for the dye molecules all through the length of the CLC to be excited. Besides, in case of high dye concentrations the dye molecules are spaced so closely that the parasitic reabsorption and triplet quenching effects characteristic to all organic dyes [155] get much stronger. The maximum slope efficiency achievable in transverse single-mode regime was around 5% for both DCM and OF dyes. It can be seen from Fig. 4.6 that the best laser performance was achieved with 1.25 wt. % DCM and 2.00 wt. % OF

samples. The slope efficiency data were reproducible and accurate within 10%, which is reflected in the size of the error bars in Fig. 4.6. Within this study, we report the slope efficiency values based on the measurement of the CLC laser output collected only in one direction.

### 4.5.2 Transverse multi-mode regime

Laser output characteristics measured in transverse multi-mode regime, corresponding to the position of the samples 14 mm away from the focal spot of the lens, are shown in Fig. 4.7. The reproducibility of the data obtained in transverse multi-mode

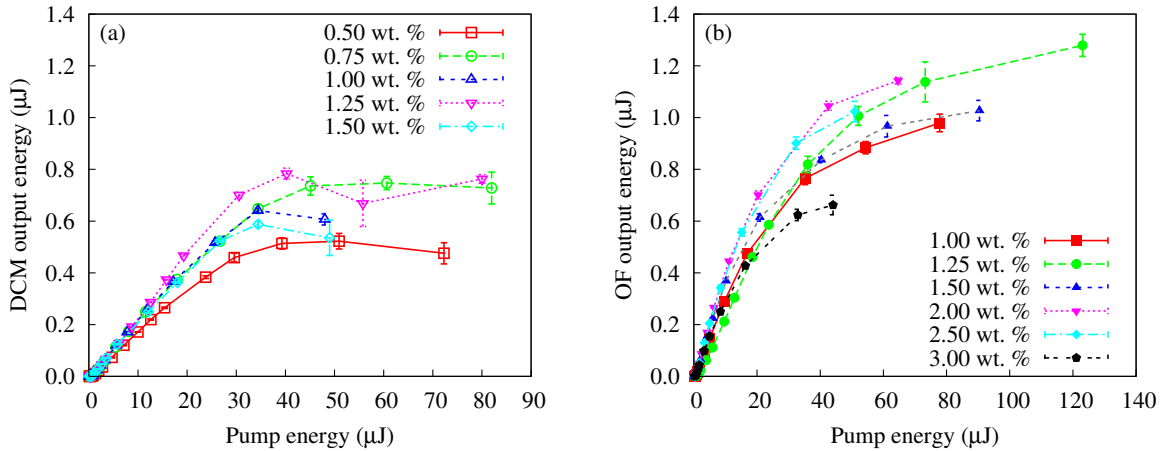


Figure 4.7: Laser output energy plotted as a function of the incident pump energy of (a) DCM- and (b) OF-doped CLC samples in transverse multi-mode regime.

regime is within 20%, while the standard deviation of the output energy is around 10%. The maximum output energy of OF in transverse multi-mode regime was measured to be 1.6 times greater than that of DCM. The lasing threshold fluences of all OF and DCM samples were around  $0.7 \text{ mJ/cm}^2$ , which is an order of magnitude lower

than that in transverse single-mode regime. The reason for the higher threshold in transverse single-mode regime can be that the pump is focused so tightly that the radiation with such a small beam diameter cannot efficiently pump the transverse fundamental spatial mode. This makes it more difficult to achieve the threshold on that mode, and makes it impossible for higher-order spatial modes to appear at the output of the CLC laser. The latter is good when it is crucial to obtain a single transverse fundamental spatial mode in the CLC output.

The slope efficiencies of the samples in transverse multi-mode regime are shown in Fig. 4.8. Unlike in the transverse single-mode regime, where the slope efficiencies

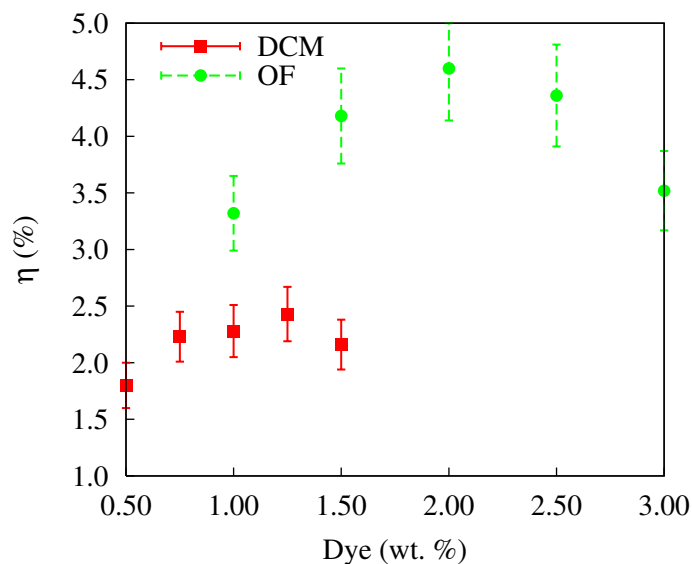


Figure 4.8: Slope efficiency of the laser output of DCM- (squares) and OF-doped CLC samples (circles) as a function of the dye weight percent in transverse multi-mode regime.

of DCM and OF were comparable, in the transverse multi-mode regime OF displayed almost twice larger maximum slope efficiency. A possible explanation to this is as

follows. In the transverse multi-mode regime there are many spatial modes in the laser output. They all contribute to the total laser output energy, and, therefore, influence the overall slope efficiencies of the output characteristics. As it has been shown in the transverse single-mode regime, the saturation of the output energy with the increase of the pump energy occurs much more rapidly in DCM- than in OF-doped CLCs. In the transverse multi-mode regime, there are many modes contributing to the total output of DCM, but each of those modes saturates more rapidly than a similar mode of an OF-doped CLC. That is why the overall slope efficiency of DCM-doped CLCs is significantly lower in the transverse multi-mode regime.

Based on the above picture, we can also explain the reason why in the transverse single-mode regime OF-doped CLCs produce 5 times higher maximum output energy as compared to DCM-doped CLCs, while in the transverse multi-mode regime they produce only 1.6 times higher maximum output energy. In the transverse single-mode regime we measure the output only of the fundamental spatial mode. That is why the maximum output energies of the dye-doped CLCs are limited by the saturation of that mode. In the multimode regime, the pump spot is an order of magnitude larger, and it efficiently pumps several spatial modes. As the intensity distribution at the pump spot on the sample is Gaussian, the first mode to lase would be the fundamental mode. The other modes switch on as we increase the pump energy, so that the intensity at the edge of the pump spot is high enough for them to meet the threshold conditions. As we increase the pump energy, more and more spatial

modes appear in the laser output, and DCM-doped CLCs saturate not as rapidly as they would if there were only one fundamental mode in the output. That is why the difference in the maximum output energy between DCM- and OF-doped CLCs is smaller in the transverse multi-mode regime.

Comparing the laser performances of DCM- and OF-doped CLC samples, we found that the laser thresholds are similar for all samples. All DCM- and OF-doped CLC display the thresholds  $7 \text{ mJ/cm}^2$  and  $0.7 \text{ mJ/cm}^2$  in the transverse single-mode and multi-mode regimes, respectively. The slope efficiencies of DCM- and OF-doped samples are similar in the transverse single-mode regime. In the transverse multi-mode regime OF-doped samples display the slope efficiency almost twice higher than that of DCM-doped samples. The maximum laser output obtained with OF-doped CLCs was found to be 5 times greater than that obtained with DCM-doped CLCs in the transverse single-mode regime, and 1.6 times greater in multi-mode regime. In addition, the spectral purity and the temporal and spatial stability of the laser output of OF-doped CLCs is much higher than that of DCM-doped CLCs. Based on the above results, one can conclude that OF is a better choice for lasing in CLC structures.

### 4.5.3 Laser Output Degradation Issues in CLCs

Working with dye-doped CLC in liquid phase requires extra care. Even a slightest mechanical stress that one accidentally applies to a CLC sample can cause the loss

of alignment, appearance of multi-domain regions, and change in the pitch and the lasing wavelength. Besides, as the host is in liquid state, the period of the structure is sensitive to the heating from the pump radiation, and degradation of the CLC laser output, caused by the heating, can occur. Even though glassy liquid crystal hosts are more robust, it is the CLCs in liquid state that allow to achieve tunability of the laser wavelength. Therefore, it is important to investigate CLC lasers with both liquid and glassy hosts. The experiments with glassy liquid crystal hosts doped with OF dye have been recently performed in Prof. Chen's group [156].

We observed a difference in the behavior of DCM- and OF-doped CLC lasers. For example, in the transverse single-mode regime at the pump energies in the range between 200 and 500 nJ, we observed a significant degradation of laser output with time in DCM-doped CLCs, while OF-doped CLCs displayed stable lasing in this range of pump energies.

## 4.6 Conclusions

We have performed a detailed comparative study of the laser output characteristics of CLC structures doped with a commonly used laser dye, DCM, with the emission order parameter 0.36 and with a new laser dye, OF, with the order parameter 0.6. The study of the laser spectra showed that only a single laser peak, corresponding to the low-energy band edge frequency mode, can be observed in the output of all DCM and OF samples. We expected to observe a second peak, corresponding to



the high-energy band edge mode in the output spectra of DCM-doped CLCs, but it appears that the threshold for the second frequency mode is higher than the damage threshold of our CLC host.

OF-doped CLCs displayed a much higher temporal and spatial stability in the output radiation. We attribute this to the higher value of OF's order parameter that prevents strong competition between the high- and low-energy edge frequency modes. Strong competition between the modes, taking place in case of a dye with a low order parameter, degrades the laser performance, creating temporal and spatial instabilities, which we observed with DCM-doped CLCs.

We measured the laser output characteristics of DCM- and OF-doped CLCs in two different regimes corresponding to generating a single fundamental spatial mode and a multi-mode ring pattern. This study itself is interesting, as, to the best of our knowledge, spatial transverse single-mode and multi-mode regimes have not been discussed in CLC structures before. The value of the transverse single-mode regime is that one can obtain a single fundamental spatial mode at low pump energy. Transverse multi-mode regime is interesting because it yields much higher output energy. The way one can control the number of the spatial modes appearing in the output is through changing the size of the pump spot in the sample. We found that the laser thresholds and the slope efficiencies of DCM- and OF-doped CLCs are similar in the transverse single-mode regime, but OF-doped CLCs produce maximum output energy 5 times greater. The laser thresholds of the samples doped with both dyes in

the transverse multi-mode regime are similar, but the slope efficiency of the OF-doped samples is almost twice higher.

The results of our study invite the conclusion that OF is an excellent laser dye for use in CLC structures, demonstrating a better laser performance in many aspects than that of the popular dye DCM.

This work has been published in the Journal of the Optical Society of America B [157]. New experimental work on characterization of OF-doped robust glassy CLCs have been recently performed in Prof. Shaw Horng Chen's group [156]. Several other experiments related to dye-doped liquid and glassy CLC structures are currently in progress.

# Chapter 5

## Optical Activity in Diffraction from a Planar Array of Achiral Nanoparticles

### 5.1 Introduction

Chiral objects occur in two mirror-image forms (enantiomers) that cannot be superimposed with each other by proper rotations [158]. Chirality is usually associated with molecular structure and leads to optical-activity effects, which arise from different interaction of chiral molecules with left- and right-hand circularly-polarized light [159, 160]. Conventional optical-activity effects, such as circular dichroism and polarization (azimuth) rotation, arise from “molecular” chirality and occur in isotropic

bulk liquids (*e. g.*, sugar solutions) and molecular crystals. Because of their molecular origin, these effects are proportional to the density of chiral molecules and build up as light traverses the chiral medium. Optical-activity effects can also arise from a chiral arrangement of achiral objects, *e. g.*, the arrangement of silicon and oxygen atoms in a unit cell of crystalline quartz. Such “structural” chirality relies on the stability of the atomic arrangement and vanishes when the crystal is melted or dissolved. Both molecular and structural chirality thus arise from the three-dimensional (3D) nature of the material. It is also possible that materials with neither molecular nor structural chirality give rise to optical-activity effects. This is the case if an experiment is performed where the setup itself is chiral, *i. e.*, it is defined by three non-coplanar vectors with a given handedness. Such effects are known in light scattering from anisotropic molecules or angular-momentum-aligned atoms and in nonlinear optics [161–165]. Note also that molecular chirality implies structural chirality, and structural chirality implies chirality of the experimental setup. Therefore, separation of the three different mechanisms may be difficult.

Recent nanofabrication techniques have made it possible to prepare samples with so-called planar or 2D chirality [85, 166]. Such samples are usually 2D arrays with a sub-wavelength period and consist of nanoparticles that cannot be brought into congruence with their mirror image by in-plane rotations or translations. The samples, therefore, possess a sense of twist, which is different when viewed from the front and back sides of the sample. This peculiarity has invoked controversies of possible

violation of time-reversal symmetry and nonreciprocity of the light-matter interaction in 2D chiral media [89, 96, 97]. However, it is now well established that planar arrays of nanoparticles lead to optical activity similar to that of conventional chiral media [90], because of the front-back asymmetry brought about by the substrate [90] or other vertical structure [167], which effectively turns a 2D sample into a 3D sample. However, it is now well-established that planar arrays of nanoparticles lead to optical activity similar to that of conventional chiral media [90]. The reason is that a real 2D chiral sample can be seen as a 3D sample because of the substrate [90] or other vertical structure [167]. As a consequence, conventional circular dichroism and polarization rotation in transmission are forbidden in strictly 2D samples, such as free standing nanogratings [90].

In contrast to the conventional optical activity, which is thus forbidden, polarization-sensitive diffraction from 2D chiral samples can occur. Different diffraction patterns for left- and right-hand circularly-polarized light have been observed for planar square gratings consisting of particles with four-fold rotation axis and no reflection symmetry [97]. Following the above classification for bulk media, this result can be seen to arise from 2D molecular chirality because of the particular sense of twist of the individual 2D nanoparticles. Similarly, one can also introduce 2D structural chirality, when the sense of twist of the 2D grating arises from the mutual arrangement of achiral nanoparticles. An attempt has been made to separate contributions from the molecular and structural 2D chirality to the polarization effects in diffraction

experiments by varying the direction of polarization of incident light [85]. However, no reference sample with pure structural chirality was used. Such a sample would have to consist of achiral nanoparticles arranged in a chiral grating with no mirror symmetry.

In this study, we report the observation of polarization changes in diffraction from a planar grating that consists of achiral crosses whose mutual orientations make the overall sample 2D chiral. This is, to the best of our knowledge, the first systematic study of diffraction from planar structures with pure structural chirality. We find that the polarization changes from such samples are significant, in fact, comparable to those observed from reference samples where the individual particles are chiral. This is surprising, as the origin of chirality in the two samples is different, and the interparticle coupling would be crucial for observing optical activity in transmission experiments with structurally chiral samples. It is therefore quite natural to expect that the effects may be *quantitatively* different for samples with chirality of different origins; we show, however, that in the diffraction experiments this is not the case. Our results therefore suggest that the two types of sample chirality cannot be separated in diffraction experiments. Our conclusion is further supported by a simple model which describes the polarization of the diffracted wave in terms of light scattering from a strictly 2D array of nanoparticles. In this model, the grating only enhances scattering into a given diffraction order through constructive interference, as the model involves no interparticle coupling.

## 5.2 Experiment

Our sample, fabricated utilizing electron-beam lithography, contains different patterns of nanoparticles on a fused silica substrate. In the direction perpendicular to the sample plane, the particles consist of a 3 nm Cr adhesion layer and 30 nm of Au. The entire structure is coated by 20 nm protective SiO<sub>2</sub> layer. There are eight different nanoparticle patterns (Fig. 5.1). Patterns 1 and 2 are achiral: pattern 1 is a square

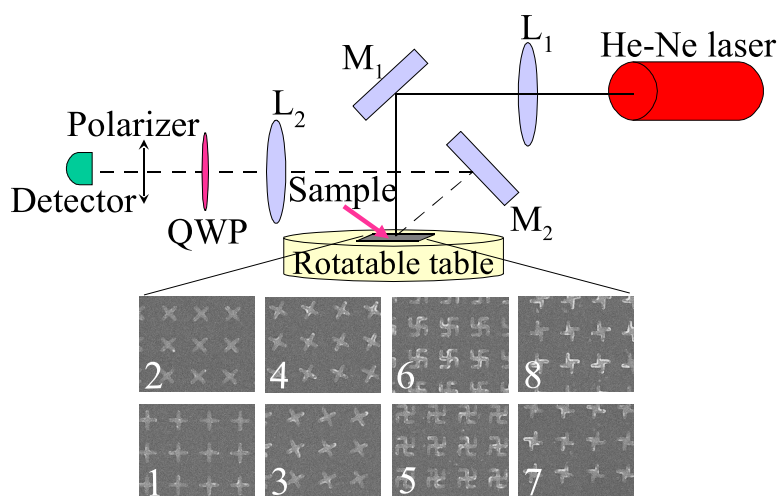


Figure 5.1: Experimental setup and sample layout.

lattice of achiral crosses with the legs oriented along the lattice axes, while pattern 2 is a lattice of crosses tilted at 45° with respect to the lattice axes. Patterns 3 and 4 consist of achiral crosses tilted at +27.5° and −27.5° with respect to the lattice axes, respectively. The ±27.5° tilt results in pure structural chirality of the patterns, as the individual particles are achiral. Patterns 5, 6, 7, and 8 contain chiral gammadions and propellers, and, therefore, possess molecular chirality. The chiral patterns in each

pair (3, 4), (5, 6), and (7, 8) are enantiomeric forms (mirror images) of each other. The period in all gratings is 800 nm; each pattern is a 1 mm  $\times$  1 mm square.

We illuminated the sample with a linearly polarized light from a 633-nm He-Ne laser at normal incidence (see Fig. 5.1). The polarization state of the incident light was controlled by a half-wave plate and a linear polarizer (not shown in the figure). We measured the polarization rotation and ellipticity of the first-order diffracted beams from all eight patterns for  $p$ - and  $s$ -polarized incident light. (We call the incident light  $p$ -polarized if its electric field vector lies in the plane perpendicular to the sample and containing the diffracted beam, and  $s$ -polarized if the electric field is perpendicular to this plane.) Due to the astigmatism of the electron beam writing, the samples can exhibit some anisotropy that affects the polarization state of the diffracted light. To remove the effects of the residual anisotropy of the structures, we analyzed the polarization states of four equivalent first-order diffracted beams corresponding to the four equivalent azimuthal orientations of the samples, and averaged the results. The spread in the data collected from the four equivalent first-order diffracted beams does not exceed  $3^\circ$  for patterns 1, 5, 6, 7, and 8, but is about  $10^\circ$  for patterns 2, 3, and 4, as the lattice axes for the latter patterns have a nonzero angle with respect to the directions of the electron beam writing. We repeated each measurement three times and found that the random errors in our measurements are smaller than the size of the datapoint in the graphs. However, the precision of the polarizer and the quarter-wave plate rotation is within  $1^\circ$ , which introduces some uncertainty into establishing



the “zero level” of ellipticity and polarization rotation. This zero level is set by the achiral patterns 1 and 2 and we have removed this offset from the other results.

### 5.3 Experimental Data

The polarization rotation and ellipticity of the diffracted beam are presented in Fig. 5.2. The achiral patterns 1 and 2 do not change the polarization state of the

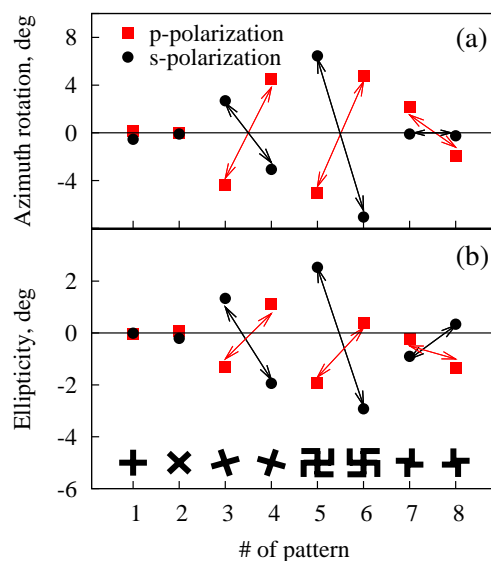


Figure 5.2: (a) Polarization azimuth rotation and (b) ellipticity of light in diffraction from the planar structures. Data for  $p$ - and  $s$ -polarized incident light are shown with squares and circles, respectively. The results for the two enantiomerically opposite forms are connected by the arrows. The offset of the “zero level” set by the achiral patterns 1 and 2 is within  $1^\circ$ . It has been shifted to coincide with the zero level of the graphs for both polarization rotation and ellipticity.

diffracted light. The chiral patterns 3–8, on the other hand, display clear deviations of the polarization rotation and ellipticity with respect to the zero level established by the patterns 1 and 2. The patterns that are enantiomeric forms of each other

demonstrate polarization effects equal in magnitude and opposite in sign, which is a manifestation of chirality. The polarization effects reverse sign as the linear polarization of the incident light changes from  $p$ - to  $s$ -state. The strongest polarization changes are observed from the pair of patterns (5, 6), which contain chiral gam-madions. The effect observed from the pair of patterns (3, 4) with pure structural chirality, however, is almost as large. Patterns 7 and 8, consisting of chiral propellers, on the other hand, display very weak polarization changes.

## 5.4 Wire Model

The origin of the polarization effects in patterns 3 and 4 possessing pure structural chirality can be explained by a simple “wire model” (inspired by [85]) where the only possible source of chirality is the orientation of the achiral particles with respect to the square lattice. Let us assume that a plane monochromatic wave with the frequency  $\omega$  is incident on a patterned surface with the period  $a$  (for convenience, we do not show the frequency dependence). We consider the linear response of the surface current density  $\mathbf{j}(\rho)$  to the electric field  $\mathbf{E}^i(\rho)$  of the incident electromagnetic wave, where  $\rho$  is a 2D position vector in the plane of the sample surface:

$$j_i(\rho) = \kappa_{ij}(\rho) E_j^i(\rho). \quad (5.1)$$

We can treat the linear surface response tensor  $\vec{\kappa}(\rho)$  as a  $2 \times 2$  matrix, as  $\mathbf{E}^i(\rho)$  lies in the surface plane in the case of normal incidence. In order to find the electric field in the far zone that is emitted by the current distribution  $\mathbf{j}(\rho)$ , we need to represent  $\mathbf{j}(\rho)$  as a spatial Fourier series. Since  $\mathbf{E}^i(\rho)$  is homogeneous in the surface plane, the problem reduces to a spatial Fourier representation of  $\vec{\kappa}(\rho)$ . As the sample is periodic in both main directions of the square lattice (which we call  $X$  and  $Y$  directions), we can write it down as

$$\kappa_{ij}(\rho) = \sum_{\alpha\beta} \tilde{\kappa}_{ij}^{(\alpha,\beta)} \exp \left[ i \frac{2\pi}{a} (\alpha\rho_x + \beta\rho_y) \right], \quad (5.2)$$

where

$$\tilde{\kappa}_{ij}^{(\alpha,\beta)} = \frac{1}{S} \int_S \kappa_{ij}(\rho) \exp \left[ -i \frac{2\pi}{a} (\alpha\rho_x + \beta\rho_y) \right] d\rho, \quad (5.3)$$

$S$  is the area of the unit cell. The zeroth order of the expansion (5.3),  $\tilde{\kappa}_{ij}^{(0,0)} \equiv \bar{\kappa}_{ij}$ , describes the reflected wave. The term with  $\tilde{\kappa}_{ij}^{(1,0)}$  describes the first order of diffraction in the direction of positive  $x$ , *i. e.*, one of the four first-order diffraction maxima in the reflection geometry.

We model each “molecule” with a cross made of two wires of the length  $2d$  each; the cross is rotated counter-clockwise by an angle  $\alpha$  with respect to the  $XY$  coordinate system of the square lattice (see Fig. 5.3(a)). As evident from standard diffraction theory, the waves emitted by different unit cells are coherently added only in the directions of the diffraction maxima determined by the lattice period  $a$ . We

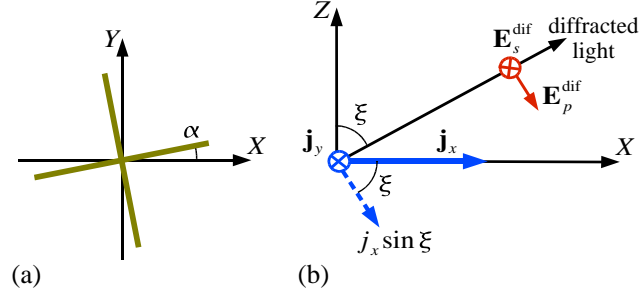


Figure 5.3: Scattering from a tilted cross. (a) Top view of the cross. (b) Side view of the scattering geometry.

consider the scattering of light from the pattern in the direction of the first diffraction maximum  $(1, 0)$ , which lies in the  $XZ$ -plane and has the angle of diffraction  $\xi$  (see Fig. 5.3(b)). The electric field  $\mathbf{E}^{\text{dif}}$  in the far zone in that direction is determined by the respective spatial Fourier harmonic of  $\mathbf{j}(\rho)$ , which can be written as

$$\tilde{j}_m^{(1,0)} = \tilde{\kappa}_{mn}^{(1,0)} E_n^i. \quad (5.4)$$

A straightforward calculation yields the result

$$\tilde{\kappa}^{(1,0)} = \sigma \frac{a}{\pi} \begin{bmatrix} \beta \cos \alpha + \gamma \sin \alpha & \beta \sin \alpha - \gamma \cos \alpha \\ \beta \sin \alpha - \gamma \cos \alpha & \beta \frac{\sin^2 \alpha}{\cos \alpha} + \gamma \frac{\cos^2 \alpha}{\sin \alpha} \end{bmatrix}. \quad (5.5)$$

Here  $\sigma$  is the specific linear conductivity of the wires,  $\beta = \sin[(\pi d/a) \cos \alpha]$ , and  $\gamma = \sin[(\pi d/a) \sin \alpha]$ . The  $s$ -component of diffracted light,  $\mathbf{E}_s^{\text{dif}}$ , is collinear with the  $Y$  axis, while its  $p$ -component,  $\mathbf{E}_p^{\text{dif}}$ , makes the angle  $\xi$  with the  $X$  axis (see Fig. 5.3). Therefore, we can find the components  $\mathbf{E}_s^{\text{dif}}$  and  $\mathbf{E}_p^{\text{dif}}$  from  $\mathbf{E}_s^{\text{dif}} = C \tilde{j}_y^{(1,0)}$

and  $\mathbf{E}_p^{\text{dif}} = C \tilde{j}_x^{(1,0)} \sin \xi$ , where  $C$  is a constant that is identical for both  $\mathbf{E}_s^{\text{dif}}$  and  $\mathbf{E}_p^{\text{dif}}$ .

These results then directly yield the polarization rotation.

In Fig. 5.4 we show the theoretical polarization rotation of the diffracted electric field as a function of the tilt angle  $\alpha$  of the wire cross with respect to the lattice axes for the  $p$ - and  $s$ -polarized incident light. The graphs are plotted for the leg length

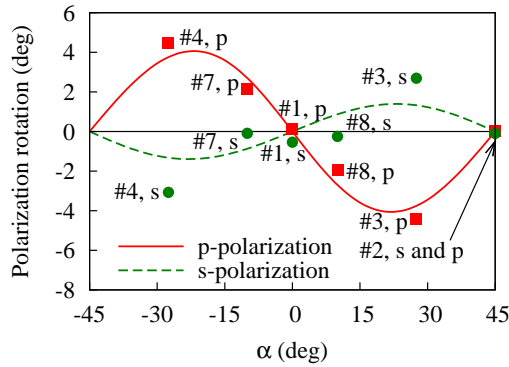


Figure 5.4: Polarization azimuth rotation of the diffracted light as a function of the tilt angle  $\alpha$  of the crosses with respect to the lattice axes, calculated using the wire model. The solid and dashed curves correspond to the  $p$ - and  $s$ -polarization of the incident light, respectively.

of the crosses  $2d = 500$  nm and the lattice period  $a = 800$  nm, which approximately corresponds to the geometry of our samples. The case of  $\alpha = \pm 27.5^\circ$  corresponds to our patterns 3 and 4 (shown as datapoints on the same graph). It is clear that the predictions of the wire model are in good agreement with the respective experimental data. In particular, the wire model predicts a smaller effect for the  $s$ -polarized incident light compared to that for the  $p$ -polarized incident light, which we observed experimentally. Patterns 7 and 8, which are chiral propellers, show a very weak polarization rotation and elliptization. These patterns resemble achiral crosses tilted with

respect to the lattice axes by a very small angle. From Fig. 5.1 we can estimate the tilting angle to be about  $10^\circ$ , with the tilting directions of the patterns 7 and 8 being the same as those of patterns 4 and 3, respectively. We also plotted the datapoints corresponding to patterns 7 and 8 in Fig. 5.4. The predictions of our wire model for this tilting angle agree well with our experimental data.

The wire model illustrates that the 2D structural chirality manifests itself in the optical activity of diffracted light, similar to that from pure 2D molecular chirality. This occurs even for highly symmetric normal incidence. For achiral particles, the sample is chiral whenever a distinct symmetry direction of each particle is tilted with respect to the lattice axes of the sample. For chiral particles the sample is always chiral, because the individual particles possess no symmetry direction with which to compare the lattice axes. Consequently, attempts to separate structural from molecular chirality in a sample consisting of chiral particles would be meaningless.

The similar polarization effects for both molecular and structural chirality can also be understood as manifestations of the chirality of the diffraction setup. Such chirality arises from the shape and orientation of a single nanoparticle in the setup, with the lattice only defining the directions of non-zero diffraction orders. The origin of the chirality of the setup can also be understood from a crystallographic perspective. Indeed, the 2D point symmetry group of both kinds of our chiral samples is  $p4$ , which lacks the in-plane mirror-reflection operation. Although the normal incidence geometry in our experiment is as symmetric as it can be, the diffraction direction is

off-normal as determined by the symmetry of the lattice. These factors give rise to the left–right asymmetry required for observing the polarization effects. It is important to keep in mind, however, that these symmetry-based considerations cannot give *quantitative* predictions, as they are not based on a detailed microscopic analysis and, in particular, do not include any assumptions about interparticle coupling. Thus, our experimental results and their analysis help to build a more detailed understanding of the polarization effects.

## 5.5 Conclusions

In conclusion, we have reported the observation of polarization rotation and elliptization of light diffracted from planar arrays consisting of either chiral or achiral nanoparticles. We have shown that, in both cases, the polarization changes are comparable; they are present even for non-mirror-symmetric patterns consisting of achiral particles (*i. e.*, possessing pure structural chirality). Our experimental data are in good agreement with the predictions of a simple wire model that describes light scattering from a planar achiral particle and includes no interparticle coupling. Our analysis of the data and the model suggests that diffraction experiments cannot distinguish between the polarization effects arising due to molecular and structural chirality of the samples. We believe that our study reported here clarifies the misconceptions related to separating molecular and structural chirality in diffraction experiments. Our findings also demonstrate that, in practical applications, patterns with pure struc-

tural chirality can be as efficient as those consisting of chiral particles, while having less pattern complexity and thus being easier to fabricate. Artificial planar structures with pure structural chirality can thus be considered as a whole new promising class of materials to be used in polarization control devices. This conclusion is not limited to metal-based structures considered in the present paper, but is also true for all-dielectric planar chiral structures [168], which may be promising because of lower losses and which will be a subject of a separate study.

The work reported in this chapter is a collaboration between Prof. Boyd's group, Dr. Sergei Volkov, and the groups of Prof. Martti Kauranen, Prof. Yuri Svirko, and Prof. Jari Turunen. It is submitted to Physical Review Letters [169].



# Chapter 6

## Summary

My Ph. D. dissertation, entitled “Local-Field Effects and Nanostructuring for Controlling Optical Properties and Enabling Novel Optical Phenomena,” consists of four major projects. Below I summarize the projects and my personal contributions.

1. “*Composite Laser Materials*”

Within this project, I have performed both theoretical and experimental investigations of the modification of laser properties of composite materials. First, Prof. Boyd and I have performed a proof-of-principle theoretical study of the modification of basic laser parameters by local-field effects, treating a composite laser gain medium as a quasi-homogeneous material. We have shown that significant changes to the basic laser parameters can be achieved.

However, more precise and sophisticated models are needed for separate composite geometries. I have developed such models for Maxwell Garnett composite

geometry with the resonance in inclusions and for layered composite geometry. Following my recipe, one can numerically solve the problem for more complex composite structures, such as Bruggeman geometry, where local field is non-uniform. An experimental validation of the theory will be performed by other graduate students from Prof. Boyd's research group.

The experimental part of the project involved the measurement of the radiative lifetime of Nd:YAG nanoparticles suspended in different liquids. I have experimentally demonstrated that the local-field effects can cause a significant change in the radiative lifetime of composite materials compared to that of the bulk materials. My experimental results obey the real-cavity model of local field. This conclusion should help to resolve a controversy in the literature regarding the influence of local-field effects on the radiative lifetime of liquid suspensions of nanoparticles.

This work is a collaboration with Prof. Peter Milonni. It is described in detail in Chapter 2 of the current thesis. The project gave a material for three publications: [24, 105, 116].

## 2. *“Microscopic Cascading Induced by Local-Field Effects”*

Within this project, I have theoretically predicted the existence of microscopic cascaded contribution from the third-order hyperpolarizability to the fifth-order nonlinear susceptibility, induced by local-field effects. This effect resembles the macroscopic, propagational cascading, in which a two-step third-order nonlinear

effect contributes to the fifth-order susceptibility. However, the microscopic cascading has a local nature and does not require propagation.

Performing a degenerate four-wave mixing experiment, I have successfully identified the microscopic cascaded effect and have shown that under certain conditions it can potentially be the dominant contribution to the total measured fifth-order nonlinear susceptibility. The reason why the microscopic cascading effect is important is because it has a potential application in the field of quantum optics where  $N$ -photon absorbing materials are needed.

This work is a collaboration with Prof. John Sipe and my colleague Heedeuk Shin, a graduate student from Prof. Boyd's group. It is covered in Chapter 3. The project resulted in two publications: [120, 121].

### 3. *“Cholesteric liquid crystal laser doped with oligofluorene”*

This project is a collaboration between Prof. Shaw Horng Chen's research group, Dr. Svetlana Lukishova, Prof. Boyd, and myself. Within this project, I have performed a comparative study of laser performances of cholesteric liquid crystals (CLCs) doped with two different laser dyes. One of the dyes is a well-known DCM, broadly used in CLC structures. The other dye, oligofluorene (OF), is a new laser dye with a high order parameter, synthesized in Prof. Shaw Horng Chen's group. I have experimentally shown that the new OF dye has a better laser performance in both transverse single-mode and multi-mode regimes, demonstrating higher total lasing output energy, better stability, and, under

certain conditions, higher slope efficiency [157]. More research in this area was done in Prof. Chen's group [156].

This work is described in detail in Chapter 4.

4. *“Optical activity in diffraction from artificial planar chiral structures”*

This project is a close collaboration between Dr. Sergei Volkov, Prof. Boyd's group, and the groups of Profs. Martti Kauranen, Jari Turunen, and Yuri Svirko from Finland. There have been many controversies in the literature regarding the optical activity in artificial chiral structures. Our study was aimed at resolving the contradictions.

My role was to perform an experimental part of the work, namely, the measurement of the polarization azimuth rotation and ellipticity of light, diffracted from planar structures with pure structural chirality. The measurements were also performed for the patterns with molecular chirality. The observed effects were similar for both types of patterns. The fact that the molecular and pure structural chirality manifest themselves similarly in diffraction invites the conclusion that it does not matter what is the origin of chirality in the sample. What matters is that both molecularly- and structurally-chiral patterns make the diffraction experimental setup chiral, which results in similar optical activity effects from both types of patterns. The statement was supported by a simple wire model that gave not only qualitative, but also a good quantitative description to my experimental data.

This work is described in Chapter 5. It gave a material for a publication [169].

I believe that the work that I have performed during my Ph. D. program will contribute to the development of new materials with improved optical properties, and to the conceptual understanding of some aspects of linear and nonlinear optics.

# Bibliography

- [1] A. Ikesue and Y. L. Aung, “Synthesis and performance of advanced ceramic lasers,” *J. Am. Ceram. Soc.* **89**, 1936–1944 (2006).
- [2] T. T. Basiev, M. E. Doroshenko, V. A. Konyushkin, V. V. Osiko, L. I. Ivanov, S. V. Simakov, “Lasing in diode-pumped fluoride nanostructure  $F_2^- : LiF$  colour centre ceramics,” *Quantum Electron.* **37**, 989–990 (2007).
- [3] F. J. Duarte and R. O. James, “Tunable Solid-State Lasers Incorporating Dye-Doped, Polymer-Nanoparticle Gain Media,” *Opt. Lett.* **28**, 2088–2090 (2003).
- [4] F. J. Duarte and R. O. James, “Spatial structure of dye-doped polymer nanoparticle laser media,” *Appl. Opt.* **43**, 4088–4090 (2004)
- [5] H. A. Lorentz, *Theory of Electrons*, 2nd ed. (Teubner, Leipzig, 1916).
- [6] J. D. Jackson, *Classical Electrodynamics*, 3rd ed. (Wiley, New York, 1999).
- [7] J. C. Maxwell Garnett, “Colours in metal glasses and in metallic films,” *Philos. Trans. R. Soc. London A* **203**, 385–420 (1904).
- [8] J. C. Maxwell Garnett, “Colours in metal glasses, in metallic films, and in metallic solutions,” *Philos. Trans. R. Soc. London A* **205**, 237–288 (1906).
- [9] V. M. Shalaev and M. I. Stockman, “Fractals: Optical susceptibility and giant Raman scattering,” *Z. Phys. D* **10**, 71–79 (1988).
- [10] R. J. Gehr and R. W. Boyd, “Optical properties of nanostructured optical materials,” *Chem. Mater.* **1996**, 1807–1819 (1996).
- [11] R. J. Glauber and M. Lewenstein, “Quantum optics of dielectric media,” *Phys. Rev. A* **43**, 467–491 (1991).

- [12] P. de Vries and A. Lagendijk, “Resonant scattering and spontaneous emission in dielectrics: Microscopic derivation of local-field effects,” *Phys. Rev. Lett.* **81**, 1381–1384 (1998).
- [13] P. W. Milonni, “Field quantization and radiative processes in dispersive dielectric media,” *J. Mod. Optics* **42**, 1991–2004 (1995).
- [14] M. S. Tomas, “Local-field corrections to the decay rate of excited molecules in absorbing cavities: The Onsager model,” *Phys. Rev. A* **63**, 053811 (2001).
- [15] H. T. Dung, S. Y. Buhmann, and D.-G. Welsch, “Local-field correction to the spontaneous decay rate of atoms embedded in bodies of finite size,” *Phys. Rev. A* **74**, 023803 (2006).
- [16] G. L. J. A. Rikken and Y. A. R. R. Kessener, “Local field effects and electric and magnetic dipole transitions in dielectrics,” *Phys. Rev. Lett.* **74**, 880–883 (1995).
- [17] F. J. P. Schuurmans, D. T. N. de Lang, G. H. Wegdam, R. Sprik, and A. Lagendijk, “Local-field effects on spontaneous emission in a dense supercritical gas,” *Phys. Rev. Lett.* **80**, 5077–5080 (1998).
- [18] G. M. Kumar, D. N. Rao, and G. S. Agarwal, “Measurement of local field effects of the host on the lifetimes of embedded emitters,” *Phys. Rev. Lett.* **91**, 203903 (2003).
- [19] G. M. Kumar, D. N. Rao, and G. S. Agarwal, “Experimental studies of spontaneous emission from dopants in an absorbing dielectric,” *Opt. Lett.* **30**, 732–734 (2005).
- [20] C.-K. Duan, M. F. Reid, and Z. Wang, “Local field effects on the radiative lifetime of emitters in surrounding media: Virtual- or real-cavity model?,” *Phys. Lett. A* **343**, 474–480 (2005).
- [21] P. Lavallard, M. Rosenbauer, and T. Gacoin, “Influence of surrounding dielectrics on the spontaneous emission of sulphorhodamine B molecules,” *Phys. Rev. A* **54**, 5450–5453 (1996).
- [22] G. Lamouche, P. Lavallard, and T. Gacoin, “Optical properties of dye molecules as a function of the surrounding dielectric medium,” *Phys. Rev. A* **59**, 4668–4674 (1999).
- [23] S. F. Wuister, C. de Mello Donega, and A. Meijerink, “Local-field effects on the spontaneous emission rate of CdTe and CdSe quantum dots in dielectric media,” *J. Chem. Phys.* **121**, 4310–4315 (2004).

- [24] K. P. Dolgaleva, R. W. Boyd, and P. W. Milonni, “Influence of local-field effects on the radiative lifetime of liquid suspensions of Nd:YAG nanoparticles,” *J. Opt. Soc. Am. B* **24**, 516–521 (2007).
- [25] J. E. Sipe and R. W. Boyd, “Nonlinear susceptibility of composite optical materials in the Maxwell Garnett model,” *Phys. Rev. A* **46**, 1614–1629 (1992).
- [26] J. E. Sipe and R. W. Boyd, “Nanocomposite materials for nonlinear optics based on local field effects,” in *Optical Properties of Nanostructured Random Media*, edited by V. M. Shalaev, *Topics Appl. Phys.* **82**, 1–19 (Springer-Verlag Berlin, Heidelberg, 2002).
- [27] R. W. Boyd and J. E. Sipe, “Nonlinear optical susceptibilities of layered composite materials,” *J. Opt. Soc. Am. B* **11**, 297–303 (1994).
- [28] R. W. Boyd, R. J. Gehr, G. L. Fischer, and J. E. Sipe, “Nonlinear optical properties of nanocomposite materials,” *Pure Appl. Opt.* **5**, 505–512 (1996).
- [29] G. L. Fischer, R. W. Boyd, R. J. Gehr, S. A. Jenekhe, J. A. Osaheni, J. E. Sipe, and L. A. Weller-Brophy, “Enhanced nonlinear optical response of composite materials,” *Phys. Rev. Lett.* **74**, 1871–1874 (1995).
- [30] D. D. Smith, G. Fischer, R. W. Boyd, and D. A. Gregory, “Cancellation of photoinduced absorption in metal nanoparticle composites through a counterintuitive consequence of local field effects,” *J. Opt. Soc. Am. B* **14**, 1625–1631 (1997).
- [31] R. L. Nelson and R. W. Boyd, “Enhanced electro-optic response of layered composite materials,” *Appl. Phys. Lett.* **74**, 2417–2419 (1999).
- [32] R. J. Gehr, G. L. Fischer, and R. W. Boyd, “Nonlinear-optical response of porous-glass-based composite materials,” *J. Opt. Soc. Am. B* **14**, 2310–2314 (1997).
- [33] X. C. Zeng, D. J. Bergman, P. M. Hui, and D. Stroud, “Effective-medium theory for weakly nonlinear composites,” *Phys. Rev. B* **38**, 10970–10973 (1988).
- [34] M. Born and E. Wolf, *Principles of Optics* 6th ed. (Cambridge University Press, 1997).
- [35] R. Landauer, “The electrical resistance of binary metallic mixtures,” *J. Appl. Phys.* **23**, 779–784 (1952).



- [36] J. Guo, J. Cooper, and A. Gallagher, “Selective reflection from a dense atomic vapor,” *Phys. Rev. A* **53**, 1130–1138 (1996).
- [37] D. E. Aspnes, “Local-field effects and effective-medium theory: A microscopic perspective,” *Am. J. Phys.* **50**, 704–709 (1982).
- [38] L. Onsager, “Electric moments of molecules in liquids,” *J. Am. Chem. Soc.* **58** 1486–1493 (1936).
- [39] F. Hynne and R. K. Bullough, “The Onsager reaction field as a screened self-interaction in refractive-index theory,” *J. Phys. A* **5**, 1272–1295 (1972).
- [40] J. U. Andersen and E. Bonderup, “Local field corrections for light absorption by fullerenes,” *Eur. Phys. J. D* **11**, 435–448 (2000).
- [41] F. A. Hopf, C. M. Bowden, and W. H. Louisell, “Mirrorless optical bistability with the use of the local-field correction,” *Phys. Rev. A* **29**, 2591–2596 (1984).
- [42] I. Abram and A. Maruani, “Calculation of the nonlinear dielectric function in semiconductors,” *Phys. Rev. B* **26**, 4759–4761 (1982).
- [43] F. A. Hopf and C. M. Bowden, “Heuristic stochastic model of mirrorless optical bistability,” *Phys. Rev. A* **32**, 268–275 (1985).
- [44] Y. Ben-Aryeh, C. M. Bowden, and J. C. Englund, “Intrinsic optical bistability in collections of spatially distributed two-level atoms,” *Phys. Rev. A* **34**, 3917–3926 (1986).
- [45] J. J. Maki, M. S. Malcuit, J. E. Sipe, and R. W. Boyd, “Linear and nonlinear optical measurements of the Lorentz local field,” *Phys. Rev. Lett.* **67**, 972–975 (1991).
- [46] H. van Kampen, V. A. Sautenkov, C. J. C. Smeets, E. R. Eliel, and J. P. Woerdman, “Measurement of the excitation dependence of the Lorentz local-field shift,” *Phys. Rev. A* **59**, 271–274 (1999).
- [47] C. R. Stroud, Jr., C. M. Bowden, and L. Allen, “Self-induced transparency in self-chirped media,” *Opt. Commun.* **67**, 387–390 (1988).
- [48] N. Wang and H. Rabitz, “Near dipole-dipole effects in electromagnetically induced transparency,” *Phys. Rev. A* **51**, 5029–5031 (1995).
- [49] J. P. Dowling and C. M. Bowden, “Near dipole-dipole effects in lasing without inversion: An enhancement of gain and absorptionless index of refraction,” *Phys. Rev. Lett.* **70**, 1421–1424 (1993).

- [50] A. S. Manka, J. P. Dowling, C. M. Bowden, and M. Fleischhauer, “Piezophotonic switching due to local field effects in a coherently prepared medium of three-level atoms,” *Phys. Rev. Lett.* **73**, 1789–1792 (1994).
- [51] A. S. Manka, J. P. Dowling, C. M. Bowden, and M. Fleischhauer, “A review of local field effects in lasing without inversion,” *Quantum Opt.* **6**, 371–380 (1994).
- [52] S. Singh, C. M. Bowden, and J. Rai, “Gain enhancement in lasing without inversion in an optically dense medium,” *Opt. Commun.* **135**, 93–97 (1997).
- [53] A. S. Zibrov, M. D. Lukin, L. Hollberg, D. E. Nikonov, M. O. Scully, H. G. Robinson, and V. L. Velichansky, “Experimental demonstration of enhanced index of refraction via quantum coherence in Rb,” *Phys. Rev. Lett.* **76**, 3935–3938 (1996).
- [54] A. S. Zibrov, A. B. Matsko, L. Hollberg, and V. L. Velichansky, “Resonant enhancement of refractive index in a cascade scheme,” *J. Mod. Optics* **49**, 359–365 (2002).
- [55] N. Bloembergen, *Nonlinear Optics*, 4th ed. (World Scientific, Singapore, 1996).
- [56] R. W. Boyd, *Nonlinear Optics*, 2nd ed. (Academic Press, New York, 2003).
- [57] Y. R. Shen, *The Principles of Nonlinear Optics*, (J. Wiley, New York, 1984).
- [58] E. Yablonovitch, C. Flytzanis, and N. Bloembergen, “Anisotropic interference of three-wave and double two-wave frequency mixing in GaAs,” *Phys. Rev. Lett.* **29**, 865–866 (1972).
- [59] S. D. Kramer, F. G. Parsons, and N. Bloembergen, “Interference of third-order light mixing and second-harmonic exciton generation in CuCl,” *Phys. Rev. B* **9**, 1853–1856 (1974).
- [60] G. R. Meredith, “Cascading in optical third-harmonic generation by crystalline quartz,” *Phys. Rev. B* **24**, 5522–5532 (1981).
- [61] R. DeSalvo, D. J. Hagan, M. Sheik-Bahae, G. Stegeman, E. W. Van Stryland, and H. Vanherzeele, “Self-focusing and self-defocusing by cascaded second-order effects in KTP,” *Opt. Lett.* **17**, 28–30 (1992).

- [62] G. I. Stegeman, M. Sheik-Bahae, E. Van Stryland, and G. Assanto, “Large nonlinear phase shifts in second-order nonlinear-optical processes,” *Opt. Lett.* **18**, 13–15 (1993).
- [63] Y. Baek, R. Schiek, and G. I. Stegeman, “All-optical switching in a hybrid Mach-Zender interferometer as a result of cascaded second-order nonlinearity,” *Opt. Lett.* **20**, 2168–2170 (1995).
- [64] R. Schiek, Y. Baek, and G. I. Stegeman, “One-dimensional spatial solitary waves due to cascaded second-order nonlinearities in planar waveguides,” *Phys. Rev. E* **53**, 1138–1141 (1996).
- [65] J. B. Khurgin, A. Obeidat, S. J. Lee, and Y. J. Ding, “Cascaded optical nonlinearities: Microscopic understanding as a collective effect,” *J. Opt. Soc. Am. B* **14**, 1977–1983 (1997).
- [66] G. I. Stegeman, D. J. Hagan, and L. Torner, “ $\chi^{(2)}$  cascading phenomena and their applications to all-optical signal processing, mode-locking, pulse compression and solitons,” *Opt. Quantum Electron.* **28**, 1691–1740 (2004).
- [67] G. I. Stegeman, “ $\chi^{(2)}$  cascading: nonlinear phase shifts,” *Quantum Semi-class. Opt.* **9**, 139–153 (1997).
- [68] D. Bedeaux and N. Bloembergen, “On the relation between macroscopic and microscopic nonlinearities,” *Physica* **69**, 57–66 (1973).
- [69] J. Ducuing, in *Nonlinear Optics*, edited by P. G. Harper and B. S. Wewretz (Academic Press, New York, 1975).
- [70] C. Flytzanis, in *Quantum Electronics*, edited by H. Rabin and C. L. Tang (Academic Press, New York, 1975).
- [71] G. R. Meredith, in *Nonlinear Optics: Methods and Devices*, edited by C. Flytzanis and J. L. Oudar (Springer-Verlag, Berlin, 1986).
- [72] J. H. Andrews, K. L. Kowalski, and K. D. Singer, “Pair correlations, cascading, and local-field effects in nonlinear optical susceptibilities,” *Phys. Rev. A* **46**, 4172–4184 (1992).
- [73] C. Kolleck, “Cascaded second-order contribution to the third-order nonlinear susceptibility,” *Phys. Rev. A* **69**, 053812 (2004).
- [74] L. S. Goldberg and J. M. Schnur, “Tunable internal-feedback liquid crystal-dye laser,” *US Patent*, 3, 771, 065 (1973).

- [75] N. V. Kukhtarev, "Cholesteric liquid crystal laser with distributed feedback," *Sov. J. Quantum Electron.* **8**, 774–776 (1978).
- [76] I. P. Ilchishin, E. A. Tikhonov, V. G. Tishchenko, and M. T. Shpak, "Generation of a tunable radiation by impurity cholesteric liquid crystals," *JETP Lett.* **32**, 24–27 (1980).
- [77] I. P. Ilchishin, A. G. Kleopov, E. A. Tikhonov, and M. T. Shpak, "Stimulated tunable radiation in an impurity cholesteric liquid crystal," *Bull. Acad. Sci. USSR, Phys. Ser.* **45**, 1376–1383 (1981).
- [78] I. P. Ilchishin, "Optimizing energy output and angular divergence of a DFB laser with cholesteric liquid crystal," *Bull. Russian Acad. Sci. Phys.* **60**, 494–498 (1996).
- [79] V. I. Kopp, B. Fan, H. K. M. Vithana, and A. Z. Genack, "Low-threshold lasing at the edge of a photonic stop band in cholesteric liquid crystals," *Opt. Lett.* **23**, 1707–1709 (1998).
- [80] B. Taheri, P. Palffy-Muhoray, and H. Kabir, *ALCOM Symposium. Chiral Materials and Applications*, Cayahoga Falls, Feb. 18–19 (1999).
- [81] J. Schmidtke and W. Stille, "Fluorescence of a dye-doped cholesteric liquid crystal film in the region of the stop band: theory and experiment," *Eur. Phys. J. B* **31**, 179–194 (2003).
- [82] K. C. Shin, F. Araoka, B. Park, Y. Takanishi, K. Ishikawa, Z. Zhu, T. M. Swager, and H. Takezoe, "Advantages of highly ordered polymer-dyes for lasing in chiral nematic liquid crystals," *Jpn. J. Appl. Phys.* **43**, 631–636 (2004).
- [83] B. M. Conger, J. C. Mastrangelo, and S. H. Chen, "Fluorescence behavior of low molar mass and polymer liquid crystals in ordered solid films," *Macromolecules* **30**, 4049–4055 (1997).
- [84] S. M. Morris, A. D. Ford, M. N. Pivnenko, and H. J. Coles, "Enhanced emission from liquid-crystal lasers," *J. Appl. Phys.* **97**, 023103 (2005).
- [85] A. Papakostas, A. Potts, D. M. Bagnall, S. L. Prosvirnin, H. J. Coles, and N. I. Zheludev, "Optical manifestation of planar chirality," *Phys. Rev. Lett.* **90**, 107404 (2003).
- [86] A. Potts, A. Papakostas, D. M. Bagnall, and N. I. Zheludev, "Planar chiral meta-materials for optical applications," *Microelectron. Engineering* **73–74**, 367–371 (2004).

- [87] S. Takahashi, A. Potts, D. Bagnall, N. I. Zheludev, and A. V. Zayats, “Near-field polarization conversion in planar chiral nanostructures,” *Opt. Commun.* **255**, 91–96 (2005).
- [88] W. Zhang, A. Potts, A. Papakostas, and D. M. Bagnall, “Intensity modulation and polarization rotation of visible light by dielectric planar chiral metamaterials,” *Appl. Phys. Lett.* **86**, 231905 (2005).
- [89] W. Zhang, A. Potts, and D. M. Bagnall, “Giant optical activity in dielectric planar metamaterials with two-dimensional chirality,” *J. Opt. A: Pure Appl. Opt.* **8**, 878–890 (2006).
- [90] M. Kuwata-Gonokami, N. Saito, Y. Ino, M. Kauranen, K. Jefimovs, T. Vallius, J. Turunen, and Y. Svirko, “Giant optical activity in quasi-two-dimensional planar nanostructures,” *Phys. Rev. Lett.* **95**, 227401 (2005).
- [91] F. Miyamaru and M. Hangyo, “Strong optical activity in chiral metamaterials of metal screw hole arrays,” *Appl. Phys. Lett.* **89**, 211105 (2006).
- [92] A. V. Krasavin, A. S. Schwanecke, N. I. Zheludev, M. Reichelt, T. Stroucken, S. W. Koch, and E. M. Wright, “Polarization conversion and “focusing” of light propagating through a small chiral hole in a metallic screen,” *Appl. Phys. Lett.* **86**, 201105 (2005).
- [93] C. Genet, E. Altewischer, M. P. van Exter, and J. P. Woerdman, “Optical depolarization induced by arrays of subwavelength metal holes,” *Phys. Rev. B* **71**, 033409 (2005).
- [94] A. V. Krasavin, A. S. Schwanecke, and N. I. Zheludev, “Extraordinary properties of light transmission through a small chiral hole in a metallic screen,” *J. Opt. A: Pure Appl. Opt.* **8**, S98–S105 (2006).
- [95] V. A. Fedotov, P. L. Mladyonov, S. L. Prosvirnin, A. V. Rogacheva, Y. Chen, and N. I. Zheludev, “Asymmetric propagation of electromagnetic waves through a planar chiral structure,” *Phys. Rev. Lett.* **97**, 167401 (2006).
- [96] A. S. Schwanecke, A. Krasavin, D. M. Bagnall, A. Potts, A. V. Zayats, and N. I. Zheludev, “Broken time reversal symmetry of light interaction with planar chiral nanostructures,” *Phys. Rev. Lett.* **91**, 247404 (2003).
- [97] S. L. Prosvirnin and N. I. Zheludev, “Polarization effects in the diffraction of light by a planar chiral structure,” *Phys. Rev. E* **71**, 037603 (2005).

- [98] B. K. Canfield, S. Kujala, K. Jefimovs, J. Turunen, and M. Kauranen, “Linear and nonlinear optical responses induced by broken symmetry in an array of gold nanoparticles,” *Opt. Express* **12**, 5418–5423 (2004).
- [99] B. K. Canfield, S. Kujala, K. Jefimovs, T. Vallius, J. Turunen, and M. Kauranen, “Polarization effects in the linear and nonlinear optical responses of gold nanoparticle arrays,” *J. Opt. A: Pure Appl. Opt.* **7**, S110–S117 (2005).
- [100] B. K. Canfield, S. Kujala, M. Kauranen, K. Jefimovs, T. Vallius, and J. Turunen, “Remarkable polarization sensitivity of gold nanoparticle arrays,” *Appl. Phys. Lett.* **86**, 183109 (2005).
- [101] B. K. Canfield, S. Kujala, K. Jefimovs, Y. Svirko, J. Turunen, and M. Kauranen, “A macroscopic formalism to describe the second-order nonlinear optical response of nanostructures,” *J. Opt. A: Pure Appl. Opt.* **8**, S278–S284 (2006).
- [102] B. K. Canfield, S. Kujala, K. Laiho, K. Jefimovs, J. Turunen, and M. Kauranen, “Chirality arising from small defects in gold nanoparticle arrays,” *Opt. Express* **14**, 950–955 (2006).
- [103] E. Snoeks, A. Lagendijk, and A. Polman, “Measuring and modifying the spontaneous emission rate of erbium near an interface,” *Phys. Rev. Lett.* **74**, 2459–2462 (1995).
- [104] A. E. Siegman, *Lasers*, (University Science Books, Sausalito, California, 1986).
- [105] K. Dolgaleva and R. W. Boyd, “Laser gain media based on nanocomposite materials,” *J. Opt. Soc. Am. B* **24**, A19–A25 (2007).
- [106] *Cavity Quantum Electrodynamics*, ed. P. R. Berman (Academic, Boston, 1994).
- [107] R. S. Meltzer, S. P. Feofilov, B. Tissue, and H. B. Yuan, “Dependence of fluorescence lifetimes of  $\text{Y}_2\text{O}_3 : \text{Eu}^{3+}$  nanoparticles on the surrounding medium,” *Phys. Rev. B* **60**, R14012–R14015 (1999).
- [108] H. P. Christensen, D. R. Gabbe, and H. P. Jenssen, “Fluorescence lifetimes for neodymium-doped yttrium aluminum garnet and yttrium oxide powders,” *Phys. Rev. B* **25**, 1467–1473 (1982).
- [109] N. P. Barnes and B. M. Walsh, “Amplified spontaneous emission: Application to Nd : YAG lasers,” *IEEE J. Quantum Electron.* **35**, 101–109 (1999).

- [110] T. S. Lomheim and L. G. DeShazer, “Determination of optical cross-sections by the measurement of saturation flux using laser-pumped laser-oscillators,” *J. Opt. Soc. Am.* **68**, 1575–1579 (1978).
- [111] T. Kushida and J. E. Geusic, “Optical refrigeration in Nd-doped yttrium aluminum garnet,” *Phys. Rev. Lett.* **21**, 1172–1175 (1968).
- [112] S. Singh, R. G. Smith, and L. G. Van Uitert, “Stimulated-emission cross section and fluorescent quantum efficiency of  $\text{Nd}^{3+}$  in yttrium aluminum garnet at room temperature,” *Phys. Rev. B* **10**, 2566–2572 (1974).
- [113] A. Rosencwaig and E. A. Hildum, “ $\text{Nd}^{3+}$  fluorescence quantum-efficiency measurements with photoacoustics,” *Phys. Rev. B* **23**, 3301–3307 (1981).
- [114] C. J. Kennedy and J. D. Barry, “New evidence on quantum efficiency of Nd : YAG,” *Appl. Phys. Lett.* **31**, 91–92 (1977).
- [115] J. T. Manassah and B. Gross, “Amplification by an optically dense resonant two-level system embedded in a dielectric medium,” *Opt. Commun.* **155**, 213–222 (1998).
- [116] K. Dolgaleva, R. W. Boyd, and P. W. Milonni, “Effects of local fields on laser gain for layered and Maxwell Garnett composite materials,” accepted for publication in *J. Phys. A*.
- [117] R. S. Bennink, Y. K. Yoon, and R. W. Boyd, “Accessing the optical non-linearity of metals with metal-dielectric photonic bandgap structures,” *Opt. Lett.* **24**, 1416–1418 (1999).
- [118] A. N. Boto, *et al.*, “Quantum interferometric optical lithography: exploiting entanglement to beat the diffraction limit,” *Phys. Rev. Lett.* **85**, 2733–2736 (2000).
- [119] H. J. Chang, H. Shin, M. N. O’Sullivan-Hale, and R. W. Boyd, “Implementation of sub-Rayleigh-resolution lithography using an N-photon absorber,” *J. Mod. Opt.* **53**, 2271–2277 (2006).
- [120] K. Dolgaleva, R. W. Boyd, and J. E. Sipe, “Cascaded nonlinearity caused by local-field effects in the two-level atom,” *Phys. Rev. A* **76**, 063806 (2007).
- [121] K. Dolgaleva, H. Shin, R. W. Boyd, and J. E. Sipe, “Observation of microscopic cascaded contribution to the fifth-order nonlinear susceptibility,” to be submitted to *Phys. Rev. Lett.*

- [122] E. Koudoumas, F. Dong, M. D. Tzatzadaki, S. Couris, and S. Leach, “High-order nonlinear optical response of C<sub>60</sub>-toluene solutions in the sub-picosecond regime ,” *J. Phys. B* **29**, L773–L778 (1996).
- [123] M. Sheik-Bahae, A. A. Said, and E. W. Van Stryland, “High-sensitivity, single-beam  $n_2$  measurements,” *Opt. Lett.* **14**, 955–957 (1989).
- [124] S. Couris, E. Koudoumas, F. Dong, and S. Leach, “Sub-picosecond studies of the third-order optical nonlinearities of C<sub>60</sub>-toluene solutions,” *J. Phys. B* **29**, 5033–5041 (1996).
- [125] F. Araoka, K.-C. Shin, Y. Takanishi, K. Ishikawa, H. Takezoe, Z. Zhu, and T. M. Swager, “How doping a cholesteric liquid crystal with polymeric dye improves an order parameter and makes possible low threshold lasing,” *J. Appl. Phys.* **94**, 279–283 (2003).
- [126] S. Furumi, S. Yokoyama, A. Otomo, and S. Mashiko, “Electrical control of the structure and lasing in chiral photonic band-gap liquid crystals,” *Appl. Phys. Lett.* **82**, 16–18 (2003).
- [127] W. Cao, P. Palffy-Muhoray, B. Taheri, A. Marino, and G. Abbate, “Lasing thresholds of cholesteric liquid crystal lasers,” *Mol. Cryst. Liq. Cryst.* **429**, 101–110 (2005).
- [128] A. Chanishvili, G. Chilaya, G. Petriashvili, R. Barberi, R. Bartolino, G. Cipparrone, A. Mazzulla, R. Gimenez, L. Oriol, and M. Pinol, “Widely tunable ultraviolet-visible liquid crystal laser,” *Appl. Phys. Lett.* **86**, 051107 (2005).
- [129] S. M. Morris, A. D. Ford, M. N. Pivnenko, and H. J. Coles, “The effects of reorientation on the emission properties of a photonic band edge liquid crystal laser,” *J. Opt. A: Pure Appl. Opt.* **7**, 215–223 (2005).
- [130] S. M. Morris, A. D. Ford, C. Gillespie, M. N. Pivnenko, O. Hadeler, and H. Y. Coles, “The emission characteristics of liquid-crystal lasers,” *J. Soc. Inf. Disp.* **14**, 565–573 (2006).
- [131] S. Furumi and Y. Sakka, “Chiroptical properties induced in chiral photonic-bandgap liquid crystals leading to a highly efficient laser-feedback effects,” *Adv. Mater.* **18**, 775–780 (2006).
- [132] E. Alvarez, M. He, A. F. Munoz, P. Palffy-Muhoray, S. V. Serak, B. Taheri, and R. Tweig, “Mirrorless lasing and energy transfer in cholesteric liquid crystals doped with laser dyes,” *Mol. Cryst. Liq. Cryst.* **369**, 75–82 (2001).



- [133] Y. Huang, Y. Zhou, Q. Hong, A. Rapaport, M. Bass, and S.-T. Wu, “Incident angle and polarization effects on the dye-doped cholesteric liquid crystal laser,” *Opt. Commun.* **261**, 91–96 (2006).
- [134] L. M. Blinov, G. Cipparrone, A. Mazzulla, P. Pagliusi, and V. V. Lazarev, “Lasing in cholesteric liquid crystal cells: competition of Bragg and leaky modes,” *J. Appl. Phys.* **101**, 053104 (2007).
- [135] A. F. Munoz, P. Palffy-Muhoray, and B. Taheri, A. F. Munoz, P. Palffy-Muhoray, and B. Taheri, “Ultraviolet lasing in cholesteric liquid crystals,” *Opt. Lett.* **26**, 804–806 (2001).
- [136] H. Finkelmann, S. T. Kim, A. Munoz, P. Palffy-Muhoray, and B. Taheri, “Tunable mirrorless lasing in cholesteric liquid crystalline elastomers,” *Adv. Mater.* **13**, 1069–1072 (2001).
- [137] J. Schmidtke, W. Stille, H. Finkelmann, and S. T. Kim, “Laser emission in a dye doped cholesteric polymer network,” *Adv. Mater.* **14**, 746–749 (2002).
- [138] H. Yu, B. Y. Tang, J. Li, and L. Li, “Electrically tunable lasers made from electrooptically active photonic band gap materials,” *Opt. Express* **13**, 7243–7249 (2005).
- [139] P. V. Shibaev, V. Kopp, A. Genack, and E. Hanelt, “Lasing from chiral photonic band gap materials based on cholesteric glasses,” *Liq. Cryst.* **30**, 1391–1400 (2003).
- [140] W. Cao, A. Munoz, P. Palffy-Muhoray, and B. Taheri, “Lasing in a three-dimensional photonic crystal of the liquid crystal blue phase II,” *Nature Mat.* **1**, 111–113 (2002).
- [141] M. Ozaki, M. Kasano, D. Ganzke, W. Haase, and K. Yoshino, “Mirrorless lasing in a dye-doped ferroelectric liquid crystal,” *Adv. Mater.* **14**, 306–309 (2002).
- [142] A. S. Furumi, S. Yokoyama, A. Otomo, and S. Mashiko, “Phototunable photonic bandgap in a chiral liquid crystal device,” *Appl. Phys. Lett.* **84**, 2491–2493 (2004).
- [143] T.-H. Lin, Y.-J. Chen, C.-H. Wu, A. Y.-G. Fuh, J.-H. Liu, and P.-C. Yang, “Cholesteric liquid crystal laser with wide tuning capability,” *Appl. Phys. Lett.* **86**, 161120 (2005).
- [144] P. V. Shibaev, R. L. Sanford, D. Chiappetta, V. Milner, A. Genack, and A. Bobrovsky, “Light controllable tuning and switching of lasing in chiral liquid crystals,” *Opt. Express* **13**, 2358–2363 (2005).

- [145] I. P. Ilchishin, O. V. Yaroshchuk, S. V. Gryshchenko, and E. A. Shaydiuk, "Influence of the light induced molecular transformations on the helix pitch and lasing spectra of cholesteric liquid crystals," *Proc. SPIE* **5507**, 229–234 (2004).
- [146] A. Chanishvili, G. Chilaya, G. Petriashvili, R. Barberi, R. Bartolino, G. Cipparrone, A. Mazzulla, and L. Oriol, "Lasing in dye-doped cholesteric liquid crystals: two new tuning strategies," *Adv. Mater.* **16**, 791–795 (2004).
- [147] M.-Y. Jeong, H. Choi, and Y. W. Wu, "Spatial tuning of laser emission in a dye-doped cholesteric liquid crystal wedge cell," *Appl. Phys. Lett.* **92**, 051108 (2008).
- [148] H. Shi, B. M. Conger, D. Katsis, and S. H. Chen, "Circularly polarized fluorescence from chiral nematic liquid crystalline films: theory and experiment," *Liq. Cryst.* **24**, 163–172 (1998).
- [149] K. L. Woon, M. O'Neill, G. J. Richards, M. P. Aldred, and S. M. Kelly, "Stokes parameter studies of spontaneous emission from chiral nematic liquid crystals as a one-dimensional photonic stopband crystal: experiment and theory," *Phys. Rev. E* **71**, 041706 (2005).
- [150] S. H. Chen, D. Katsis, A. W. Schmid, J. C. Mastrangelo, T. Tsutsui, and T. N. Blanton, "Circularly polarized light generated by photoexcitation of luminophores in glassy liquid-crystal films," *Nature* **397**, 506–508 (1999).
- [151] D. Katsis, A. W. Schmid, and S. H. Chen, "Mechanistic insight into circularly polarized photoluminescence from a chiral-nematic film," *Liq. Cryst.* **26**, 181–185 (1999).
- [152] M. Voigt, M. Chambers, and M. Grell, "On the circular polarization of fluorescence from dyes dissolved in chiral nematic liquid crystals," *Chem. Phys. Lett.* **347**, 173–177 (2001).
- [153] K. Amemiya, K.-C. Shin, Y. Takanishi, K. Ishikawa, R. Azumi, and H. Takezoe, "Lasing in cholesteric liquid crystals doped with oligothiophene derivatives," *Jpn. J. Appl. Phys.* **43**, 6084–6087 (2004).
- [154] Y. Geng, A. C. A. Chen, J. J. Ou, S. H. Chen, K. Klubek, K. M. Vaeth, and C. W. Tang, "Monodisperse glassy-nematic conjugated oligomers with chemically tunable polarized light emission," *Chem. Mater.* **15**, 4352–4360 (2003).

- [155] O. G. Peterson, J. P. Webb, W. C. McColgin, and J. H. Eberly, "Organic dye laser threshold," *J. Appl. Phys.* **42**, 1917–1928 (1971).
- [156] S. K. H. Wei, S. H. Chen, K. Dolgaleva, S. G. Lukishova, and R. W. Boyd, "Robust organic lasers comprising glassy-cholesteric pentafluorene doped with a red-emitting oligofluorene," submitted to *Appl. Phys. Lett.*
- [157] K. Dolgaleva, S. K. H. Wei, S. G. Lukishova, S. H. Chen, K. Schwertz, and R. W. Boyd, "Enhanced laser performance of cholesteric liquid crystals doped with oligofluorene dye," *J. Opt. Soc. Am. B* **25**, 1496–1504 (2008).
- [158] S. Bassiri, C. H. Papas, and N. Engheta, "Electromagnetic wave propagation through a dielectric-chiral interface and through a chiral slab," *J. Opt. Soc. Am. A* **5**, 1450–1459 (1988).
- [159] J. B. Biot, "Mémoire sur la polarisation circulaire et sur ses applications A la chimie organique," *Mem. Acad. Sci.* **13**, 39–175 (1835);
- [160] J. B. Biot, "Phénomènes de polarisation successive, observés dans des fluides homogènes,," *Bull. Soc. Philomath.* 190–192 (1815).
- [161] J. R. Appling, M. G. White, T. M. Orlando, and S. L. Anderson, "Observation of circular dichroism in photoelectron angular distributions," *J. Chem. Phys.* **85**, 6803 (1986);
- [162] C. Westphal, J. Bansmann, M. Getzlaff, and G. Schönhense, "Circular dichroism in the angular distribution of photoelectrons from oriented CO molecules," *Phys. Rev. Lett.* **63**, 151–154 (1989);
- [163] N. Chandra, "Circular dichroism in photoionization of oriented nonlinear molecules," *Phys. Rev. A* **39**, 2256–2259 (1989);
- [164] R. L. Dubs, S. N. Dixit, and V. McKoy, "Circular dichroism in photoelectron angular distributions from oriented linear molecules," *Phys. Rev. Lett.* **54**, 1249–1251 (1985);
- [165] T. Verbiest, M. Kauranen, Y. Van Rompaey, and A. Persoons, "Optical Activity of Anisotropic Achiral Surfaces," *Phys. Rev. Lett.* **77**, 1456–1459 (1996).
- [166] T. Vallius, K. Jefimovs, J. Turunen, P. Vahimaa, and Y. Svirko, "Optical activity in subwavelength-period arrays of chiral metallic particles," *Appl. Phys. Lett.* **83**, 234–236 (2003).

- [167] M. Decker, M. W. Klein, M. Wegener, and S. Linden, “Circular dichroism of planar chiral magnetic metamaterials,” *Opt. Lett.* **32**, 856–858 (2007).
- [168] K. Konishi, B. Bai, X. Meng, P. Karvinen, J. Turunen, Y. P. Svirko, and M. Kuwata-Gonokami, “Observation of extraordinary optical activity in planar chiral photonic crystals,” *Opt. Express*, **16**, 7189–7196 (2008).
- [169] S. N. Volkov, K. Dolgaleva, R. W. Boyd, K. Jefimovs, J. Turunen, Y. Svirko, B. K. Canfield, and M. Kauranen, “Optical activity in diffraction from a planar array of achiral nanoparticles,” submitted to *Phys. Rev. Lett.*
- [170] M. Abramowitz and I. A. Stegun, *Handbook of Mathematical Functions with Formulas, Graphs, and Mathematical Tables*, 10th printing (National Bureau of Standards, Washington DC, 1972).

# Appendix A

## Mesoscopic Field in an Inclusion of a Maxwell Garnett Composite

### Material

In this Appendix we derive the expression for the mesoscopic field in an inclusion of a Maxwell Garnett composite material. As a starting point, we use the result for the mesoscopic field  $\mathbf{e}(\mathbf{r})$  at any point  $\mathbf{r}$  of a Maxwell Garnett composite, obtained in [25] (Eq. (3.8)):

$$\mathbf{e}(\mathbf{r}) = \mathbf{E}(\mathbf{r}) + \int \overleftrightarrow{\mathbf{T}}(\mathbf{r} - \mathbf{r}') \mathbf{p}'(\mathbf{r}') d\mathbf{r}' + \frac{4\pi}{3\epsilon_h} [\mathbf{P}'(\mathbf{r}) - \mathbf{p}'(\mathbf{r})]. \quad (\text{A.1})$$

Here  $\overleftrightarrow{\mathbf{T}}(\mathbf{r})$  designates a static dipole-dipole coupling tensor for a host medium with dielectric constant  $\epsilon_h$ . The mesoscopic polarization  $\mathbf{p}'(\mathbf{r})$  is a linear part of the source

polarization defined in [25] (we will refer to it as the linear source polarization). It is defined as

$$\mathbf{p}'(\mathbf{r}) = \begin{cases} (\chi_i^{(1)} - \chi_h^{(1)})\mathbf{e}(\mathbf{r}), & \text{if } r \in \text{inclusion,} \\ 0, & \text{if } r \in \text{host.} \end{cases} \quad (\text{A.2})$$

Here  $\chi_i^{(1)}$  and  $\chi_h^{(1)}$  are the susceptibilities of the inclusion and host media, respectively.

In this study we are not concerned with the nonlinear interactions, so we do not consider the nonlinear part of the source polarization. The macroscopic linear source polarization  $\mathbf{P}'(\mathbf{r})$  is obtained by averaging  $\mathbf{p}'(\mathbf{r})$ ,

$$\mathbf{P}'(\mathbf{r}) = \int \tilde{\Delta}(\mathbf{r} - \mathbf{r}')\mathbf{p}'(\mathbf{r}') d\mathbf{r}', \quad (\text{A.3})$$

where  $\tilde{\Delta}(\mathbf{r})$  is a smoothly varying weighting function which has a range  $R$  much smaller than the wavelength of light, but much larger than a typical separation distance between the inclusions. The weighting function is normalized to unity:

$$\int \tilde{\Delta}(\mathbf{r} - \mathbf{r}') d\mathbf{r}' = 1. \quad (\text{A.4})$$

We are considering the mesoscopic field in an inclusion of the Maxwell Garnett composite material. In the case of an isotropic and uniform inclusion material one can assume that the polarization  $\mathbf{p}'(\mathbf{r})$  and the electric field  $\mathbf{e}(\mathbf{r})$  are mesoscopically uniform over an inclusion. Based on the above assumption and on the mathematical arguments given in Ref. [25], we can set the term involving the dipole-dipole coupling

tensor in Eq. (A.1) equal to zero. It brings us to the expression

$$\mathbf{e}_i(\mathbf{r}) = \mathbf{E}(\mathbf{r}) + \frac{4\pi}{3\epsilon_h} [\mathbf{P}'(\mathbf{r}) - \mathbf{p}'(\mathbf{r})] \quad (\text{A.5})$$

for the mesoscopic field in an inclusion. We can find the macroscopic average polarization  $\mathbf{P}'(\mathbf{r})$  from Eq. (A.3), using the assumption that  $\mathbf{p}'(\mathbf{r})$  is mesoscopically uniform over an inclusion:

$$\mathbf{P}'(\mathbf{r}) = f_i \mathbf{p}'(\mathbf{r}). \quad (\text{A.6})$$

Here  $f_i$  is the volume fraction of the inclusions in the composite material. Using Eq. (A.2), we can express the mesoscopic polarization  $\mathbf{p}_i(\mathbf{r})$  in an inclusion as

$$\mathbf{p}_i(\mathbf{r}) = \chi_h^{(1)} \mathbf{e}_i(\mathbf{r}) + \mathbf{p}'(\mathbf{r}). \quad (\text{A.7})$$

Substituting Eqs. (A.6) and (A.7) into Eq. (A.5) and making use of the relation  $f_h + f_i = 1$  for the volume fractions of the host and inclusion materials, we obtain the expression

$$\mathbf{e}_i(\mathbf{r}) = \frac{3\epsilon_h}{3\epsilon_h - 4\pi f_h \chi_h^{(1)}} \left[ \mathbf{E}(\mathbf{r}) - \frac{4\pi}{3\epsilon_h} f_h \mathbf{p}_i(\mathbf{r}) \right] \quad (\text{A.8})$$

for the mesoscopic field in an inclusion.

# Appendix B

## Multiple Solutions for the Population Inversion

Let us consider in which part of parameter space Eq. (3.1a) has more than one physical solution. It is convenient to rewrite the equation in the form

$$w[1 + (\delta + \delta_L w)^2 + x] = -[1 + (\delta + \delta_L w)^2], \quad (\text{B.1})$$

where  $\delta = \Delta T_2$  is the detuning parameter,  $\delta_L = \Delta_L T_2$  is the Lorentz red-shift parameter, and  $x = |E|^2/|E_s^0|^2$  is the electric field parameter. We rewrite Eq. (B.1) as [170]

$$w^3 + a_2 w^2 + a_1 w + a_0 = 0, \quad (\text{B.2})$$



where

$$a_0 = \frac{1 + \delta^2}{\delta_L^2}, \quad (\text{B.3a})$$

$$a_1 = \frac{1 + \delta^2 + x + 2\delta\delta_L}{\delta_L^2}, \quad (\text{B.3b})$$

and

$$a_2 = \frac{2\delta + \delta_L}{\delta_L}. \quad (\text{B.3c})$$

Then, constructing

$$q = \frac{a_1}{3} - \frac{a_2^2}{9} \quad (\text{B.4a})$$

and

$$r = \frac{a_1 a_2 - 3a_0}{6} - \frac{a_2^3}{27}, \quad (\text{B.4b})$$

we look at the sign of the parameter

$$D = q^3 + r^2. \quad (\text{B.5})$$

If  $D > 0$ , there is one real root and a pair of complex conjugate roots; if  $D = 0$  all roots are real and at least two are equal; if  $D < 0$  all three roots are real (irreducible case) [170]. In order to achieve multiple physical solutions, we need the values of  $w$  to be real (and in the range  $-1$  to  $+1$ ). Certainly a necessary condition for this is  $D \leq 0$ . Introducing

$$s_1 = \left[ r + (q^3 + r^2)^{\frac{1}{2}} \right]^{\frac{1}{3}} \quad (\text{B.6a})$$

and

$$s_2 = \left[ r - (q^3 + r^2)^{\frac{1}{2}} \right]^{\frac{1}{3}}, \quad (\text{B.6b})$$

we write the solutions to Eq. (B.2) in the form [170]

$$w_1 = (s_1 + s_2) - \frac{a_2}{3}, \quad (\text{B.7a})$$

$$w_2 = -\frac{1}{2}(s_1 + s_2) - \frac{a_2}{3} + \frac{i\sqrt{3}}{2}(s_1 - s_2), \quad (\text{B.7b})$$

and

$$w_3 = -\frac{1}{2}(s_1 + s_2) - \frac{a_2}{3} - \frac{i\sqrt{3}}{2}(s_1 - s_2). \quad (\text{B.7c})$$

We now consider certain fixed values of the red shift parameter  $\delta_L$ , and investigate the ranges of  $\delta$  and  $x$  for which multiple physical solutions exist. Such ranges are marked with contours on the graphs in Fig. B.1. For the values of parameters  $\delta$  and  $x$  lying inside the contours there are three physical solutions to Eq. (B.2) with the corresponding values of  $w$  being within the range  $[-1 : 1]$ . The area outside the contours corresponds to a single physical solution for  $w$ , with the other two solutions being complex and, therefore, non-physical. According to our numerical analysis, summarized in Fig. B.1, multiple physical solutions only arise for  $|\delta_L| \geq 4.16$ . In sodium vapor that we consider as an example for our analysis in Section 3.3, such large values of  $\delta_L$  are not achievable; raising the density to increase  $\Delta_L$  also decreases  $T_2$  due to homogeneous broadening, and  $\delta_L$  can never get this large.

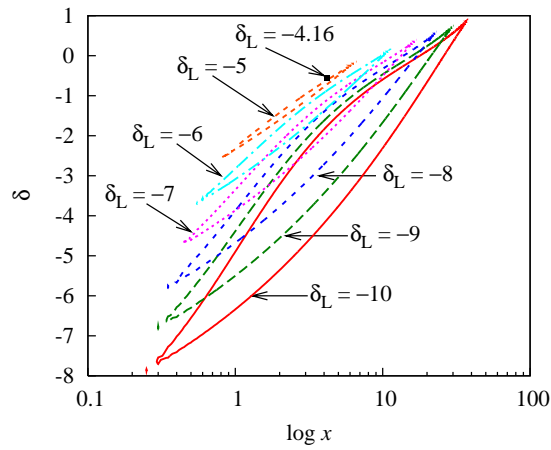


Figure B.1: The ranges of values of the detuning parameter  $\delta$  and the electric field parameter  $x$  for which mirrorless optical bistability is achievable (marked with contours). Different contours correspond to different values of the Lorentz redshift parameter  $\delta_L$ . The point corresponds to the limiting value  $\delta_L = -4.16$ : for  $|\delta_L| < 4.16$  there are no ranges of  $\delta$  and  $x$  at which optical bistability is achievable.